Laser Microstructured Scaffolds for Tissue Engineering Under Dynamic Cell Culture Conditions

A Thesis submitted for the degree of Doctor of Philosophy by

Eleftheria Babaliari

Supervisor: Prof. Anna Mitraki
Co-supervisors: Dr. Emmanuel Stratakis, Prof. Maria Vamvakaki

---

University of Crete, Materials Science and Technology Department
&
Foundation for Research and Technology (FORTH), Institute of Electronic Structure and Laser (IESL)

Heraklion, Crete, October 2020

Ευρωπαϊκή Ένωση
European Social Fund

Operational Programme
Human Resources Development,
Education and Lifelong Learning
Co-financed by Greece and the European Union

ΕΣΠΑ
2014-2020
ανάπτυξη - εργασία - αλληλεγγύη

<u>Acknowledgements</u>

I would like to express my sincere gratitude to my advisor Dr. Emmanuel Stratakis for his continuous guidance and support during all these years of my Ph.D. research in Ultrafast Laser Micro- and Nano- Processing (ULMNP) Laboratory. His constant assistance, motivation, and patience encouraged me to make this dissertation a reality. Moreover, my sincere regards go to my advisor Dr. Anthi Ranella for guiding my Ph.D. study in the Tissue Engineering - Regenerative Medicine and Immuno-engineering (TERMIM) Lab, for her continuous support, and constant encouragement. Without their persistent help and guidance, this dissertation would not have been possible. My appreciation also extends to my advisor Prof. Anna Mitraki for all her assistance and tremendous support since the early beginning of my Ph.D. research. Additionally, I would like to especially acknowledge my advisor Prof. Maria Vamvakaki for all her help and contribution to my committee.

Besides my advisors, I need to sincerely thank the rest members of my thesis committee, Prof. Electra Gizeli, Prof. Dimitris Papazoglou, and Prof. Kelly Velonia, for accepting to evaluate my Ph.D. thesis.

Furthermore, I wish to thank Dr. Yannis Papaharilaou in the Institute of Applied and Computational Mathematics (I.A.C.M.) for the collaboration and for conducting the computational flow simulations.

I would like to express my thanks to Aleka Manousaki for her support and continuous help with the Scanning Electron Microscopy (SEM) measurements.

My sincere thanks also go to all the members of the ULMNP and TERMIM group for all their assistance and the friendly working atmosphere. Special thanks go to Dr. Paraskevi Kavatzikidou for her invaluable advice and research feedback, as well as, for always being so supportive to me.

I want to especially acknowledge my colleagues in the office for all their help, constant encouragement, and for all the fun we had during the last years.

Finally, many warm thanks go to my family, my George, and my friends for always being supportive, patient, and constantly encouraging me in all areas all these years.

Abstract

Although the peripheral nervous system exhibits a higher rate of regeneration than that of the central nervous system through a spontaneous regeneration after injury, the functional recovery is fairly infrequent and misdirected. Thus, the development of successful methods to guide neuronal outgrowth, *in vitro*, is of high significance.

Neural tissue engineering has emerged as a promising alternative field for the development of new nerve graft substitutes to overcome the limitations of the current grafts. The ultimate goal of a tissue-engineered construct is to sufficiently mimic the topographic features of the extracellular matrix and the surrounding environment of cells, such as shear stress and soluble factors, so that cells will function in the artificial environment as they would *in vivo*.

Several approaches have been developed to create cellular substrates at the micro- and/or nano-scales that aim to reconstruct the extracellular matrix architecture *in vitro*. Among them, ultrafast laser structuring has proved to be important for engineering surface topography in various materials as a simple, fast, and effective method to fabricate micro- and nano-structures with controlled geometry and pattern regularity. Indeed, it has been well-reported that laser-induced topography significantly affects neuronal growth, orientation, and differentiation.

Apart from topography, it has recently become increasingly evident that neurogenesis may be also driven by mechanical factors. Mechanical stress is a significant component of the host environment, as it influences the cellular signal transduction and the behavior of various cells. However, the combined effect of flow-induced shear stress and surface topography on neuronal outgrowth has been rarely reported.

In the present thesis, a precise flow controlled microfluidic system with specific custom-designed chambers, incorporating the laser-microstructured substrates, was developed to investigate for the first time the combined effect of shear stress and topography on the growth, orientation, and elongation of Schwann (SW10) cells, as well as on the growth and differentiation of neuronal [Neuro-2a (N2a)] cells. Moreover, the effect of topography on the co-culture of SW10 and N2a cells was

investigated. For this purpose, polymeric [polyethylene terephthalate (PET)] microstructured substrates with different geometries, microgrooves, chess-like, net-like, were fabricated by ultrafast laser structuring. The cell culture results on the combined effect of shear stress and topography were combined with computational flow simulations to precisely calculate the shear stress values.

Our results demonstrate the ability to guide the outgrowth of Schwann cells via flow-induced shear stress and surface topography, which is crucial for neural tissue regeneration. Besides this, our findings revealed that shear stress may affect the differentiation of N2a cells. Thus, the microfluidic system presented here could be potentially used as a new model system to study the role of shear stress (induction and/or inhibition) on cell differentiation. Finally, our preliminary results on a co-culture system, comprising Schwann-SW10 glial cells and neuronal-N2a cells, showed that N2a cells preferentially grew and differentiated on top of the SW10 cells on the flat substrates. Further optimization of this co-culture patterned system will enable closer simulation of the *in vivo* microenvironment and hence will be useful in neural tissue-engineered dynamic microfluidic systems.

<u>Contents</u>

Abbreviations

2D	Two-dimensional
3D	Three-dimensional
AM	Acetoxymethyl
BHET	Bis(hydroxyethyl) terephthalate
boB	Bands of Büngner
BSA	Bovine serum albumin
cAMP	Cyclic AMP
CNS	Central nervous system
DAPI	4',6-Diamidino-2-Phenylindole
dhh	Desert Hedgehog
DMEM	Dulbecco's Modified Eagle's Medium
DMT	Dimethyl terephthalate
DRG	Dorsal root ganglion
ECM	Extracellular matrix
EG	Ethylene glycol
ESCs	Embryonic stem cells
EthD-1	Ethidium homodimer-1
FBS	Fetal Bovine Serum
GDA	Glutaraldehyde
GDNF	Glial cell line-derived neurotrophic factor
GF	Growth factors
GFAP	Glial fibrillary acidic protein
hiPSCs	Human induced pluripotent stem cells
hMSCs	Human mesenchymal stem cells
hNSCs	Human neural stem cells
HTS	High-throughput screening
HW	Half waveplate
IBMX	3-isobutyl-1-methylxanthine
IR	Infrared
LIF	Laser induced fluorescence

LP	Linear polarizer
MAG	Myelin-associated glycoprotein
MAP2	Microtubule-associated protein 2
MBP	Myelin basic protein
MG	Microgrooves
N2a	Neuro-2a
NGF	Nerve growth factor
NRG1-III	Neuregulin
NSCs	Neural stem cells
NT-3	Neurotrophin-3
PBS	Phosphate buffered saline
PC12	Adrenal pheochromocytoma
PCL	Polycaprolactone
PDLA	Poly(D,L-lactic acid)
PDMCs	Placenta-derived multipotent stem cells
PDMS	Polydimethylsiloxane
PET	Polyethylene terephthalate
PET-MG	Polyethylene terephthalate microgrooved
PFA	Paraformaldehyde
PI	Polyamide
PLGA	Poly(lactic-co-glycolic acid)
PLLA	Poly-L-lactic acid
PNS	Peripheral nervous system
PS	Pen-Strep
PTFE	Poly(tetrafluoroethylene)
RA	Retinoic acid
RGCs	Radial glial cells
SCB	Sodium cacodylate buffer
SEM	Scanning Electron Microscopy
SW	Shutter
SW10	Schwann
UV	Ultraviolet

UV-Vis   Ultraviolet-Visible

UV/VIS/NIR   Ultraviolet/Visible/Near Infrared

1. Introduction

1.1 Neurological injuries - Tissue engineering

Human adult nerve injuries are a major clinical problem that greatly affects the quality of patients' life [1]. They affect more than 1 billion people, around the world, resulting in 6.8 million deaths per year [2]. These injuries have been associated with a wide range of disorders including neurodegenerative diseases, brain and spinal cord traumatic injuries, and stroke [3].

The nervous system can be subdivided into the central nervous system (CNS) and the peripheral nervous system (PNS). Although the central nervous system does not regenerate after an injury, the peripheral nervous system has an intrinsic regenerative capacity [4]. When a peripheral nerve is damaged so that axons within it are severed, the portions of the affected axons lying distal to the injury site are cut off from the centrally located cell body. Afterward, these distal axon segments degrade, and the resulting debris is cleared away by Schwann cells and macrophages as part of a process termed "Wallerian degeneration". Schwann cells proliferate and take on a pro-regenerative phenotype, rearranging themselves into aligned tracts called "bands of Büngner" and secreting factors conducive to the in-growth of regenerating axons. Meantime, the portions of the injured neurons proximal to the damage site prepare for regeneration. The cell body of every injured axon undergoes major metabolic changes and initiates a program of protein synthesis to support axonal regeneration. At the tip of every injured axon, a growth cone develops leading the regenerating axon through the intact structure of the distal nerve segment and back toward its original target, at the approximate rate of 1-3 mm per day [4,5].

However, the process of peripheral nerve regeneration occurs spontaneously as long as the injury does not result in an extended gap in the nerve. Most of the time, such regeneration is rarely functional because when a nerve fiber loses its continuity with consequent damage of the basal lamina tubes, axon spontaneous regeneration is disorganized and mismatched resulting in an inadequate nerve functional recovery and musculoskeletal incapacity [1].

Nerve autografts remain the gold standard in the treatment of peripheral injuries. Healthy segments of the nerve are harvested from the patient's body and are used to bridge the gap across the injury site. However, this approach has several drawbacks including the need for additional surgery, loss of a functional nerve, donor site morbidity, and longer surgery procedures [1,4]. Therefore, tissue engineering has emerged as a promising alternative field for the development of new graft substitutes [6]. Indeed, the ultimate goal of using a tissue-engineered construct is to adequately mimic both the topographic features of the extracellular matrix (ECM) as well as its surrounding stimuli, including for example mechanical stresses and soluble factors, so that cells will respond within the artificial environment as they would *in vivo*.

The effective use of biomaterials within tissue-engineered constructs allows spatiotemporal control over the presentation of environmental cues so that the repair and regeneration of neuronal deficits can be engineered. Moreover, tissue engineering techniques use biomaterials to transplant cells replacing or supplementing the function of injured or diseased neural cells. Indeed, cell transplantation constructs can present cues that could influence not only the host neural tissue of the implantation site but also the transplanted cells contained within the constructs [4].

For the aforementioned reasons, much research has been devoted to developing a biomaterials-based implant as an alternative to an autograft. The ultimate goal is to engineer a construct that could be implanted across an injury gap in place of a nerve graft to provide support and guidance to regenerating cells and axons (Figure 1.1). Such a construct would employ biomaterials to recreate a pro-regenerative environment, similar to that which is found in the distal segment of the injured nerve. For instance, the bands of Büngner found in the distal nerve segment provide a physically aligned surface topography containing oriented tracks of adhesive molecules. Moreover, diffusible biochemical trophic and signaling factors are released by cells in the distal nerve stump. Thus, the development of biomaterials that could recreate these types of natural physical and chemical cues to guide migrating cells and regenerating axons across the nerve gap and into the distal nerve segment is of great importance [4].
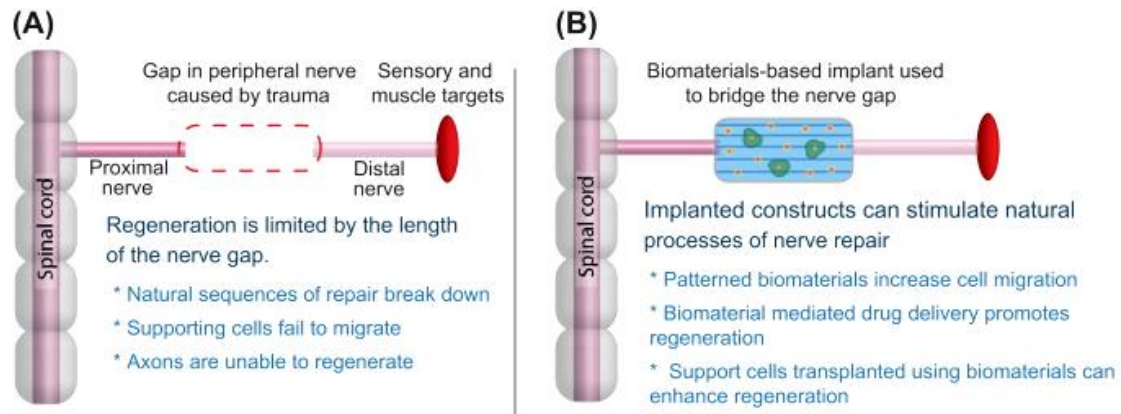
Figure 1.1: A) Summary of the biological constraints to peripheral nerve regeneration. B) Capacity of biomaterials-based constructs to alleviate biological constraints and promote regeneration [4].

1.2 Importance of size scale - Topography

The response of a cell to its surrounding topography depends strongly on the size of the topographic cues. Microscale features act at the cellular level, while submicron and nanoscale features act at subcellular levels [7]. For example, biological structures like growth cone filopodia lie within the nanometer range and are highly sensitive to nanoscale topographic cues [8]. Moreover, basement membranes, across which axons typically grow, are composed of a dense meshwork of three-dimensional topography, featuring pores and fibers with dimensions ranging from tens to hundreds of nanometers [9,10]. Consequently, control over micro/nanotopography is desirable.

At the cell-material interface, all the cellular processes are governed by the physical and chemical stimuli of substrate stiffness, topography, and chemistry, respectively, while at the intracellular level, focal adhesions are key molecular complexes for sensing the environmental conditions as significant mechanosensitive players [11–14]. Indeed, many studies confirmed that the surface topography influences the adhesion, migration, polarization, proliferation, and differentiation of cells [15–20].

In particular, neural cells respond highly to natural cues present in their surrounding environment, especially during periods of growth and development. For instance, the course of a regenerating axon is guided by the physical topography and chemistry of

the surface along which it grows, as well as by signaling molecules in the local environment. These biochemical and physical cues exert great influence on cellular viability, growth, and activity [4].

Biomaterials with patterned surfaces provide fine topographic cues additionally to tissue-level structural support. Topographic cues are physical features of the appropriate size and geometry to influence individual cells. Cellular attachment, growth, alignment, migration, and gene expression could be regulated by controlling the nature and distribution of topographic cues provided by the component biomaterials of a tissue-engineered construct [4].

The ability of the cells to respond to artificial topographic cues originates from the sensitivity of cells to natural topographic cues in their normal biological surroundings. During neural tissue development, for example, aligned ECM plays a significant role in guiding neural cell migration and differentiation [21]. By mimicking the natural structures along which neural cells develop, engineered substrates with particular topographies could greatly influence cellular behavior.

The mechanisms by which topographic cues affect cellular behavior are complex but involve interactions between the substrate topography and cellular structures that are sensitive to physical cues and able to effect cell-wide changes in behavior. Neural growth cones, for example, located at the front of extending axons/neurites, are especially sensitive to topographical features as they guide neuronal extension during periods of growth and development. Moreover, protrusions of filopodia on the end of the growth cones continuously advance or retract regarding physical and chemical cues as they "explore" their surrounding environment. Finally, growth cones direct axon/neurite extension by mediating the reorganization of the neuronal cytoskeleton [4].

This cytoskeletal reorganization is required for changes in cellular orientation, growth, and migration. In particular, the cytoskeleton is rearranged by depolymerization and polymerization of its component microtubules, intermediate filaments, and microfilaments [22]. It is hypothesized that these rod-like structures have a limited capability to bend, similar to a railroad track, and that their

polymerization is consequently dependent on the surrounding topography. This hypothesis may explain, for instance, why the alignment and growth of cells can be directionally constrained by certain types of topographic features like aligned grooves.

Consequently, size scale and topography are of high significance for the design and development of advanced biomaterials in neural tissue engineering. However, this task is often delicate as natural cues are presented in complex combinations within the intricate terrain of neural tissue. Thus, a considerable amount of research is devoted to the modification of materials' surfaces for use as platforms to study cell viability, differentiation, motility, and apoptosis [23,24].

1.3 Ultrafast laser structuring

1.3.1 Fundamentals

Several approaches have been developed to create structures on surfaces that aim to reconstruct the extracellular matrix architecture *in vitro* [23–25]. Previous studies have detailed the major fabrication techniques, the produced types of micro/nanostructured substrates, as well as, the respective advantages and disadvantages [26,27]. Among several techniques that have been developed for surface modification, laser irradiation has proved to be important in the enhancement of material biocompatibility, particularly via the creation of new functional groups and the precise topography formation at the cellular and subcellular scale [18,28–31].

In particular, microstructuring via ultrashort pulsed lasers provides unique control over the uniformity and regularity of micron and submicron features due to the local excitation of certain areas of material with minimal damage to the surrounding ones. This is attributed to the short pulse duration that enables a higher excitation threshold intensity to be attained without increasing the laser beam intensity. In the case of longer pulses, the thermal energy generated upon melting diffuses around the irradiation spot and gives rise to the creation of heat-affected zones. Above the material damage threshold, the heat-affected zone has a detrimental effect on the

integrity of the material, and microcracks together with micropores are produced. Moreover, the ablated material causes surface debris and recast layers, resulting in a poor fabrication outcome. These effects are avoided by using femtosecond laser pulses enabling faster ablation process (i.e. rapid vaporization and material removal) [32]. In dielectric materials, in particular, the collateral damage is mostly eliminated, [33] while in metals the heat-affected zones become smaller [34].

Although in the infrared (IR) wavelength region the photon energy is too small for photochemical ablation [35], amplified femtosecond pulses can be non-linearly absorbed producing clean ablation in various materials. In the particular case of dielectric polymers, it is generally considered that nonlinear processes associated with the irradiance generate free electrons. The free electrons are then responsible for increased absorption and consequent rapid heating, ionization, charge separation, as well as, removal of the absorbing material [35–37]. Furthermore, the thermal conduction length which corresponds to the femtosecond laser pulse duration is generally small, thus the absorbed energy is not significantly diffused [37]. It has been shown that femtosecond pulsed laser ablation has fewer affects on the remaining polymer surface than nanosecond pulsed laser ablation at comparable wavelengths [38–41].

Femtosecond laser structuring has various advantages compared to other techniques such as photolithography, as well as, mechanical and chemical methods. In particular, these techniques involve multiple steps, tedious sample preparation, and require hazardous chemicals [32]. Femtosecond laser structuring is a simple, single-step, fast, non-contact process and can be applied to a wide range of materials (metals, ceramics, polymers). Moreover, it can be used to texture materials on their surfaces, as well as etching deeper regions within the bulk of the material to create structures with complex geometries [42,43].

Materials that have been laser-patterned with structures like grooves, pillars, micro- and nano-cones [44], as well as, channels have been widely used as cell culture platforms to investigate the effect of topographical cues on various cellular responses [15].

1.3.2 Polyethylene terephthalate (PET)

Polyethylene terephthalate (PET) is a semicrystalline, thermoplastic resin which belongs to the polyester family [45]. The commercial synthesis of PET begins with one of two chemical reactions: 1) Ethylene glycol (EG) is reacted with terephthalic acid or 2) EG is reacted with dimethyl terephthalate (DMT) [46,47]. The reaction 1 is performed at 240 - 260°C and 300 - 500 kPa, while the reaction 2 at 140 - 220°C and 100 kPa. They both yield bis(hydroxyethyl) terephthalate (BHET) [46,47]. After the initial reaction, two or three polymerization steps are performed which depend on the required molecular weight (Figure 1.2). The first polymerization step is transesterification between BHET molecules, displacing EG, at 250 - 280°C and 2 - 3 kPa [46,48]. Afterward, the resulting oligomers are polycondensed at 270 - 280°C and 50 - 100 kPa [46,47]. At this stage, the polymer is appropriate for applications that do not require high molecular weight chains. If a higher molecular weight is required, the polymer is subjected to a third, solid state polymerization, at 200 - 240°C and 100 kPa [46,47,49]. After the synthesis of the raw polymer, it can then be processed into the required form, via injection moulding, extrusion, or blow moulding [46]. The physical properties of PET are presented in Table 1.1.
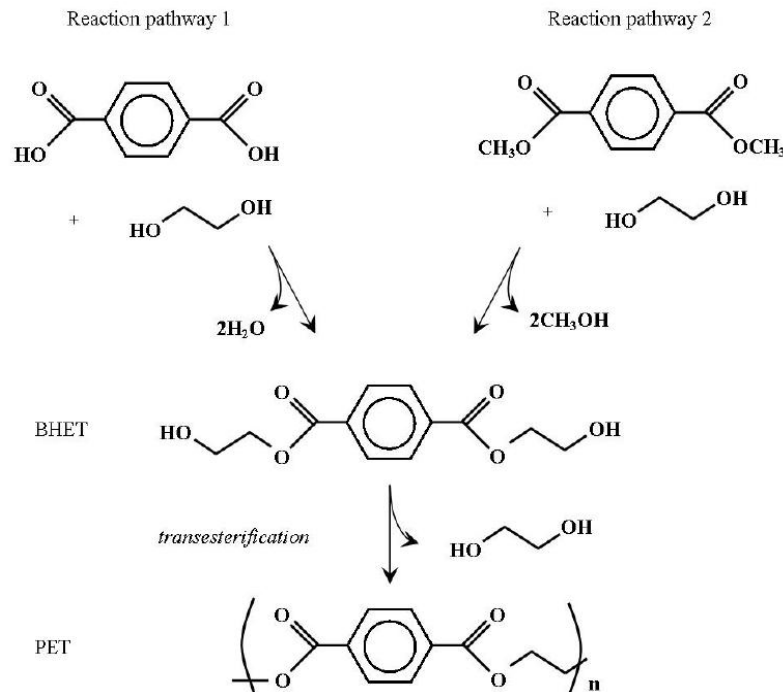
Figure 1.2: *Chemical reactions of polyethylene terephthalate (PET) manufacturing* [45].

Table 1.1: *Physical properties of polyethylene terephthalate (PET)* [37,45,50].

	Average molecular weight (g/mol)	Density (g/cm³)	Melting temperature, T_m (°C)	Glass transition temperature, T_g (°C)	Thermal conductivity [W/(mK)]	Heat capacity [kJ/(kgK)]
Polyethylene terephthalate (PET)	30000 - 80000	1.3 - 1.4	250 - 270	69 - 115	0.13 - 0.15	1.3

PET is one of the most common polymers widely used for cell culturing (Thermanox® or Mylar®) and biomedical applications [51,52]. Specifically, chemically inert PET (Dacron®) biomaterials, combined with different coatings, are used in sutures, vascular grafts, surgical meshes, scaffolds, heart valves, urinary, and bloodstream catheters due to their biocompatibility and excellent mechanical strength and resistance [51–53].

1.4 Role of shear stress

Shear stress is termed as "the external force acting on an object or surface parallel to the slope or plane in which it lies" [54] (Figure 1.3).
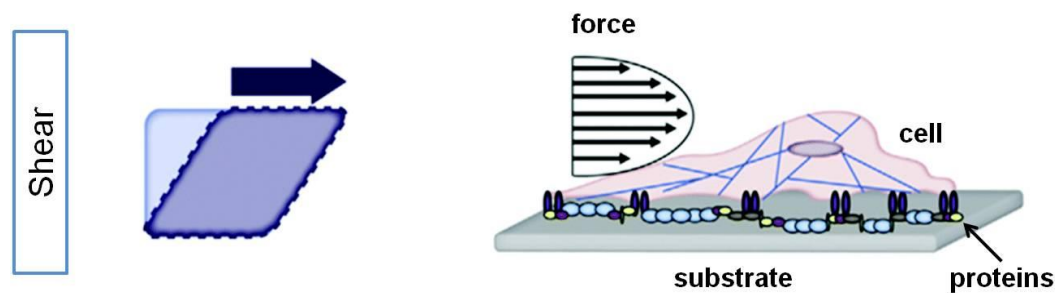
Figure 1.3: Externally applied force results in shear stress on cells. Simplified illustration of the effect of shear in planar culture is shown for an idealized square (left) and a cell (right). Shear stress induces an angle change between opposing sides of the cell (modified by [55]).

Apart from topography, mechanical stress is also a significant component of the host environment, as it influences the cellular signal transduction and the behavior of

various cells. Flow-induced shear stress, in particular, influences mechanoreceptors, like ion channels and integrin/focal adhesions, as well as responses, such as nitric oxide and intracellular calcium production, and cytoskeletal remodeling [56]. Shear stress is applied at discrete local points and is transmitted through the cell body along cytoskeletal microstructures, which in turn trigger intracellular mechanical signaling. Thus, shear stress alters not only the cell's shape but also the intracellular signaling pathways [57,58] (Figure 1.4).
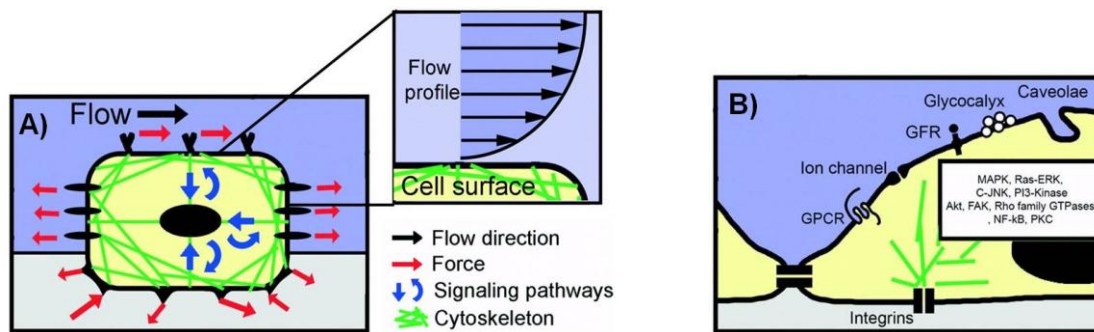
Figure 1.4: Cell mechanosensing model approach at the micro- and nano-scale. A) A mechanosensing approach, where a cell internalizes both mechanical and biochemical signals. B) Schematic representation of selected membrane-bound nanoscale structures involved in intracellular mechanical signaling (modified by [58]).

Flow-induced shear stress can be applied to cells, *in vitro*, using specially designed microfluidic systems. In particular, fluid flow applies shear stress to a monolayer of cultured cells (Figure 1.5). Assuming parallel-plate geometry, the applied shear stress is often approximated by the equation of wall shear stress [59,60],

$$\tau_w = (6\mu Q)/(bh^2)$$

where μ is the fluid viscosity, Q is the flow rate, b is the width of the parallel plates, and h is the separation (height) of the parallel plates.
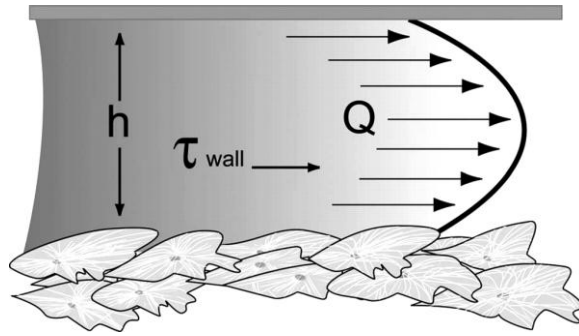
Figure 1.5: *Fluid shear in a parallel-plate flow chamber. h refers to the separation (height) of the parallel plates, Q to the flow rate, and τ_{wall} to the wall shear stress* [60].

Previous studies have shown that fluid-induced shear stress enhances the cells' alignment, through the reorganization of the cytoskeleton, in a variety of cell types [61−67]. An association between extracellular matrix alignment and cell shear stress was also reported in [68]. In addition to this, it has been shown that such stimulation affects cellular migration [63].

Chafik et. al. [69] reported that shear stress is a critical component of the natural environment for the regeneration of axons. Indeed, it is known that the cell soma and the neurites of neurons are correlated to the cytoskeleton, which senses the mechanical stimuli producing different cellular responses [57,69,70]. Moreover, it has been reported that cell proliferation, migration, and differentiation are controlled via numerous unknown signaling pathways connected to the cytoskeleton [70,71]. Thus, fluid-induced shear stress may be also crucial for guiding neurite outgrowth. However, the effect of shear stress on neuronal outgrowth has not been studied thoroughly [69,72−76].

1.5 Cell culture under microfluidic flow

Over the last decades, conventional cell culture techniques are well-established and essentially consist of culturing cells in flasks, petri dishes, and microtiter plates [77]. The cells are usually maintained under static conditions and have limited cell-cell interactions. However, cells in a multicellular organism live in a considerably different environment compared to conventional static cultures. They are attached to

softer materials than the glass and plastic substrates on which most studies are done *in vitro*, and are surrounded by fluid and nutrients [61,78] (Figure 1.6). To gain more insight into different biological problems, it is important to perform cellular experiments that reflect more closely the *in vivo* conditions with cell-cell, cell-matrix, and cell-soluble factor interactions [79].
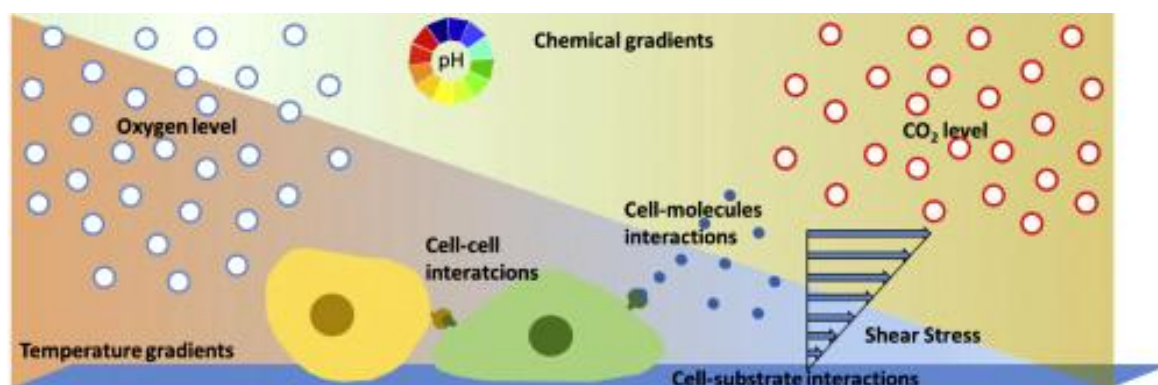
Figure 1.6: *Schematic representation of the microenvironment of cells consisting of biochemical (cell interactions), physical (shear stress), and physicochemical [pH, carbon dioxide (CO_2), temperature, oxygen (O_2)] factors* [77].

Microfluidic devices provide a more realistic environment for biological research, as they are related to scales found in biological systems (micro- and nano-). Cells are in the micrometer range, typically around 10 - 15 μm. Unlike conventional static cultures, microfluidic cell cultures permit precise control of the microenvironment [e.g. changes in the flow rate, pH, oxygen (O_2) levels] that influence biochemical and mechanical factors in a cell and, thus, cell functionality [78]. Figure 1.7 illustrates the possible physicochemical and biomolecular stimuli provided by the microfluidic flow.
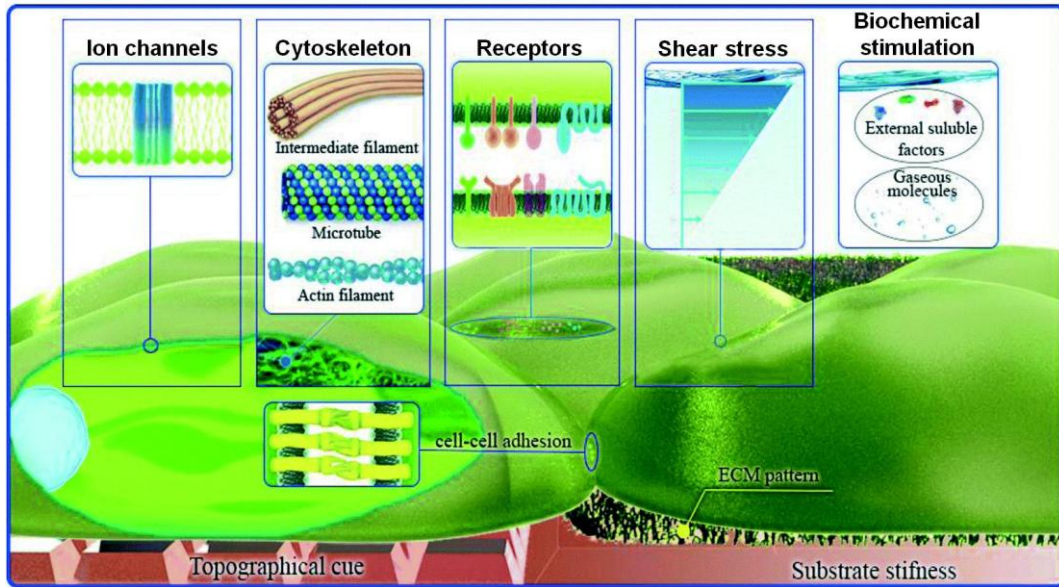
Figure 1.7: *Schematic representation of the possible physicochemical and biomolecular stimuli, which could be provided by microfluidic flow (modified from* [80]*).*

In particular, cell cultures under microfluidic flow reflect more appropriately the *in vivo* environment of cells in tissues such as the physiological fluid flow inside the body, consistent nutrient delivery, effective waste removal, and mechanical stimulation due to fluid shear forces [81]. Laminar flow regimes, small length scales, and diffusion dominated mass transport characterize the microfluidic devices resulting in a more *in vivo*-like environment [80]. Indeed, the continuous flow of nutrient is a distinct advantage that microfluidic flow brings to dynamic cell cultures in contrast to conventional static ones. Furthermore, small volumes of media in microfluidic devices reflect more appropriately the physiological condition of cells in tissues than cells cultured in larger volumes, due to faster consumption of nutrients and increased concentration of metabolites and secreted products, similar to densely packed tissues [81].

Table 1.2 summarizes some important differences between conventional static cultures and cell cultures under microfluidic flow.

Table 1.2: *Differences between conventional static cultures and cell cultures under microfluidic flow (modified by* [82]*).*

Conventional static cultures	Cell cultures under microfluidic flow
Cell microenvironment	
No confinement (open walls)	**Confinement** (closed systems)
Limited level of **spatial control** (e.g. only single-well or trans-well systems)	**High** level of **spatial control** (e.g. compartmentalization for co-culture, 3-dimensionality and sub-cellular resolution)
No fluid control (only static)	**High** level of **control** over **fluids** (e.g. laminar flow, perfusion, temporal control over fluid exchange)
Limited possibilities for creating **physical stimuli**	**Various physical stimuli** possible (e.g. shear)
Low temporal and **spatial** control over **chemical stimuli** (only bulk addition)	Possibility to create **highly** defined **spatial** and **temporal chemical stimuli** (e.g. soluble or surface gradients)
Biological read-out	
Compatible with **conventional** standardized **biological assays**	**Compatibility issues** with **conventional** standardized **biological assays**
Compatible with **established read-out equipment**	**Compatibility issues** with **established read-out equipment**
Comparable to large amount of **data** from **historical experiments**	**Low number** of available **historical experiments** limits comparison
Limited possibilities for *in situ* **read-out** of **biological processes**	**Possibility** to integrate sensors and assays for *in situ* **read-out** of **biological processes**
High-throughput screening (HTS)	
High reagent and **biological** (cell) **material use** in **HTS** setting	**Reduced reagent** and **biological** (cell) **material use** in **HTS setting**
Limited possibilities to **parallelize** and **integrate** assays	**Highly** applicable to **parallelization** and **integration** of assays
Compatible to **conventional high-throughput** (robotics) **equipment**	**Not compatible** with **conventional high-throughput** (robotics) **equipment**

Utilizing the microfluidic technology discussed above, numerous microfluidic platforms applied to stem cells [83–87], tumor cells [88–90], and other types of cells [63–67,91,92]. Microfluidic platforms are designed for several specific applications

including single-cell studies [93–95], biomarkers' detection [96–98], drug screening and discovery [99–101], organs-on-chip [102–111], and tissue engineering [80,112,113].

A summary of applications for individual cell types is presented in Figure 1.8.
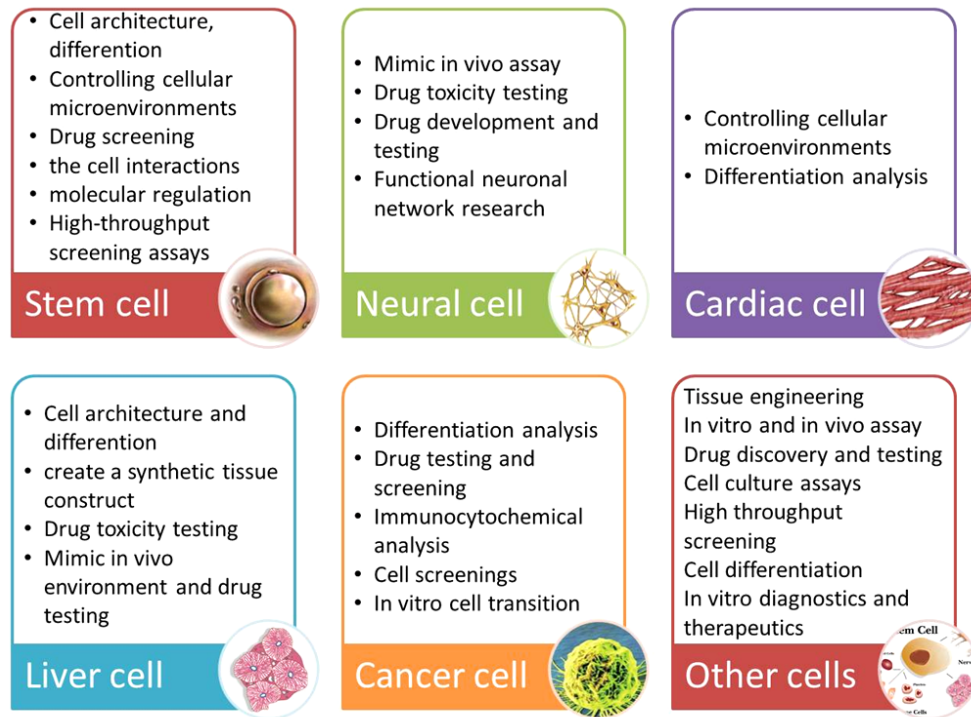
Figure 1.8: *Summarized applications of cell culture under microfluidic flow according to cell type* [114].

1.6 Peripheral nervous system

1.6.1 Peripheral nerve anatomy

The nervous system is classified into the CNS and the PNS. In particular, the CNS contains the brain and the spinal cord. The PNS includes the cranial, spinal, and autonomic nerves, which, along with their branches, connect to the CNS [115]. Peripheral nerves innervate muscle tissue, transmitting sensory and excitatory input to and from the spinal column.

The nervous system consists of two cell types, neurons, and neuroglia. Neurons are the main structural and functional elements of the nervous system and consist of a cell body (soma) and its extensions (axons and dendrites). Clusters of sensory nerve soma (ganglia) are located just outside the spinal column. Dendrites transmit electrical signals to the cell body of the neuron and the axon conducts impulses away. Neuroglia or glial cells are support cells that aid the function of neurons. They include astrocytes and oligodendrocytes in the CNS and Schwann cells in the PNS. Glial cells are more abundant than neurons. In contrast to neurons which cannot undergo mitosis, glial cells have some capacity for cell division. Although neurons cannot divide by mitosis, they can sprout new processes or regenerate a severed portion under certain conditions [116]. For example, sympathetic and cortical neurons try to reactive the cell cycle when subjected to acute insults, like oxidative stress, DNA damage, and excitotoxicity [117].

In the PNS myelin sheath, a laminated sheath made up of lipoproteins is formed by consecutive wrappings of Schwann cell membrane around the axon of a neuron. On the outer surface of this Schwann cell layer is the neurilemma which is a basement membrane similar to that found in epithelial cells. The neurilemma is only present in the PNS due to the lack of Schwann cells in the CNS. In the CNS the myelin sheath is delivered by oligodendrocytes. Myelin sheath protects and insulates the nerve fiber, as well as, increases the propagation velocity of the nerve impulse, which is particularly important for those axons extending long distances up to 1 meter [116].

A peripheral nerve is composed of sensory and motor axons bundled together by support tissue into an anatomically defined trunk (Figure 1.9). Endoneurium, composed predominantly of oriented collagen fibers, surrounds individual axons and their Schwann cells sheaths. Afterward, the perineurium which is formed from many layers of flattened cells (fibroblasts) and collagen, surrounds group of axons to form fascicles. Finally, the epineurium, an outer sheath of loose fibrocollagenous tissue, binds individual nerve fascicles into a nerve trunk. Peripheral nerves are well vascularized by capillaries within the support tissue of the nerve trunk or by vessels penetrating the nerve from surrounding arteries and veins [116].
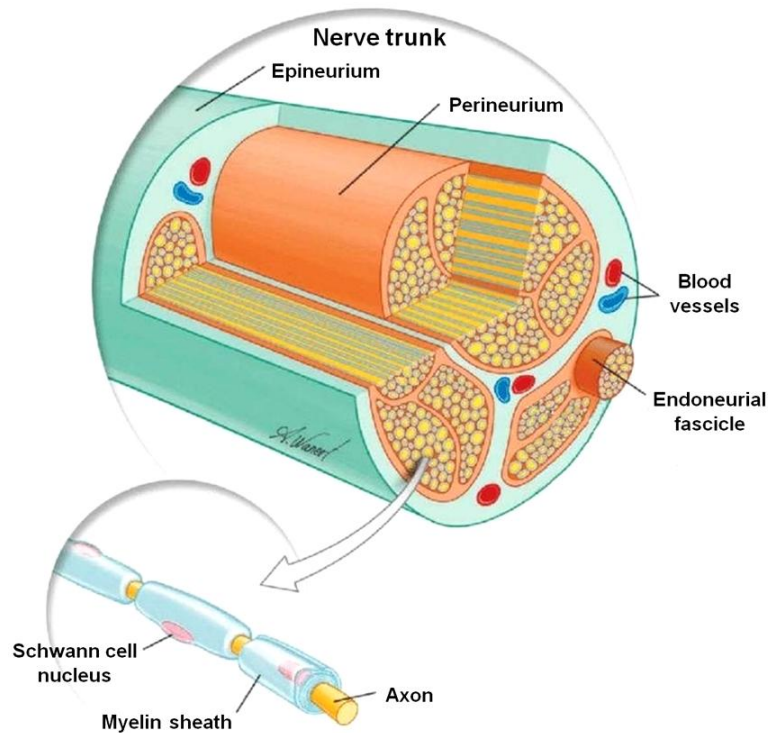
Figure 1.9: *Peripheral nerve anatomy (modified by* [118]*).*

1.6.2 Cells used for this study

For the cell cultures, fibroblasts (NIH 3T3 cells), Schwann (SW10) cells, and neuronal [Neuro-2a (N2a)] cells were used as well-studied and characterized experimental models for the study of cellular functions such as adhesion and proliferation (NIH 3T3 cells), neurogenesis, and neuronal differentiation (SW10 cells and N2a cells respectively).

NIH 3T3 cells were initiated from a cell line isolated at the Department of Pathology in the New York University School of Medicine in 1962 by George Todaro and Howard Green. 3T3 refers to the cell transfer and inoculation method for the line and means "3-day transfer, inoculum 3 x 10^5 cells" [119]. NIH refers to "National Institutes of Health" and was added later [120]. Using this method, the immortal cell line begins to thrive and stabilize in cell culture after about 20 - 30 generations of *in vitro* growth. The two scientists originally obtained the cells from desegregated NIH Swiss mouse embryo fibroblasts. Since being established, the mouse fibroblast cell line NIH 3T3 cells has been used in thousands of studies [120]. Indeed, it has been

used as a model system in a multitude of different studies including adhesion and proliferation.

During the mid-19th century while investigating the nervous system, Theodore Schwann, the co-founder of the cell theory, discovered that specific cells are wrapped around the axons of the PNS. What Theodore Schwann discovered then, it is now termed as "Schwann cell". Although neurons form the basis of the nervous system, glial cells play a vital role in the survival and function of neurons. Schwann cells are the main glial cells in peripheral nerves and are derived from neural crest cells. They come in two types, myelinating or non-myelinating Schwann cells, both playing a pivotal role in the maintenance and regeneration of the neurons' axons in the PNS. Schwann cells are under investigation as a therapeutic agent for spinal cord injuries and demyelinating diseases [121]. One of the most important functions of the Schwann cells is to myelinate the axons of the PNS. Myelin, as previously described in section 1.6.1, insulates the axons and helps to increase the saltatory conduction of the neuron. A myelinating Schwann cell wraps around one axon. Myelination occurs in larger diameter axons (>1 μm) while a process called ensheathment occurs on smaller diameter axons. In the case of ensheathment, a single cell wraps around multiple small unmyelinated axons separating them with a thin layer of cytoplasm. The resulting structure is called a Remak bundle. The axon diameter determines if Schwann cells will myelinate or ensheath axons [122]. Independent of axon diameter, axons that express low levels of neuregulin, NRG1-III, are ensheathed while those expressing high levels are myelinated [123]. Schwann cells also assist in neuronal survival and signal the formation of various structures within the PNS. Indeed, they offer trophic support for developing neurons whose axons have not reached their targets yet [124]. Two key secreted factors that may play a critical role are glial cell line-derived neurotrophic factor (GDNF) and neurotrophin-3 (NT-3) [125]. Moreover, Schwann cells regulate the formation of the perineurium and the node of Ranvier. Specifically, they secret Desert Hedgehog (dhh) which helps to form the perineurial sheath, a protective barrier for the peripheral nerves. The nodes of Ranvier are gaps found between the myelin sheath of an axon. Developing Schwann cells are thought to produce signals that cluster the Na^{+} channels in the axon membrane, normally at the edge of the Schwann cell [125]. In contrast to neurons, Schwann cells cannot

transmit synaptic messages and can divide indefinitely throughout life. The counterparts of Schwann cells in the CNS are the oligodendrocytes. Contrary to oligodendrocytes, Schwann cells enter quickly mitosis after the occurrence of an injury implying that may be better for treating spinal cord injuries and demyelinating disorders [121]. Thus, although Schwann cells are often overlooked due to their supporting role to the neurons, they play a central role in many aspects of neuronal homeostasis and are associated with several pathologies. The mouse Schwann cell line SW10 cells has been used as a model system in many studies including adhesion, proliferation, and orientation.

N2a is a mouse neural crest-derived cell line that has been extensively used as a model system to study proliferation, neuronal differentiation, neurite outgrowth, signaling pathways, and cytotoxicity [126–131]. A useful characteristic of N2a cells is their ability to differentiate into neurons within a few days. Their differentiation is usually obtained in specific conditions of culturing, like serum deprivation or addition of retinoic acid (RA) or cyclic AMP (cAMP) to the culture medium [132]. As a result, N2a cells can develop axon-like or dendrite-like processes, similar to those observed in hippocampal and cortical cultures [133]. Their tendency to differentiate to neurons can be evaluated by the overall qualitative cell morphology as shown around the soma. Additionally, it can be quantitatively expressed by the number and length of neurite-like extensions [134]. Thus, N2a cells have proven to be a useful model to study the effect of different stimuli on neuronal proliferation and differentiation.

1.7 Effect of topography on neuronal outgrowth

It has been well-reported that the surface topography significantly affects the adhesion, orientation, proliferation, and differentiation of cells. Therefore, many groups focused their interest on the controlled modification of materials' surfaces, as a strategy for guiding the neuronal outgrowth, which is crucial for the development of functional neuronal interfaces [23,24,26,42,133,135–137].

Based on their design, the different geometries attained via patterning are classified in continuous and discontinuous (Figure 1.10). Continuous geometries are further

classified into anisotropic, isotropic, and topography-gradient topographies. Anisotropic topographies are directionally dependent providing cues along a single axis. Isotropic topographies are uniform in all directions providing cues along multiple axes. Topography-gradient topographies provide cues through gradual changes in physical features, such as groove spacing, along a particular direction. Grooved substrates and electrospun polymeric fibers at parallel or random orientation are examples of continuous topographies. Discontinuous geometries are further classified into isotropic and topography-gradient topographies. Pillars/posts and pits are examples of discontinuous topographies [138].
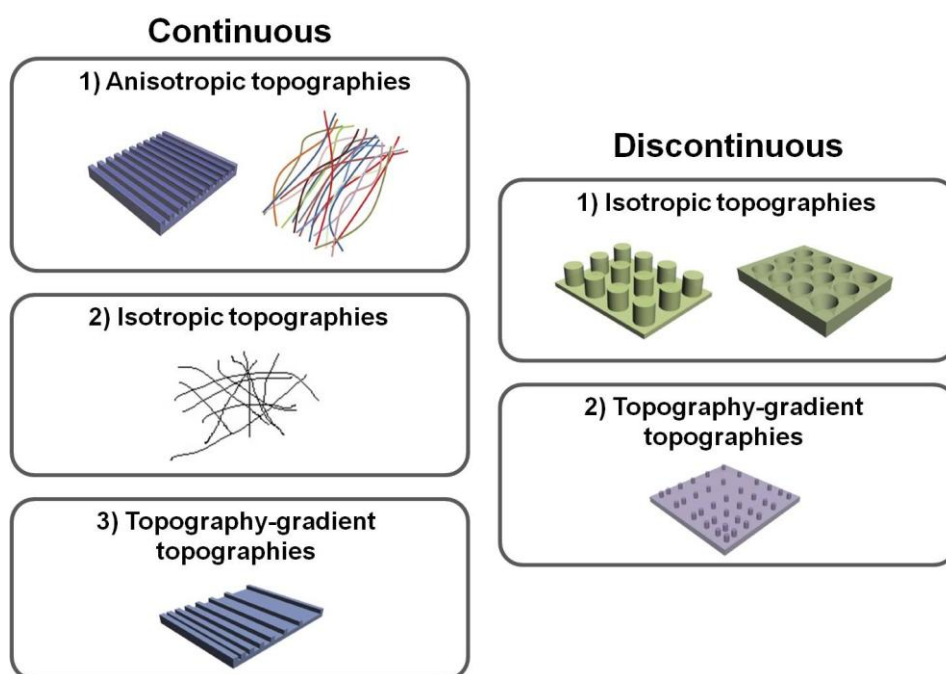
Figure 1.10: *Schematic representations of the different geometries being used as cell culture substrates (modified from* [138]*).*

It has been shown that anisotropic continuous electrospun polymeric fibers could influence neuronal growth, alignment, and differentiation [139–148]. It has been also reported that in continuous grooved substrates the width and the depth have a critical role in the neuronal outgrowth [149,150,159–161,151–158]. Additionally, previous studies elucidated the impact of disordered/anisotropic nanotopographical features on neuronal differentiation and maturation, by mechanotransduction pathways, in adrenal pheochromocytoma (PC12) cells [162–164].

19

Among various techniques employed, ultrashort-pulse laser structuring has proved to be important for engineering surface topography in various materials including polymers, such as poly-L-lactic acid (PLLA), polycaprolactone (PCL), and silicon (Si) [15,18,30,31,165–167]. Indeed, the laser-induced topography was found to significantly affect the neuronal adhesion, growth, and orientation. Specifically, Yiannakou et. al. [15] reported that laser-microstructured Si substrates with nanoripples, as well as, microgrooves decorated with nanoripples (hierarchical patterns) affected Schwann cells' behavior. It has been shown that although cell adhesion and growth was inhibited by the nanoripples, it was significantly promoted by the hierarchical micro- and nano-structures. Furthermore, Simitzi et. al. [30,31] showed that laser-microstructured discontinuous Si substrates not only support cellular adhesion and viability, but also significantly affect cell morphology, growth, orientation, and differentiation in a surface-dependent manner. It has been reported that Schwann cells and sympathetic neurons' axons were parallel oriented on microcone patterns of elliptical cross-sections, while they exhibited a random orientation on the microcones exhibiting arbitrarily shaped cross-sections. Continuing further the above investigations, Angelaki et. al. [167] developed a combined topography comprising rectangles of microcones on a nanosized ripples surface that could create selective neuron cell patterns. It has been shown that when Schwann cells were co-cultured with N2a cells, N2a cells adhered on top of the oriented Schwann cells and only on the areas where the Schwann cells adhered i.e. microcones. Consequently, it was suggested that anisotropic continuous and discontinuous topographical patterns could promote Schwann cell and axonal alignment, provided that the pattern presents anisotropic geometrical features, even though their sizes are at a subcellular scale [30]. Finally, the same topographical system, i.e. microcones, were used to study PC12 differentiation after treatment with nerve growth factor (NGF). Although PC12 cells were stimulated with NGF, it has been shown that surfaces that were highly rough and exhibited large distances between microcones did not support cell differentiation in contrast to surfaces with low and medium roughness [31].

1.8 Effect of microfluidic flow on neuronal outgrowth

Many studies have shown that the dynamic culture of neuronal and/or glial cells has a positive effect on their cell function and behavior (morphology, proliferation, differentiation). Specifically, Millet et. al. [168] considering that cell-to-cell signaling is local, they developed a specific culture system that sustained small numbers of primary hippocampal neurons and enabled analysis of the microenvironment. They observed that cultured neurons inside perfused channels (by gravity flow) composed of native, autoclave, or extracted polydimethylsiloxane (PDMS) showed increased viability and channel-length capacity (increasing 2-fold for all but native PDMS). Moreover, Park et. al. [72] designed a two-dimensional microfluidic system to study the effect of continuous flow shear stress (10^{-4} and 10^{-3} Pa) on radial glial cells (RGCs). They found that flow shear stress possibly activated mechanosensitive Ca^{+2} channels that significantly enhanced the proliferative capacity of RGCs in response to increased shear stress.

Nakashima and Yasuda [169] fabricated a microfluidic device to investigate the effect of growth factors (GF) on the differentiation and axon elongation guidance of PC12 cells. The microfluidic device composed of a cell culture chamber, a micro-channel, a nano-hole array (containing GF), and a micro-valve allowing the precise release of chemicals from the nano-hole. NGF was used to stimulate the differentiation of PC12 cells. They showed that the cell growth, differentiation, and axon elongation were dependent on micro-valve switching and release gradient of NGF. Chung et. al. [73] developed a PDMS gradient-generating microfluidic platform that exposed human neural stem cells (hNSCs) to a concentration gradient of known GF, under continuous flow ($5 \cdot 10^{-5}$ Pa). As a result, a minimization of autocrine and paracrine signaling was observed. Additionally, they found that the differentiation of hNSCs into astrocytes was inversely proportional to GF concentration while proliferation was directly proportional. Kim et. al. [170] performed a similar study by using a microfluidic chip-generated growth factor gradient system and neural stem cells (NSCs). Results confirmed that the proliferation and differentiation of NSCs were directly dependent on the concentration gradient of GF. Furthermore, Park et. al. [171] designed a microfluidic platform to expose human embryonic stem cells (ESCs)-derived neural

progenitor cells to stable concentration gradients of extracellular signaling molecules. Human ESC-derived neural progenitor cells were cultured in the microfluidic system under continuous cytokine gradients (0.15 μL/hour) for 8 days. Neural progenitor cells proliferated and differentiated, into neurons, in a controlled manner and the cell properties reflected the different concentrations of extracellular signaling molecules.

Cheng et al. [74] fabricated a microfluidic system that could analyze the effect of mechanical and chemical stimulation on neuronal differentiation of placenta-derived multipotent stem cells (PDMCs). They analyzed the effect of shear stress with various flow rates ($1.4 \cdot 10^{-4}$, $3.31 \cdot 10^{-3}$, $4.97 \cdot 10^{-3}$ Pa) on PDMCs beside 3-isobutyl-1-methylxanthine (IBMX), as the chemical stimulant, for 3 days. They found that shear stress could not differentiate PDMCs into other cell types. Although chemical stimulation played a critical role in the differentiation of PDMCs, shear stress enhanced PDMCs for earlier neuronal differentiation. The highest cell differentiation ratio of 42.4% was noticed in the highest flow rate and IBMX in 48-hour condition.

Chafik et al. [69] developed a custom-designed flow chamber that applied shear stress (1.33 Pa for 2 hours), through laminar fluid flow, to Schwann cells. They showed that mechanical stimuli enhanced the proliferation of Schwann cells and caused a slight movement from their original positions. Moreover, Gupta et. al. [75,76] used an *in vitro* model to apply shear stress on primary Schwann cells in the form of laminar fluid flow (3.1 Pa for 2 hours). They observed increased proliferation and down-regulation of two pro-myelinating proteins, myelin-associated glycoprotein (MAG) and myelin basic protein (MBP). These results implied that a low level of mechanical stimulus may directly trigger Schwann cell proliferation.

Majumdar et. al. [172] designed a PDMS microfluidic cell co-culture platform that allowed individual manipulation of various cell types with the position of a microfabricated valve that served as a reversible barrier between the chambers. As a result, healthy co-cultures of hippocampal neurons and glia were maintained for several weeks under optimal conditions. In particular, co-culture with glia provided nutrient media for maintaining healthy neural cultures, eliminating the need to supply neurons with pre-conditioned glia media, and enhanced the transfection efficiency of neurons in the platform. Similarly, Shi et. al. [173] fabricated two PDMS microfluidic

cell culture systems, a vertically-layered set-up, and a four-chamber set-up for studying communication between neurons and glia in close proximity. The chambers were separated by pressure-enabled valve barriers that allowed them to control communication between the two cell types. They observed that the co-culture of neurons and glia increased the number and stability of synaptic contacts, as well as, the secreted levels of soluble factors. These results confirmed the importance of communication between neurons and glia for the development of stable synapses in microfluidic platforms.

The neuronal response to microfluidic flow is summarized in Table 1.3 where the different approaches and the respective nerve responses are presented.

Table 1.3: Effect of microfluidic flow on nerve cell morphology/response.

Cell type	Circulating Flow?	Shear stress	Findings	Reference
Hippocampal neurons	No	-	▪ Increased viability and channel-length capacity	[168]
Radial glial cells (RGCs)	Yes	▪ 10^{-4} Pa ▪ 10^{-3} Pa for 5 days	▪ Increased proliferation of RGCs in response to increased shear stress	[72]
Adrenal pheochromocytoma (PC12) cells	No	-	▪ Cell growth, differentiation and axon elongation were dependent on micro-valve switching and release gradient of nerve growth factor (NGF)	[169]
Human neural stem cells (hNSCs)	Yes	▪ $5 \cdot 10^{-5}$ Pa for 4 and 7 days	▪ Minimization of autocrine and paracrine signals ▪ Differentiation of hNSCs into astrocytes was inversely proportional to growth factors (GF) concentration ▪ Proliferation was directly proportional to GF concentration	[73]

			• Simultaneous application of multiple gradients in a single experiment • Low media requirements • Low cell requirements	
Neural stem cells (NSCs)	Yes	-	• Proliferation and differentiation of NSCs were directly dependent on GF concentration	[170]
Neural progenitor cells	Yes	-	• Proliferation and differentiation of neural progenitor cells in a controlled manner • Cells properties reflected the different concentrations of extracellular signaling molecules	[171]
Placenta-derived multipotent stem cells (PDMCs)	Yes	• $1.4 \cdot 10^{-4}$ Pa • $3.31 \cdot 10^{-3}$ Pa • $4.97 \cdot 10^{-3}$ Pa for 1 hour, 2 hours, 24 hours, 48 hours, 72 hours	• No differentiation of PDMCs into other cell types with shear stress • Shear stress combined with 3-isobutyl-1-methylxanthine (IBMX) enhanced the PDMCs for earlier neuronal differentiation • Highest cell differentiation in the highest flow rate and IBMX in 48-hour condition	[74]
Schwann cells	Yes	• 1.33 Pa for 2 hours	• Increased proliferation • Slight cells' movement from their original positions	[69]
Schwann cells	Yes	• 3.1 Pa for 2 hours	• Increased proliferation	[75]
Schwann cells	Yes	• 3.1 Pa for 2 hours	• Increased proliferation • Down-regulation of myelin-	[76]

			associated glycoprotein (MAG) and myelin basic protein (MBP)	
Co-culture of hippocampal neurons and glia	No	-	▪ Elimination of the need to supply neurons with pre-conditioned glia media ▪ Enhancement of the transfection efficiency of neurons	[172]
Co-culture of hippocampal neurons and glia	No	-	▪ Increased number of synaptic contacts ▪ Increased stability of synaptic contacts ▪ Increased secreted levels of soluble factors	[173]

1.9 Combined effect of microfluidic flow and topography on neuronal outgrowth

The combined effect of microfluidic flow and topography on neuronal outgrowth has been rarely reported. Specifically, Hesari et. al. [174] developed a hybrid microfluidic system composed of PDMS microchip and poly(lactic-co-glycolic acid) (PLGA) nanofiber-based substrate for differentiation of human induced pluripotent stem cells (hiPSCs) into neurons. The results revealed an increase of β-tubulin III (a neuron-specific marker) gene expression and a decrease of glial fibrillary acidic protein (GFAP) (a classic marker for astrocytes) gene expression. Thus, this hybrid microfluidic system could be optimum for neuronal differentiation. Afterward, for further *in vivo* evaluation of this system, the cell loaded scaffold was implanted in a spinal cord model of rats. Animals receiving this implant showed functional improvement during 28 days of study. However, the difference with the control group was statistically insignificant.

Kim et. al. [57] studied the effect of mechanical stimulation on PC12 cells cultured in microfiber-based substrates. They observed that the shear stress affected the length and orientation of neurons along the microfibers. Furthermore, Jeon et. al. [175] investigated the combined effects of surface topography and flow-induced shear stress on the neuronal differentiation of human mesenchymal stem cells (hMSCs). They applied different shear stresses in a PDMS substrate with micrometric grooves. An increased directionality under flow conditions was observed. Moreover, an increased neurite length was noticed on the seventh day. However, a significant decrease in neurite length was observed on the tenth day. These results were not conclusive on how the combined effect of shear stress and topography affects neuronal growth. It should also be emphasized that in both studies, the flow was not continuous but was rather applied for only a few hours per culture day. As a result, the *in vivo* dynamic culture conditions may not be adequately simulated *in vitro.*

Table 1.4 summarizes the reported studies on the combined effect of microfluidic flow and topography on neuronal response.

Table 1.4: *Reported studies on the combined effect of microfluidic flow and topography on nerve cell morphology/response.*

Substrate	Fabrication technique	Cell type	Circulating Flow?	Shear stress	Findings	Disadvantages	Ref.
Poly(lactic-co-glycolic acid) (PLGA) nanofiber-based substrate	Electrospinning	Human induced pluripotent stem cells (hiPSCs)	No	-	▪ Increase of β-tubulin III gene expression ▪ Decrease of glial fibrillary acidic protein (GFAP) gene expression	▪ Animals receiving this implant showed functional improvement but no significant difference with the control group	[174]
PLGA microfiber-based substrate	Electrospinning	Adrenal pheochromocytoma (PC12) cells	Yes	▪ 0.1-1.5 Pa for 2 hours, 3 times per day for 2 days	▪ 0.25 Pa: Increased neurite length ▪ 0.5 Pa: Increased cellular alignment	▪ Not continuous flow	[57]
Polydimethylsiloxane (PDMS) substrate with micrometric grooves	Photolithography	Human mesenchymal stem cells (hMSCs)	Yes	▪ 0.1 and 0.25 Pa for 3 hours per day for 2 days	▪ 0.1 Pa: Increased neurite length at day7	▪ Not continuous flow ▪ Decrease of neurite length at day10	[175]

1.10 Aim of this study

Due to the dysfunctional spontaneous recovery of the nervous system after injury, the successful guidance of neuronal outgrowth, *in vitro*, is mandatory for neurogenesis. Therefore, the development of successful methods to guide neuronal outgrowth in a controllable manner, *in vitro*, is of great importance. It has been well-reported, as previously described in section 1.7, that surface topography affects the neuronal growth, orientation, and differentiation. However, the combined effect of flow-induced shear stress and surface topography on neuronal outgrowth has been rarely reported, as previously described in section 1.9 [57,175]. Nevertheless, these results were not conclusive on how the combined effect of shear stress and topography affects neuronal growth. Moreover, the main limitation in these studies was that the flow was not continuous but it was applied only for some hours per day. As a consequence, the *in vivo* dynamic culture conditions may not be adequately simulated *in vitro*. The ultimate goal of this work is to demonstrate an *in vitro* biomimetic dynamic cell culture model to promote neurogenesis.

Here we present a unique approach to realize such a guidance control on neuronal cell outgrowth, based on the combined effect of flow-induced shear stress and surface topography. Towards this aim, an interdisciplinary approach is implemented, where laser engineering, dynamic flow rate cell cultures, and computational flow simulations are employed to assess the synergistic or antagonistic effect of shear stress and scaffold topography on neuronal cell outgrowth, orientation, length, and differentiation.

For this purpose, polymeric, PET, microstructured substrates with different geometries (microgrooves, chess, net) have been prepared by ultrafast laser structuring. The laser-microstructured substrates have been characterized as to surface morphology, wetting properties, and surface chemistry. The geometries of microgrooves, chess, and net have been applied to *in vitro* static cell cultures before selecting the microgrooves for investigating the effect of shear stress.

A precise flow controlled microfluidic system with specific custom-designed chambers, incorporating laser-microstructured PET substrates comprising

microgrooves, was fabricated to assess the combined effect of shear stress and topography on neuronal outgrowth. The microgrooves were positioned either parallel or perpendicular to the direction of the flow. Additionally, the cell culture results were combined with computational flow simulations to calculate accurately the shear stress values.

The cell models used included fibroblast (NIH 3T3), Schwann (SW10), and neuronal (N2a) cell lines. In particular, NIH 3T3 cells were used as a well-studied and characterized experimental model for the study of cellular adhesion, proliferation, and orientation to optimize basic experimental parameters, such as the cell densities, days of culture, and flow rates. Since the neuronal survival and function are greatly dependent on the support of glial cells, Schwann (SW10) cells were used as important glial cells of the PNS. The combined effect of shear stress and topography on the adhesion, growth, and orientation of SW10 cells was investigated under dynamic culture conditions attained via continuous flow. In addition to this, N2a cells were used as a model system to study the combined effect of shear stress and topography on neuronal growth and differentiation. Finally, the effect of topography on the co-culture of SW10 and N2a cells was examined as it provides a more realistic environment of the actual structure of the PNS, including both the glial and neuronal-like cells.

The structure of this dissertation comprises an introduction to the experimental methods, presentation and discussion of the experimental findings followed by the conclusions.

2. Materials and Methods

2.1 Experimental setup used for the fabrication of laser-microstructured substrates

The microstructured substrates were fabricated via ultrafast laser direct writing of PET coverslips used for cell cultures (Sarstedt, Numbrecht, Germany). A Yb:KGW laser source was used with a wavelength of 1026 nm, 1 kHz repetition rate, and 170 fs pulse duration. The beam propagated through a half waveplate (HW) and a linear polarizer (LP) (which were used to vary the values of power), to a shutter (SW) (which was used to control the exposure time and thus the number of pulses receptive to the sample), then to a convex lens of 100 mm focal length, and, finally, to the sample (Figure 2.1). The laser-microstructured substrates were fabricated at a constant fluence of 11.9 J/cm^2 and scan velocity of 7 mm/s. By changing the x_{step} and y_{step} (which is the distance between two consecutive scan lines), three different geometries were created, defined as microgrooves (MG), chess, and net. The spacing and the width of the MG were 28.76 ± 0.50 μm and 28.68 ± 0.47 μm, respectively. The spacing of the chess was 24.52 ± 1.62 μm and the diameter of each chess piece was 21.91 ± 1.12 μm. The spacing of the net was 168.12 ± 1.38 μm. The total patterned area was 3 mm x 3 mm or 4 mm × 4 mm.
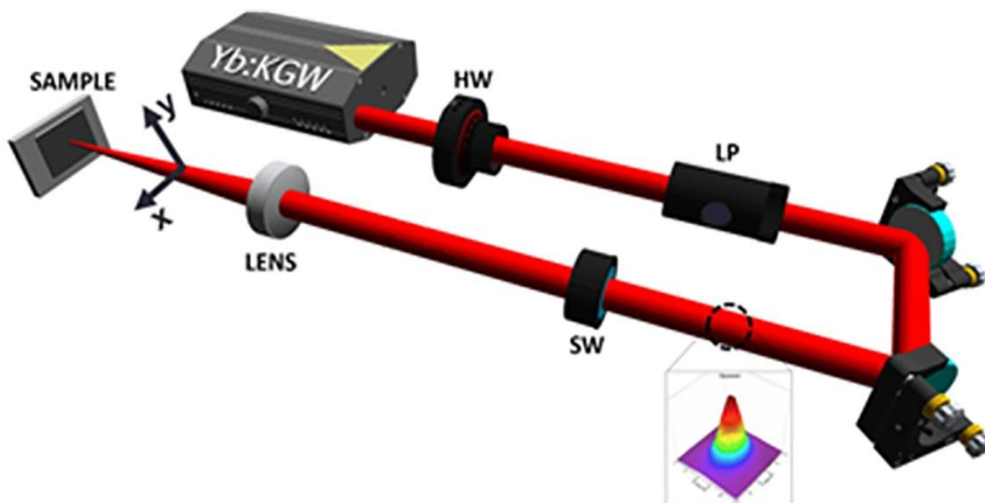
Figure 2.1: Experimental setup used for the fabrication of laser-microstructured substrates (modified by [176]*).*

2.2 Characterization of laser-microstructured substrates

2.2.1 Scanning Electron Microscopy (SEM)

Following the laser structuring process, the laser-microstructured substrates were sputter-coated with a 15 nm layer of gold (Baltec SCD 050, BAL-TEC AG, Balzers, Liechtenstein) and observed under a scanning electron microscope (JEOL JSM-6390 LV, Jeol USA Inc, Peabody, MA, USA) using an acceleration voltage of 15 kV.

2.2.2 Wettability measurements of laser-microstructured substrates

The contact angles of the laser-microstructured substrates and their relevant flat substrates were calculated via an automated tensiometer, using the sessile drop method [177]. A droplet of distilled, deionized Millipore water with a volume of 4 μL was positioned on the surface of the laser-microstructured substrates and their relevant flat substrates using a microsyringe. Afterward, images were taken to measure the angle formed at the liquid-solid interface. Depending on the contact angle value, the surface is characterized as hydrophilic ($< 90^{o}$) or hydrophobic ($> 90^{o}$). The surfaces of the laser-microstructured substrates being measured had a surface area of 4 mm x 4 mm. The mean value was calculated from at least three individual measurements. Successive measurements were reproducible within $\pm 1^{o}$.

2.2.3 Ultraviolet-visible (UV-Vis) measurements of laser-microstructured substrates

The ultraviolet-visible (UV-Vis) absorption spectra of the laser-microstructured substrates and their relevant flat substrates were measured with a LAMBDA 950

UV/VIS/NIR spectrophotometer from Perkin Elmer with a spectral range from 250 nm to 1200 nm.

2.2.4 Laser induced fluorescence (LIF) measurements of laser-microstructured substrates

The fluorescence spectra were collected by laser induced fluorescence (LIF) technique. The samples were induced by excitation at 248 nm with the output of a nanosecond excimer laser (KrF laser, Lambda-Physik EMG 201 MSC, Gottingen, Germany). The laser beam ($F_{Laser} \sim 10$ mJ/cm^2) was focused perpendicularly onto the sample. The fluorescence emission from the sample was collected by an optical fiber oriented nearly perpendicular to the sample, at ~2 cm away from its surface, and was spectrally analyzed in a 0.20 m grating spectrograph. The spectrum was recorded on a CCD camera (Andor iStar, Belfast, Northern Ireland). In each case, proper cutoff filters were employed to block any probe beam scattered light. The laser was operating with a repetition rate of 2 Hz and every spectrum is the accumulated fluorescence signal after 10 laser pulses of excitation. Laser-microstructured substrates and their relevant flat substrates were used for the measurements.

2.2.5 Raman measurements of laser-microstructured substrates

Raman spectroscopy of the laser-microstructured substrates and their relevant flat substrates was performed using a Nicolet Almega XR Raman spectrometer (Thermo Scientific) with a 780 nm laser as an excitation source. The Raman emission was collected in a back scattering geometry using a 50x objective.

2.3 Geometrical characterization of laser-microstructured substrates via image processing analysis

Fiji ImageJ, an image processing software, was used to analyze the geometrical characteristics of the laser-microstructured substrates. The aspect ratio of the MG, A, was calculated to be the ratio of the MG depth (d) to their width (w) (A = d/w).

The roughness ratio, r, was calculated to be the ratio of the actual, unfolded, surface area of MG to the total irradiated area$[r = 1 + (2d/w)]$.

2.4 Design of the microfluidic system

The microfluidic system (Figure 2.2a) is composed of an air compressor (Durr Technik, USA) and an OB1 pressure controller (pressure stability 0.005%) (Elveflow, France) which are connected, through silicon tubing, to the nutrient reservoirs (Elveflow, France). Then nutrient (in this case culture medium), through poly(tetrafluoroethylene) (PTFE) tubing (interior diameter 0.5 mm), moves to the flow sensors (Elveflow, France), which precisely control the flow rates, to the bubble traps (Elveflow, France), to the custom-made geometry chambers (Ebers, Spain) containing the laser-microstructured substrates with the cells and finally to the waste reservoirs (Elveflow, France). The MG were placed parallel or perpendicular to the direction of the flow inside the chambers. The chambers consist of polysulfone upper lids for loading cells (length: 6 mm, width: 6 mm, height: 13 mm) and for flowing fluids across the cells and the laser-microstructured substrates (length: 11 mm, width: 6 mm, height: 150 μm). The experiments were performed under continuous flow conditions. The chambers, as well as the waste reservoirs, were placed inside a 5% carbon dioxide (CO_2) incubator at $33^{o}C$ or $37^{o}C$ (depending on the cell line used), for the whole duration of the dynamic culture experiments. In this thesis, the terms "dynamic culture" and "dynamic condition" refer to the culture under flow-induced shear stress. The cross-section image of the chamber, containing the laser-microstructured substrates with the cells, where the flow occurs is also illustrated (Figure 2.2b).
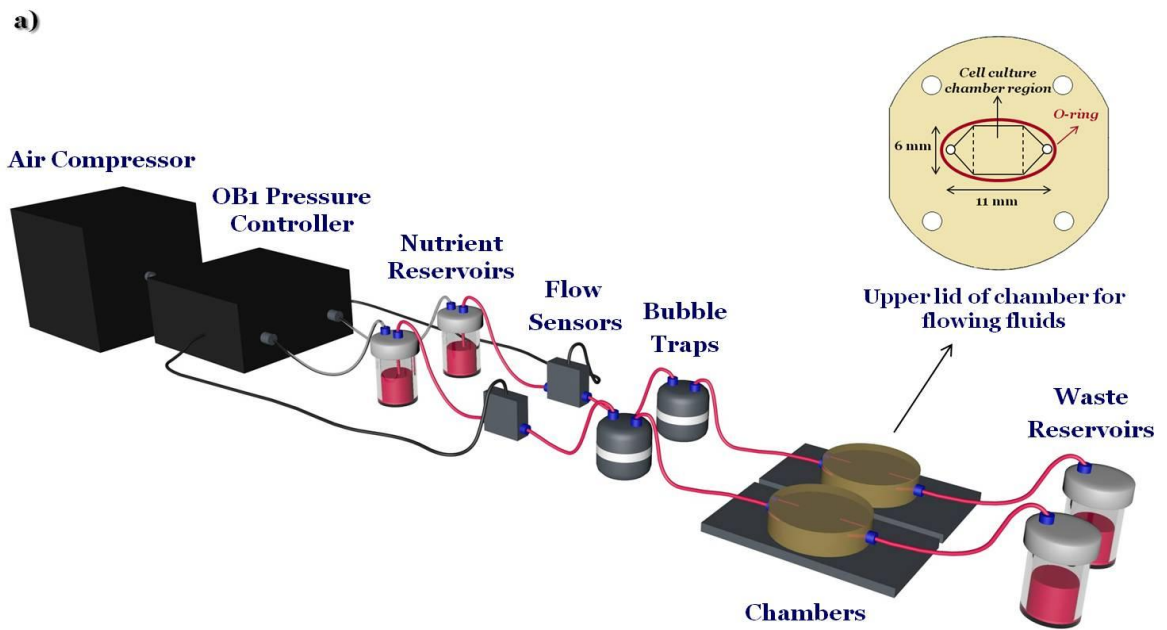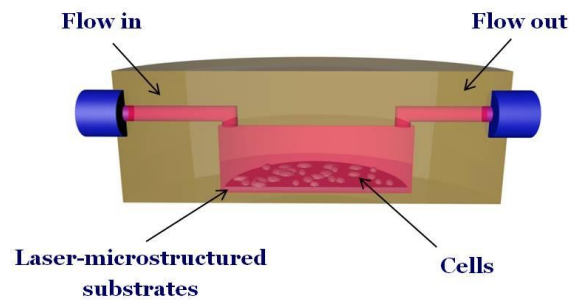
Figure 2.2: a) Schematic illustration of the custom-designed microfluidic system. It is composed of an air compressor and an OB1 pressure controller connected with nutrient reservoirs, flow sensors, bubble traps, a couple of chambers including the cells and the laser-microstructured substrates, and waste reservoirs. The upper lid of the chamber for flowing fluids across the cells and the laser-microstructured substrates is shown at the inset. Specifically, the length of the chamber's upper lid for flow is 11 mm and the width is 6 mm. The cell culture chamber region is pointed out in the dashed lines. b) Cross-section image of the chamber, containing the laser-microstructured substrates and cells, where the flow occurs.

2.5 Computational flow simulations in the microfluidic system chamber *(in collaboration with Dr. Yannis Papaharilaou)*

The commercial software ICEM-CFD v12.1 (Ansys Inc.) was used to generate the mesh of the computational model. The computational grid for the flat substrate case contains 435K hexahedral elements and non-uniform grid node spacing to produce higher grid density at the inlet and outlet regions of the square-shaped cell culture region of the chamber (Figure 2.2a). Near wall grid refinement was imposed through a viscous layer adjacent to the walls to capture the velocity gradients in the boundary layer and resolve the wall shear stress. Straight tube extensions were added to the inlet and outlet of the microfluidic system chamber to prevent upstream and downstream contamination respectively of the chamber flow domain from flow disturbances caused by forced outflow boundary conditions or non-fully developed flow entering the chamber.

For the laser-microstructured substrate case the three-dimensional (3D) computational grid contains 1.5M hexahedral elements and non-uniform node spacing to produce near wall refinement and higher grid density within the MG that runs parallel to the mean flow direction. In the case where the MG are placed perpendicular to the mean flow direction symmetry of the geometry and periodicity of the MG is exploited to construct a two-dimensional (2D) computational grid with 240K elements. In both cases, it is assumed that flow is fully developed at the upstream boundary of the MG region.

The Navier-Stokes and continuity equations for incompressible steady laminar flow in the absence of body forces were solved using Fluent v12.1 (Ansys Inc.). For the flow field computations, the wall was assumed rigid and the fluid was modeled as incompressible Newtonian with a density of 1.0 g/cm^3 and a viscosity of 1.0 cP. A uniform velocity was applied perpendicular to the inlet boundary and a traction free boundary condition was applied at the outlet of the domain.

2.6 Cell lines used

2.6.1 NIH 3T3, mouse fibroblast cells

NIH 3T3 cells, a mouse fibroblast cell line, were grown in cell culture flasks using culture medium [Dulbecco's Modified Eagle's Medium (DMEM) (Invitrogen, Grand Island, NY, USA) supplemented with 10% Fetal Bovine Serum (FBS) (Biosera, Sussex, UK) and 1% antibiotic solution (Gibco, Invitrogen, Kalsruhe, Germany)] in a 5% CO_2 incubator (Thermo Scientific, OH, USA) at 37°C.

2.6.2 SW10, mouse Schwann cells

Mouse Schwann cell line (SW10), an established adherent neuronal cell line, was obtained from ATCC® (Code: CRL-2766™). SW10 cells were grown in cell culture flasks using culture medium [DMEM (Invitrogen, Grand Island, NY, USA) supplemented with 10% FBS (Biosera, Sussex, UK) and 1% antibiotic solution (Gibco, Invitrogen, Kalsruhe, Germany)] in a 5% CO_2 incubator (Thermo Scientific, OH, USA) at 33°C.

2.6.3 Neuro-2a (N2a), mouse neuroblastoma cells

N2a is a fast-growing mouse neuroblastoma cell line. N2a cells were grown in cell culture flasks using culture medium [DMEM (Invitrogen, Grand Island, NY, USA) supplemented with 10% FBS (Biosera, Sussex, UK) and 1% antibiotic solution (Gibco, Invitrogen, Kalsruhe, Germany)] in a 5% CO_2 incubator (Thermo Scientific, OH, USA) at 37°C.

2.7 Static and dynamic cultures

Prior to any experiment, the laser-microstructured substrates, the reservoirs, the bubble traps, and the chambers were UV-sterilized. Subsequently, the substrates were transferred into sterile wells of 24-well plates (Sarstedt, Numbrecht, Germany) for

static cultures or/and inside the chambers of the microfluidic system for dynamic cultures. Planar PET coverslips for cell cultures (Sarstedt, Numbrecht, Germany) were used as the control samples.

2.7.1 *In vitro* experiments with NIH 3T3 cells

For the static cultures, 2.5×10^4 or 5×10^4 NIH 3T3 cells/1.9 cm^2 were seeded on the planar PET coverslips or the laser-microstructured substrates (MG, chess, net) and were cultured for a series of different time periods ranging from 1 to 6 days (1 day, 4 days, 6 days).

For the dynamic cultures, a series of different cell numbers (1.5×10^4 or 2.5×10^4 or 5×10^4 cells/0.36 cm^2) were seeded on the planar PET coverslips, placed inside the chamber, and kept at rest overnight in a 5% CO_2 incubator at 37°C. The next day, the continuous perfusion was initiated and lasted for 2 days. Flow rates of 15, 30, 60, and 120 μL/min were used. At higher flow rate values cells detached from the coverslips.

The mean velocity, ū, in the microfluidic system is estimated by the equation [178]:

$$\bar{u} = (4Q)/(\pi d^2)$$

where Q is the flow rate and d is the tubing diameter (d = 0.5 mm).

While, the shear stress, τ_w, exerted on the cell layer can be estimated in a simplistic approach, as previously described in section 1.4, by the equation [59,60]:

$$\tau_w = (6\mu Q)/(bh^2)$$

where μ is the nutrient's viscosity (μ ~ 0.01 gcm^{-1}s^{-1} [61,179]), Q is the flow rate, b is the width of the chamber's upper lid for flowing fluids (b = 6 mm) and h is the height of the chamber's upper lid for flowing fluids (h = 150 μm).

Table 2.1 shows the flow rates as well as the corresponding mean velocity and shear stresses in the microfluidic system.

Table 2.1: *Values for flow rate (Q), mean velocity* $[\bar{u} = (4Q)/(\pi d^2)]$, *and shear stress* $[\tau_w = (6\mu Q)/(bh^2)]$ *in the microfluidic system.*

Q (µL/min)	$\bar{u}$ (m/s)	σ (Pa)
15	0.0013	0.01
30	0.0025	0.02
60	0.0051	0.04
120	0.0102	0.09

2.7.2 *In vitro* experiments with SW10 cells

For the static cultures, 3×10^4 SW10 cells/1.9 cm^2 were seeded on the planar PET coverslips or the laser-microstructured substrates (MG, chess, net) and were cultured for 4 and 6 days.

Prior to dynamic cultures, the substrates were coated with a 15 µg/mL solution of laminin (Sigma-Aldrich, St. Louis, MO, USA) to enhance cell adhesion. A number of 2.5×10^4 cells/0.36 cm^2 were seeded on the planar PET coverslips or the MG, placed inside the chamber, and kept at rest overnight in a 5% CO_2 incubator at 33°C. The MG were placed parallel or perpendicular to the direction of the flow inside the chambers. The next day, the continuous perfusion was initiated and lasted for 2 days. Based on the previous results of NIH 3T3 cells and SW10 cells under static conditions, it was determined that it would be more effective to quantify the cell length after a 3-day culture period, as well as, selecting the geometry of MG for investigating the effect of shear stress.

To our knowledge, there are no available data on the shear stress values applied *in vivo* to the PNS cells. Additionally, although it is known [180] that there are small arteries, coined as *vasa nervorum*, providing blood supply to peripheral nerves, the velocity's values are unknown. Thus, based on the previous results of NIH 3T3 cells under dynamic conditions, the flow rates of 30, 50, and 200 µL/min were used. At higher flow rate values cells detached from the substrates.

Table 2.2 shows the flow rates as well as the corresponding mean velocity and shear stresses in the microfluidic system.

Table 2.2: Values for flow rate (Q), mean velocity $[\bar{u} = (4Q)/(\pi d^2)]$, and shear stress $[\tau_w = (6\mu Q)/(bh^2)]$ in the microfluidic system.

Q (µL/min)	ū (m/s)	σ (Pa)
30	0.0025	0.02
50	0.0042	0.04
200	0.0170	0.15

Moreover, 2.5×10^4 cells/1.9 cm^2 were seeded on the planar PET coverslips or the MG, which were coated with a 15 µg/mL solution of laminin (Sigma-Aldrich, St. Louis, MO, USA), and were cultured for 3 days under static conditions.

2.7.3 *In vitro* experiments with N2a cells

Prior to any culture, the substrates were coated with a 15 µg/mL solution of laminin (Sigma-Aldrich, St. Louis, MO, USA). For the static cultures, 3×10^4 N2a cells/1.9 cm^2 were seeded on the planar PET coverslips or the MG, and were cultured for 3 days. For the dynamic cultures, 3×10^4 cells/0.36 cm^2 cells were seeded on the planar PET coverslips or the MG, placed inside the chamber, and kept at rest overnight in a 5% CO$_2$ incubator at 37°C. The MG were placed parallel to the direction of the flow inside the chambers. The next day, the continuous perfusion was initiated and lasted for 2 days. Flow rates of 15 and 30 µL/min were used.

Table 2.3 shows the flow rates as well as the corresponding mean velocity and shear stresses in the microfluidic system.

Table 2.3: Values for flow rate (Q), mean velocity $[\bar{u} = (4Q)/(\pi d^2)]$, and shear stress $[\tau_w = (6\mu Q)/(bh^2)]$ in the microfluidic system.

Q (µL/min)	ū (m/s)	σ (Pa)
15	0.0013	0.01
30	0.0025	0.02

For the cell differentiation experiments, under static conditions, the culture medium was replaced with serum-free DMEM (Invitrogen, Grand Island, NY, USA) containing 1% antibiotic solution (Gibco, Invitrogen, Kalsruhe, Germany) or serum-free DMEM (Invitrogen, Grand Island, NY, USA) containing 1% antibiotic solution (Gibco, Invitrogen, Kalsruhe, Germany) and 300 μM cAMP (Sigma-Aldrich, St. Louis, MO, USA) after 24 hours of incubation. Under dynamic conditions, the culture medium was replaced with serum-free DMEM (Invitrogen, Grand Island, NY, USA) containing 1% antibiotic solution (Gibco, Invitrogen, Kalsruhe, Germany).

2.7.4 *In vitro* experiments with SW10 and N2a cells (co-culture)

3×10^4 SW10 cells/1.9 cm^2 and 3×10^4 N2a cells/1.9 cm^2 were seeded on the planar PET coverslips or the MG, coated with a 15 μg/mL solution of laminin (Sigma-Aldrich, St. Louis, MO, USA), and were cultured for 3 days, under static conditions, in a 5% CO_2 incubator at 37 ^{o}C.

For the cell differentiation experiments, the culture medium was replaced with DMEM (Invitrogen, Grand Island, NY, USA) containing 0.5% FBS (Biosera, Sussex, UK) and 1% antibiotic solution (Gibco, Invitrogen, Kalsruhe, Germany) or DMEM (Invitrogen, Grand Island, NY, USA) containing 0.5% FBS (Biosera, Sussex, UK), 1% antibiotic solution (Gibco, Invitrogen, Kalsruhe, Germany) and 300 μM cAMP (Sigma-Aldrich, St. Louis, MO, USA), after 24 hours of incubation. Serum-free DMEM inhibited the survival of SW10 cells.

2.8 Qualitative characterization of cell cultures

2.8.1 Live/dead assay

The viability of the attached cells on the planar PET coverslips or the laser-microstructured substrates was evaluated using the LIVE/DEAD™ Viability/Cytotoxicity Kit for mammalian cells (L3224, Thermo Scientific). In particular, after specific time periods of incubation, the samples were removed from the incubator and washed twice with phosphate buffered saline (PBS). A live/dead

solution was prepared by adding 20 μL of the supplied 2 mM ethidium homodimer-1 (EthD-1) stock solution to 10 mL of sterile PBS (thus reaching the desired concentration of 4 μM EthD-1 solution) and, after mixing thoroughly, 5 μL of the supplied 4 mM calcein acetoxymethyl (AM) stock solution was added to the 10 mL EthD-1 solution (thus reaching the desired concentration of 2 μM calcein AM solution). Live cells are distinguished by the presence of intracellular esterase activity, determined by the conversion of the virtually non-fluorescent cell-permeant calcein AM to the intensely green-fluorescent calcein, after acetoxymethyl ester hydrolysis by intracellular esterases. EthD-1 enters cells with damaged membranes and undergoes a 40-fold enhancement of fluorescence upon binding to nucleic acids, thus producing a bright red fluorescence in dead cells. EthD-1 is excluded by the intact plasma membrane of live cells [181]. The solution was added to the samples and was left for 1 hour at room temperature. Finally, the samples were washed once with PBS, and fluorescent images were obtained by an epifluorescence microscope coupled to a high-resolution Carl Zeiss Axiocam color camera. The objective of x10 was used.

2.8.2 SEM

The adhesion and the orientation of the cultured cells on the planar PET coverslips or the laser-microstructured substrates were examined by SEM. Specifically, the planar PET coverslips or the laser-microstructured substrates seeded with the cells were removed from the incubator at specific time periods, washed twice with 0.1 M sodium cacodylate buffer (SCB), and fixed with 2% glutaraldehyde (GDA) and 2% paraformaldehyde (PFA) in 0.1 M SCB for 30 minutes. Thereafter, they were washed twice with 0.1 M SCB and dehydrated in increasing concentrations (from 30 - 100%) of ethanol. Finally, they were dried in a critical point drier (Baltec CPD 030, BAL-TEC AG, Balzers, Liechtenstein), sputter-coated with a 15 nm layer of gold (Baltec SCD 050, BAL-TEC AG, Balzers, Liechtenstein), and observed under a scanning electron microscope (JEOL JSM-6390 LV, Jeol USA Inc, Peabody, MA, USA) at an accelerating voltage of 15 kV.

2.8.3 Immunocytochemical assays

A series of cell cultures on planar PET coverslips or laser-microstructured substrates were stained to study cell adhesion, proliferation, orientation, and differentiation.

To perform immunofluorescence staining, the samples were removed from the incubator and washed twice with PBS after specific time periods of incubation. Afterward, they were fixed with 4% PFA for 15 minutes and permeabilized with 0.1% Triton X-100 in PBS for 5 minutes. The non-specific binding sites were blocked with 2% bovine serum albumin (BSA) in PBS for 30 minutes.

The F-actin of the cytoskeleton and the double-stranded helical DNA of the cell nucleus were stained with phalloidin and 4',6-Diamidino-2-Phenylindole (DAPI), respectively. Actin is the major cytoskeletal protein of most cells. It is highly conserved and participates in various structural and functional roles [182]. In this case, actin exists as actin filaments (F-actin) and is stained with a specific phalloidin (Alexa Fluor® 568 Phalloidin or Alexa Fluor® 680 Phalloidin). The samples were incubated for 2 hours at room temperature with Alexa Fluor® 568 Phalloidin or Alexa Fluor® 680 Phalloidin (Invitrogen, Thermo Fisher Scientific) (1:250 in PBS-BSA 1%) for F-actin staining. Then, they were washed with PBS and put on coverslips with DAPI (Molecular Probes by Life Technologies, Carlsbad, CA, USA) for nuclei staining.

The TUJ1 (Merck, Germany), a marker of neuronal differentiation, was applied to the samples cultured with N2a cells (1:400 in PBS-BSA 1%) and they were incubated for 1 hour at room temperature. Afterward, they were washed with PBS and incubated for 1 hour at room temperature with anti-mouse CF®488A (Biotium, San Francisco, CA, USA) (1:400 in PBS-BSA 1%). Finally, they were washed with PBS and put on coverslips with DAPI (Molecular Probes by Life Technologies, Carlsbad, CA, USA) for nuclei staining.

In the co-culture system, the TUJ1 (Merck, Germany) was applied to the samples (1:400 in PBS-BSA 1%) and they were incubated for 1 hour at room temperature. Then, they were washed with PBS and incubated for 1 hour at room temperature with

anti-mouse CF®488A (Biotium, San Francisco, CA, USA) (1:400 in PBS-BSA 1%) and Alexa Fluor® 568 Phalloidin (Invitrogen, Thermo Fisher Scientific) (1:400 in PBS-BSA 1%) for F-actin staining. Finally, they were washed with PBS and put on coverslips with DAPI (Molecular Probes by Life Technologies, Carlsbad, CA, USA) for nuclei staining.

Cell imaging was performed using an epifluorescence microscope coupled to a high-resolution Carl Zeiss Axiocam color camera or a Leica SP8 inverted scanning confocal microscope. The objectives of x10, x20, and x40 were used. To obtain the images of cells both on the top of MG and inside the MG, the z-stack of the confocal microscope was used.

2.9 Quantitative characterization of cell cultures via image processing analysis

2.9.1 Cell viability on the laser-microstructured substrates

The number of live and dead cells on the planar PET coverslips or the laser-microstructured substrates was determined by counting cell nuclei stained with calcein and EthD-1 respectively. Nuclei number was assessed with Fiji ImageJ using the "Cell Counter" plug-in.

The percentage of live and dead cells on the samples was calculated using the equations:

$$\% \text{ Live cells} = \frac{\text{Total number of live cells}}{\text{Total number of live and dead cells}} \text{ x } 100$$

$$\% \text{ Dead cells} = \frac{\text{Total number of dead cells}}{\text{Total number of live and dead cells}} \text{ x } 100$$

The results represent the means of three different experiments.

2.9.2 Cell proliferation on the laser-microstructured substrates

The number of cells that were grown on the planar PET coverslips or the laser-microstructured substrates was determined by counting cell nuclei stained with DAPI. Nuclei number was assessed with Fiji ImageJ using the "Cell Counter" plug-in. The results represent the means of three different experiments.

2.9.3 Directional orientation of cells on the laser-microstructured substrates

To investigate changes in the directional orientation of cells on the laser-microstructured substrates, the "Local gradient orientation" for directionality was performed using the Fiji ImageJ plug-in "Directionality" [183]. On top of the histogram, the plug-in generates statistics on the highest peak found, which is fitted by a Gaussian function considering the periodic nature of the histogram. In the tables, the "Direction (^{o})" column reports the center of the Gaussian; the "Dispersion (^{o})" column refers to the standard deviation of the Gaussian; the "Amount" column presents the sum of the histogram from center-std to center+std, divided by the total sum of the histogram; the "Goodness" column indicates the goodness of the fit, where 1 is good, 0 is bad.

2.9.4 Directional orientation of cells' cytoskeleton on the laser-microstructured substrates

To investigate changes in the directional orientation of cells' cytoskeleton on the planar PET coverslips or the laser-microstructured substrates, the "Local gradient orientation" for directionality was performed using the Fiji ImageJ plug-in "Directionality" [183]. In this way, the data of the amount of cells, presented in the input image, in each direction was extracted and plotted as a polar plot. To compare the different cases, the cell population per angle was normalized with the maximum value in each case and expressed as normalized cell population.

2.9.5 Cell length on the laser-microstructured substrates

To determine the cell length on the planar PET coverslips or the laser-microstructured substrates, Fiji ImageJ and Harmony® software of Operetta High-Content Imaging System (Perkin Elmer) were used. The results represent the means of three different experiments.

2.10 Statistical analysis

Statistical analysis of the data was performed using post hoc Tukey HSD test. A p-value < 0.05 was considered significant. For each case investigated, a series of three different experiments have been performed.

3. Results

3.1 Laser-microstructured substrates

The laser-microstructured substrates were morphologically characterized by SEM. Figure 3.1 depicts the top-view SEM images of PET coverslips that were ablated by the femtosecond laser at a constant fluence of 11.9 J/cm^2 and scan velocity of 7 mm/s. Using a x_{step} of 50 μm, a x_{step} and y_{step} of 50 μm, and a x_{step} of 200 μm, the geometries of anisotropic continuous MG, isotropic discontinuous chess, and isotropic continuous net were fabricated, respectively. The tilted-view and cross-section SEM images of MG are presented in Figure 3.2.
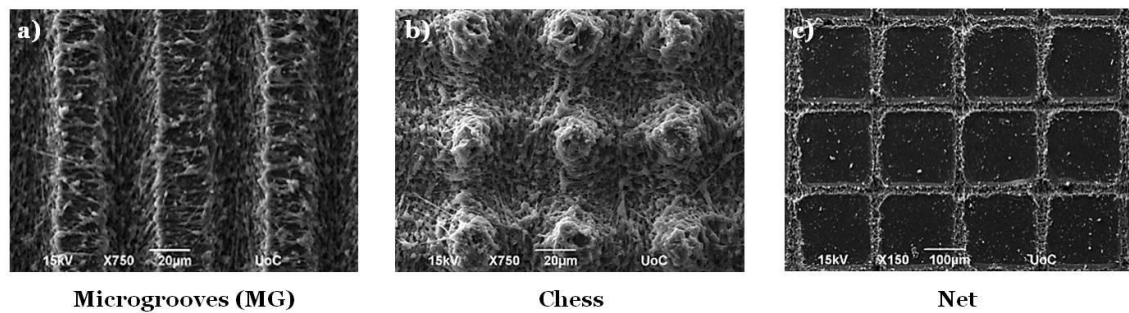
Figure 3.1: Scanning electron microscopy (SEM) images of laser-microstructured substrates on polyethylene terephthalate (PET) with different geometries [a) microgrooves (MG), b) chess, c) net].
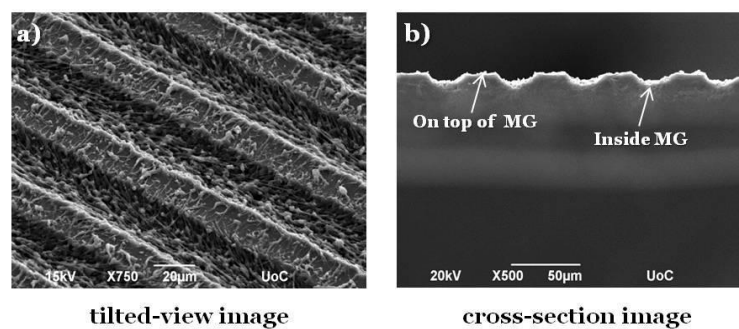
Figure 3.2: a) Tilted-view and b) cross-section SEM images of the polyethylene terephthalate microgrooved (PET-MG) substrates. The upper surface of the MG is termed as "On top of MG" while the inner surface as "Inside MG".

Table 3.1 illustrates the geometrical characteristics of laser-microstructured substrates, PET-MG, PET-Chess, and PET-Net.

Table 3.1: *Geometrical characteristics of laser-microstructured substrates (PET-MG, PET-Chess, PET-Net), spacing, width (w), and diameter of each chess piece.*

	Spacing (μm)	Width (w) (μm)	Diameter of each chess piece (μm)
PET-MG substrate	28.76 ± 0.50	28.68 ± 0.47 μm	-
PET-Chess substrate	24.52 ± 1.62	-	21.91 ± 1.12
PET-Net substrate	168.12 ± 1.38	-	-

Table 3.2 shows some additional geometrical characteristics of PET-MG substrates.

Table 3.2: *Geometrical characteristics of PET-MG substrates, depth (d), aspect ratio ($A = d/w$), and roughness ratio $[r = 1 + (2d/w)]$.*

PET-MG substrate	
Depth (d) (μm)	8.87 ± 0.44
Aspect ratio (A)	0.31 ± 0.01
Roughness ratio (r)	1.62 ± 0.02

3.2 Characterization of laser-microstructured substrates

3.2.1 Wettability measurements of laser-microstructured substrates

The contact angles measured on the irradiated PET with different geometries (PET-MG, PET-Chess, PET-Net), as well as, on the non-irradiated PET (PET-Flat) are presented in Figure 3.3. In particular, the contact angle of the PET-Flat was ~77.8^o (which is in agreement with previous studies [51,184]), while the contact angles of the

PET-MG, PET-Chess, and PET-Net were ~108.2^o, ~123.5^o, and ~127.6^o, respectively. A decrease in the hydrophilicity was observed on the irradiated PET with different geometries compared to the non-irradiated PET.
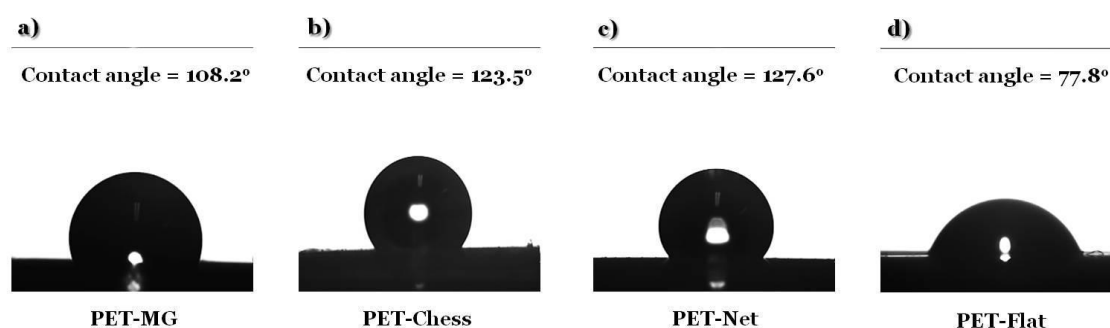
Figure 3.3: *Wettability measurements of irradiated PET with different geometries [a) PET-MG, b) PET-Chess, c) PET-Net], and non-irradiated PET [d) PET-Flat].*

3.2.2 UV-Vis measurements of laser-microstructured substrates

To determine changes to the surface chemistry of the laser-microstructured substrates, UV-Vis spectroscopy was performed. An increase of the absorption and the development of an absorption band were observed in the region of 300 - 500 nm in irradiated PET (PET-MG, PET-Chess), except PET-Net, compared to the non-irradiated PET (PET-Flat) (Figure 3.4).
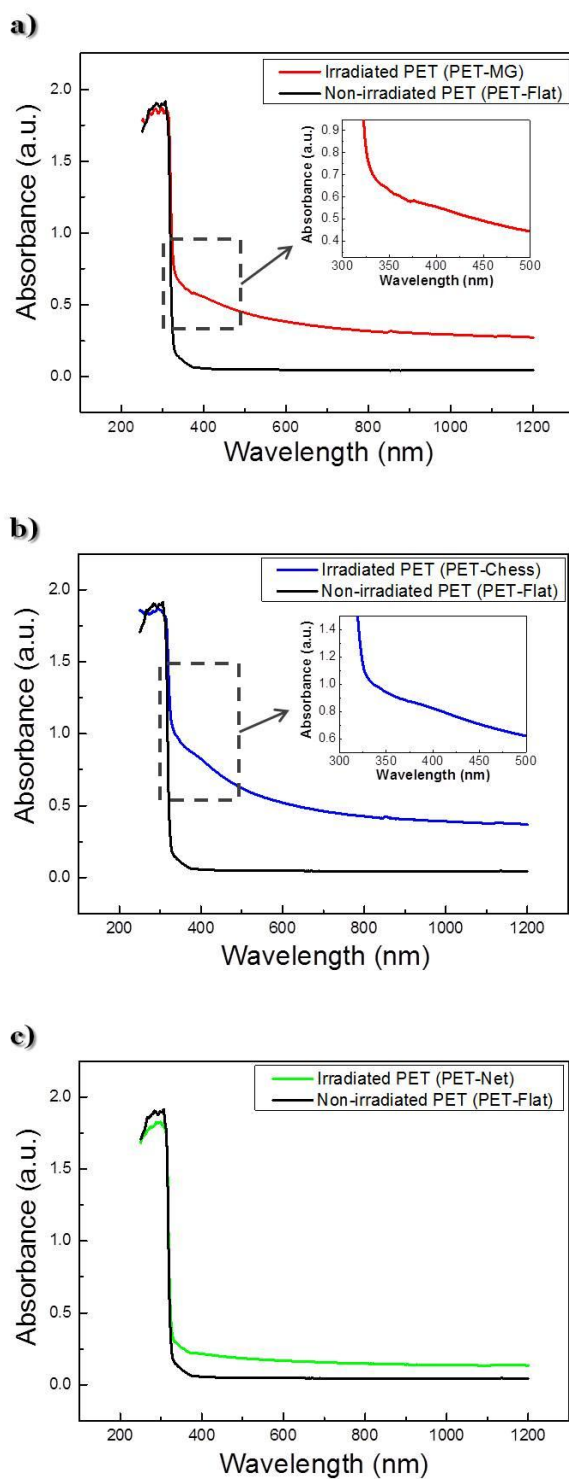
Figure 3.4: *UV-Vis measurements of irradiated PET with different geometries (PET-MG, PET-Chess, PET-Net), and non-irradiated PET (PET-Flat). Specifically, a) PET-MG (red line) – PET-Flat (black line), b) PET-Chess (blue line) – PET-Flat (black line), and c) PET-Net (green line) – PET-Flat (black line). The inset image shows the region of 300-500 nm in a) PET-MG and b) PET-Chess.*

3.2.3 LIF measurements of laser-microstructured substrates

To further assess the structural modification induced by the laser irradiation, the fluorescence spectra of the irradiated PET with different geometries (PET-MG, PET-Chess, PET-Net), as well as, the non-irradiated PET (PET-Flat) were recorded upon excitation at 248 nm with a KrF laser. In this case, the spectrum of the PET-Flat revealed a peak centered at ~460 nm. Additionally, a blue shift and a fluorescent increase in the PET-MG, PET-Chess, and PET-Net were observed compared to the PET-Flat (Figure 3.5).

a)

b)

c)
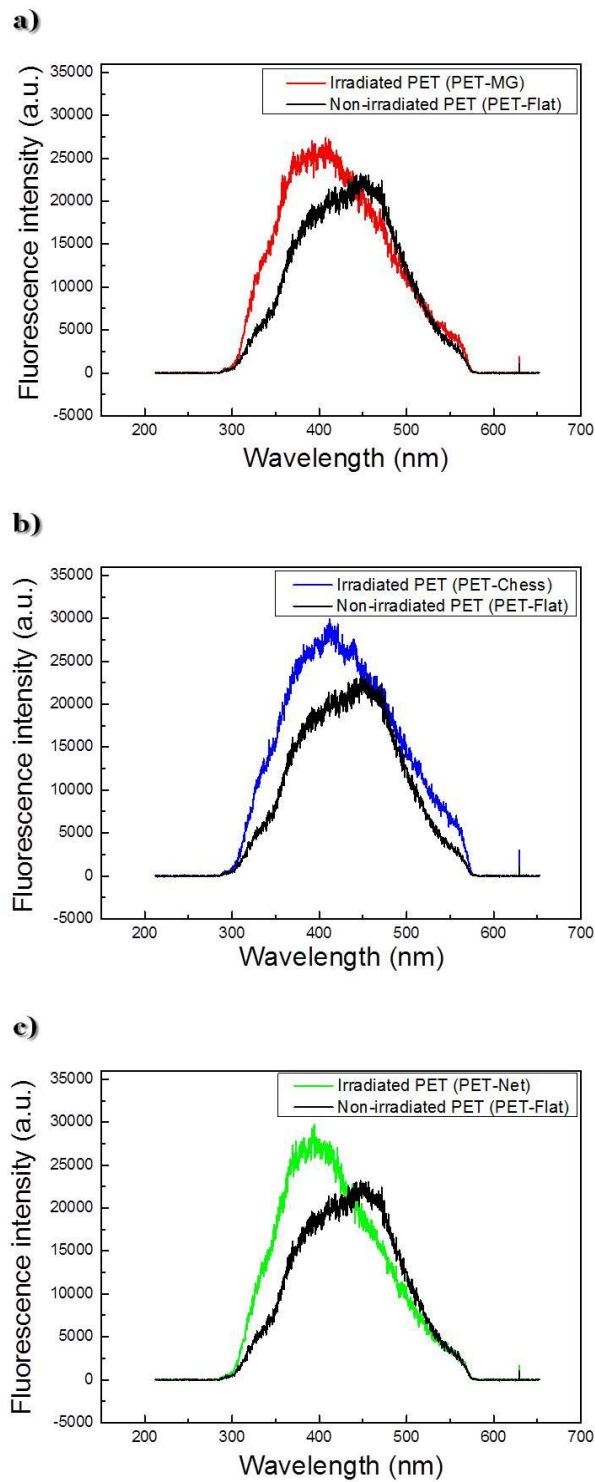
Figure 3.5: *LIF measurements of irradiated PET with different geometries (PET-MG, PET-Chess, PET-Net), and non-irradiated PET (PET-Flat). Specifically, a) PET-MG (red line) – PET-Flat (black line), b) PET-Chess (blue line) – PET-Flat (black line), and c) PET-Net (green line) – PET-Flat (black line).*

3.2.4 Raman measurements of laser-microstructured substrates

Raman spectroscopy, which also gives information on chemical changes [185], was performed to the irradiated PET with different geometries (PET-MG, PET-Chess, PET-Net), as well as, the non-irradiated PET (PET-Flat). An increase of the fluorescence background in the PET-MG, PET-Chess, and PET-Net was observed compared to the PET-Flat (Figure 3.6).

a)

b)

c)
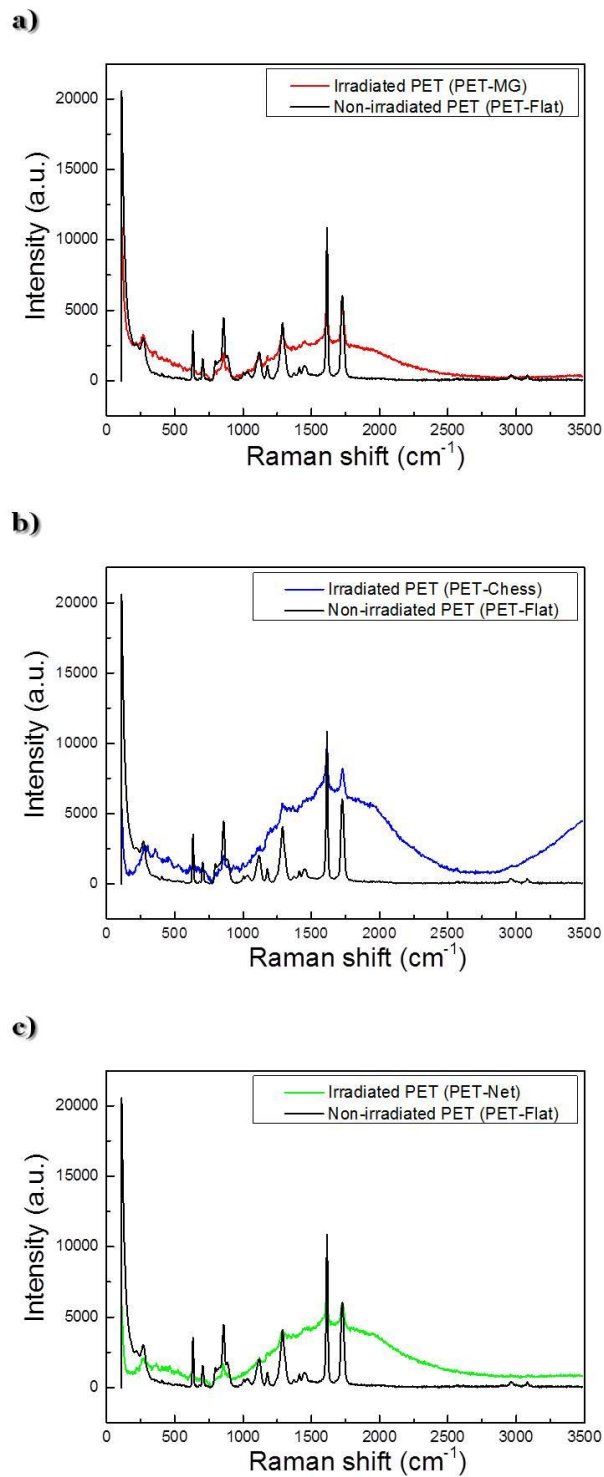
Figure 3.6: Raman measurements of irradiated PET with different geometries (PET-MG, PET-Chess, PET-Net), and non-irradiated PET (PET-Flat). Specifically, a) PET-MG (red line) – PET-Flat (black line), b) PET-Chess (blue line) – PET-Flat (black line), and c) PET-Net (green line) – PET-Flat (black line).

3.3 Numerically computed wall shear stress distribution in the microfluidic system chamber

Results from numerical simulations of the flow field in the microfluidic system chamber with steady flow at 30, 50, 120, and 200 µL/min flow rates for PET-Flat, as well as, 50 and 200 µL/min flow rates for PET-MG substrates are shown in Figure 3.7. The width and the maximum depth of the profile of MG applied to the flat substrate in the latter case were 29 µm and 9 µm respectively, as extracted from the respective SEM measurements (Figures 3.1a and 3.2). Exploiting the periodicity of the pattern of the microstructured substrate only part of the physical domain was modeled in the simulation to extract the primary features of the flow field. The simulated region, in the case where MG runs parallel to mean flow, includes a single MG and its lateral flat ridges which are assumed to be adjacent to the physical model symmetry plane. The wall shear stress distribution on the flat square cell culture substrate surface in the microfluidic system chamber indicates that the inlet and outlet triangular shaped regions of the physical model affect the velocity field in the square-shaped cell culture chamber region and reduce the area where cells are exposed to a uniform shear loading. This effect becomes more pronounced as the flow rate is increased.

The addition of MG parallel to flow direction increases the complexity of the flow field which becomes three-dimensional. Cells inside the MG of the PET-MG substrates will be exposed to lower wall shear stress compared to those on the top of MG. In the case where MG are parallel to the flow, a recirculation region develops as the flow enters and exits the microgrooved channel which is characterized by relatively low wall shear stress. In the case where MG are placed perpendicular to the flow, the computational domain can be reduced to 2 dimensions exploiting the symmetries in the microfluidic system chamber and the periodicity of the MG pattern. In this case, the strong variability of wall shear stress along the MG width is evident. A strong wall shear stress gradient develops at the edges of the MG perpendicular to the flow direction. Although the flow patterns are the same in both 50 and 200 µL/min cases the gradients are as expected larger in the higher flow rate case.
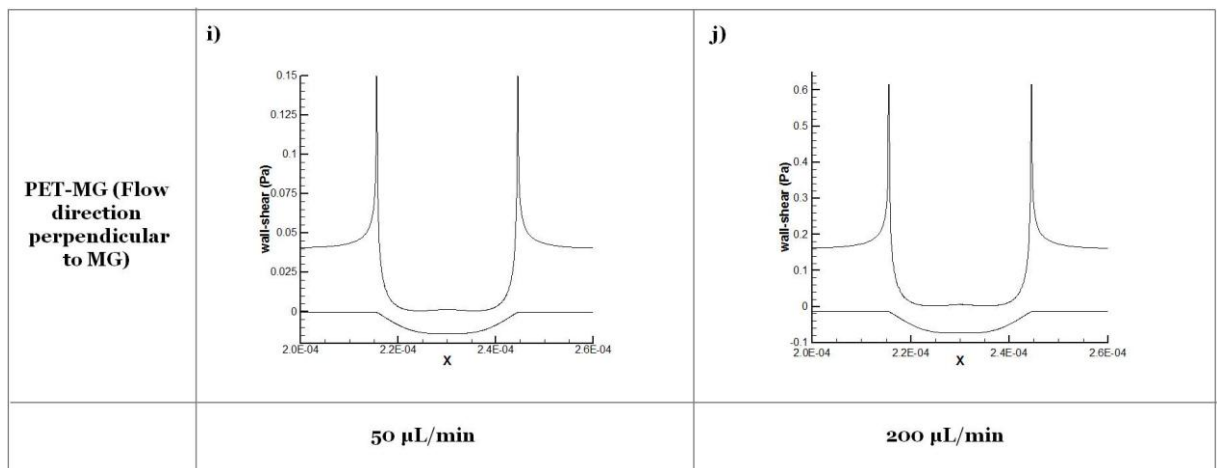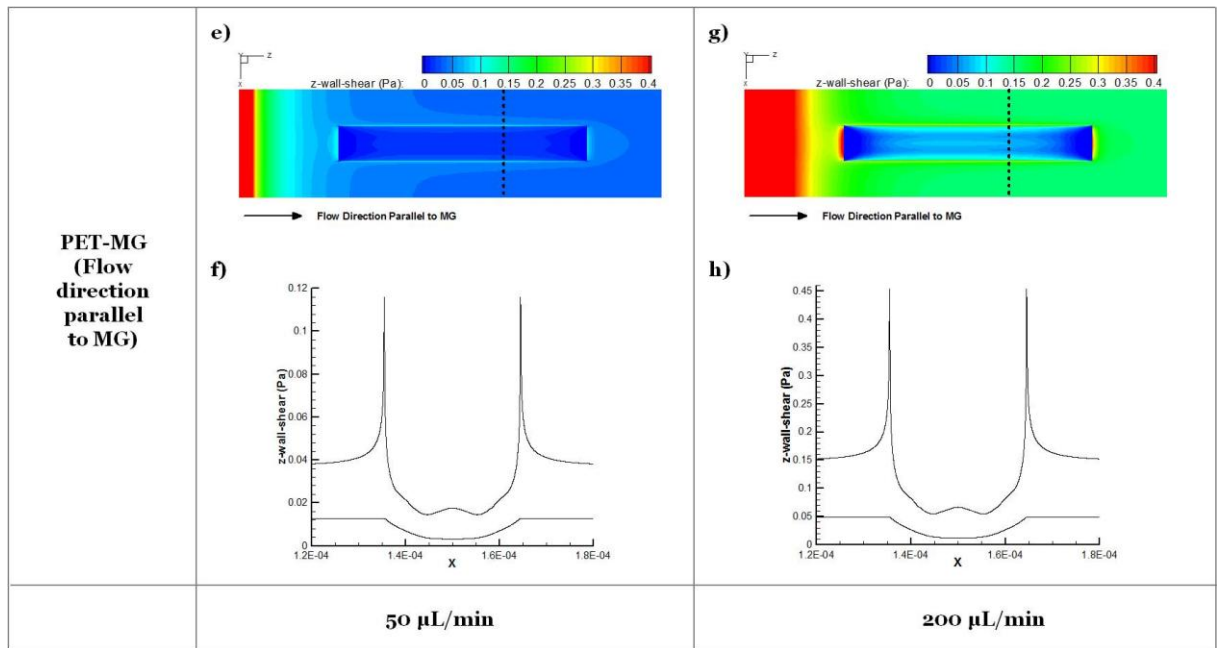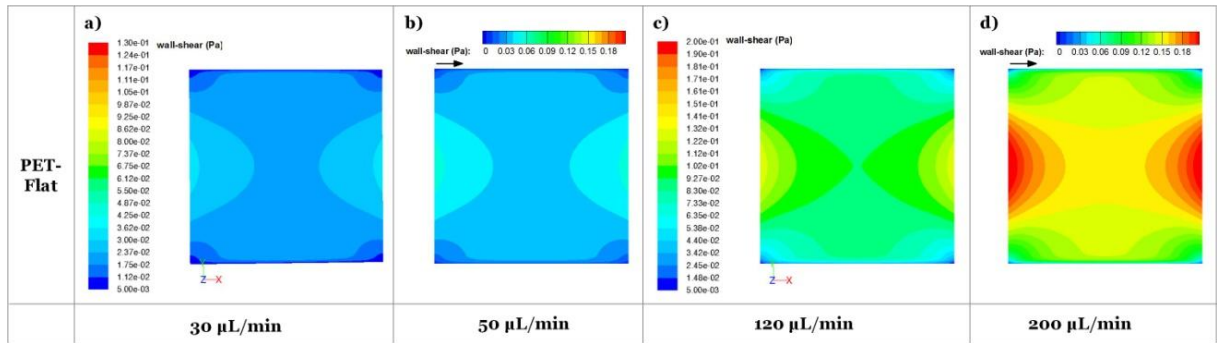
Figure 3.7: Contour plots on PET-Flat (a-d) or PET-MG substrates (e, g) and cross-section profiles (dotted line) (f, h, i, j) of computed wall shear stress for 30 (a), 50 (b, e, f, i), 120 (c), and 200 µL/min (d, g, h, j) flow rates. Microgrooves are parallel (e-h)

or perpendicular (i, j) to the flow direction. The lower curve in f, h, i, j depicts the modeled geometry of microgroove cross-section.

3.4 *In vitro* experiments with NIH 3T3 cells

3.4.1 Viability of NIH 3T3 cells on the laser-microstructured substrates under static conditions

Viability of the attached NIH 3T3 cells on the planar PET coverslips (PET-Flat) (Figures 3.8a-c) or the laser-microstructured substrates [PET-MG (Figures 3.8d-f), PET-Chess (Figures 3.8g-i), PET-Net (Figures 3.8j-l)] was evaluated using the live/dead assay on the first (Figures 3.8a, d, g, j), fourth (Figures 3.8b, e, h, k), and sixth (Figures 3.8c, f, i, l) day of culture, under static conditions. Particularly, this fluorescent assay facilitates counting the proportion of live (depicted with green color) and dead (depicted with red color) cells per unit area. In accordance with this assay, Figure 3.8 clearly shows that the percentage of live cells (~95% on average) was higher compared to dead cells (~5% on average) in all the different substrates and time periods.
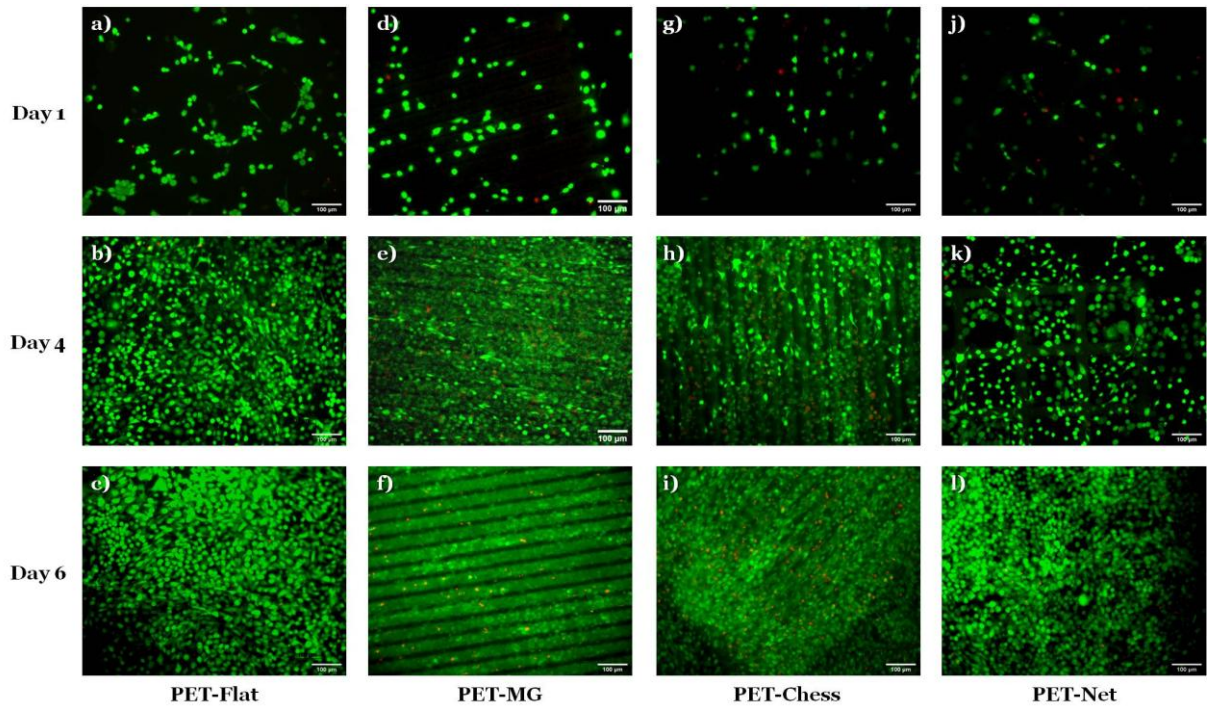
Figure 3.8: *Fluorescent images of NIH 3T3 cells cultured on the PET-Flat (a-c) or the laser-microstructured substrates [PET-MG (d-f), PET-Chess (g-i), PET-Net (j-l)], under static conditions, on the first (a, d, g, j), fourth (b, e, h, k), and sixth (c, f, i, l) day of culture. Live cells take non-fluorescent calcein and convert to green fluorescent calcein. Ethidium (EthD-1) only enters dead cells through damaged membranes producing red fluorescent. The number of live and dead cells was determined by counting cell nuclei stained with calcein and EthD-1 respectively. Nuclei number was assessed with Fiji ImageJ using the "Cell Counter" plug-in.*

3.4.2 Growth of NIH 3T3 cells on the laser-microstructured substrates under static conditions

Figure 3.9 illustrates the morphology of NIH 3T3 cells cultured on the PET-Flat (Figures 3.9a-c) or the laser-microstructured substrates [PET-MG (Figures 3.9d-f), PET-Chess (Figures 3.9g-i), PET-Net (Figures 3.9j-l)], under static conditions, for three different time periods [1 day (Figures 3.9a, d, g, j), 4 days (Figures 3.9b, e, h, k), 6 days (Figures 3.9c, f, i, l)] to control the cell adhesion and substrate. We observed, in all cases, that the cells exhibited a branched shape and flattened morphology with long cellular extensions, indicating good adhesion and growth of the cells both on the PET-Flat and the laser-microstructured substrates. Interestingly, cells appeared to be oriented along the direction of the MG for 4 and 6 days of culture, while they showed a random orientation on the other geometries (PET-Chess, PET-Net), as well as, on the PET-Flat.
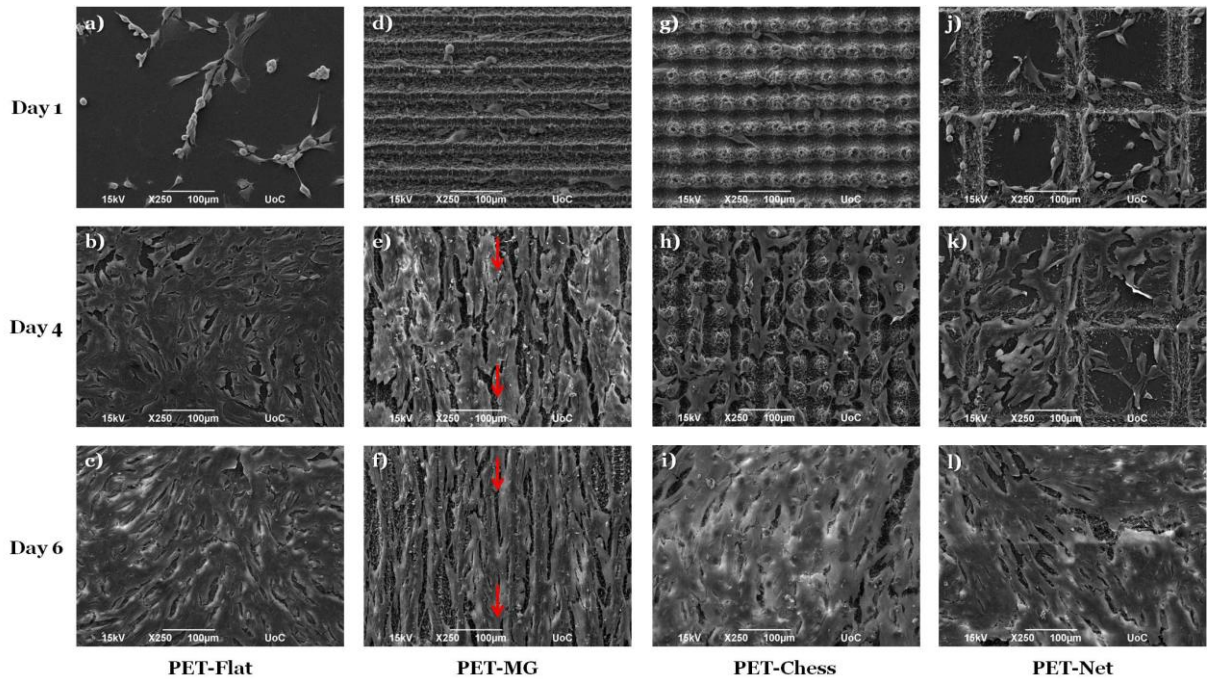
Figure 3.9: *SEM images of NIH 3T3 cells cultured on the PET-Flat (a-c) or the laser-microstructured substrates [PET-MG (d-f), PET-Chess (g-i), PET-Net (j-l)], under static conditions, on the first (a, d, g, j), fourth (b, e, h, k), and sixth (c, f, i, l) day of culture. The red arrows represent the directionality of cells, which are oriented according to the direction of the microgrooves.*

3.4.3 Orientation of NIH 3T3 cells' cytoskeleton on the laser-microstructured substrates [microgrooves (MG)] under static conditions

To examine the cytoskeleton arrangement of NIH 3T3 cells and their orientation on the PET-Flat and PET-MG substrates a series of immunocytochemical experiments were performed. Figure 3.10 presents the fluorescent images of NIH 3T3 cells cultured on the PET-Flat or PET-MG substrates, under static conditions, on the fourth and sixth day of culture. The actin filament of the cytoskeleton is visualized with red color, while the nuclei with blue color. We noticed that the cells' cytoskeleton was oriented parallel to the MG length for 4 and 6 days of culture, whereas an omnidirectional orientation was observed on the flat PET.
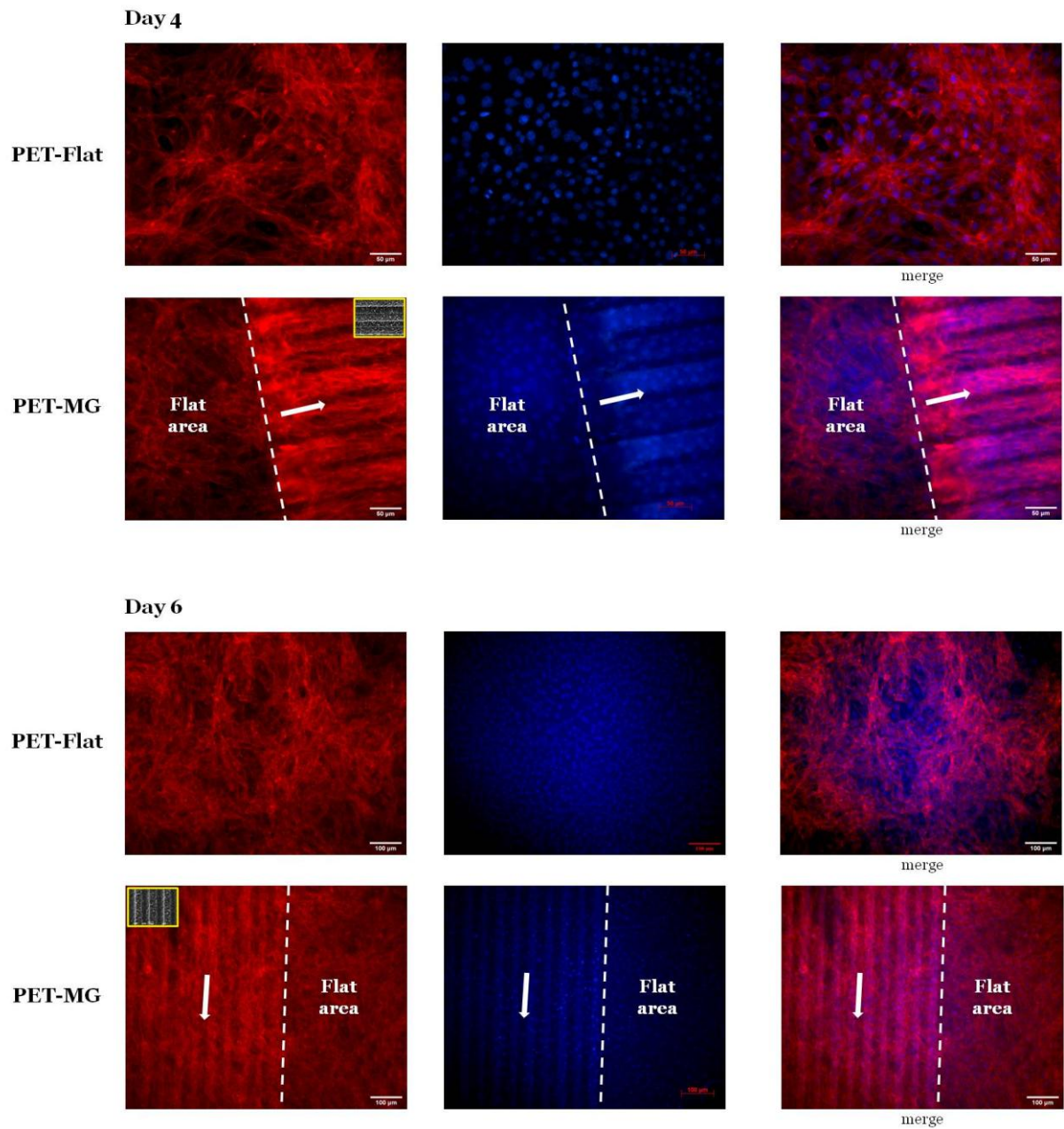
Figure 3.10: *Fluorescent images of NIH 3T3 cells cultured on the PET-Flat or PET-MG substrates, under static conditions, on the fourth and sixth day of culture. The cytoskeleton of the cells is visualized with red color (Alexa Fluor® 568 Phalloidin), while the nuclei with blue color (DAPI). The white arrows represent the directionality of cells, which are oriented according to the direction of the microgrooves. The inset SEM images, framed by a yellow box, depict the geometry of microgrooves.*

3.4.4 Growth of NIH 3T3 cells under dynamic conditions

In the dynamic experiments, we initially used NIH 3T3 cells, as a well-studied and characterized experimental model for the study of cellular adhesion, proliferation, and orientation to optimize the parameters (e.g. cell number, flow rate) of the experiment.

Figure 3.11 illustrates the NIH 3T3 cells [50000 cells/0.36 cm^2 (Figure 3.11a), 25000 cells/0.36 cm^2 (Figure 3.11b)] cultured on the PET-Flat substrates under dynamic conditions, applying the flow rates of 15 (Figure 3.11a) and 30 (Figure 3.11b) µL/min, on the third day of culture. We noticed that the cells adhered strongly and proliferated well on the PET-Flat, but no orientation was observed. Thus, we decreased the number of cells, 15000 cells/0.36 cm^2 (Figure 3.12), to examine if the lack of orientation was due to the cell number.

In particular, Figure 3.12 presents the NIH 3T3 cells (15000 cells/0.36 cm^2) cultured on the PET-Flat substrates under dynamic conditions, applying 30 (Figure 3.12a), 120 (Figure 3.12b), and 60 (Figure 3.12c) µL/min, on the third day of culture. However, by decreasing the cell number and applying the same flow rate (30 µL/min), cells proliferated well on the PET-Flat but similarly appeared to have a random orientation (Figure 3.12a). So, we increased the flow rate to examine if the cells will be oriented along the direction of the flow. However, by applying 120 (Figure 3.12b), and 60 µL/min (Figure 3.12c), cells detached from the PET-Flat.

Day 3

➢ 50000 cells/0.36 cm²

15 μL/min

➢ 25000 cells/0.36 cm²

30 μL/min

PET-Flat
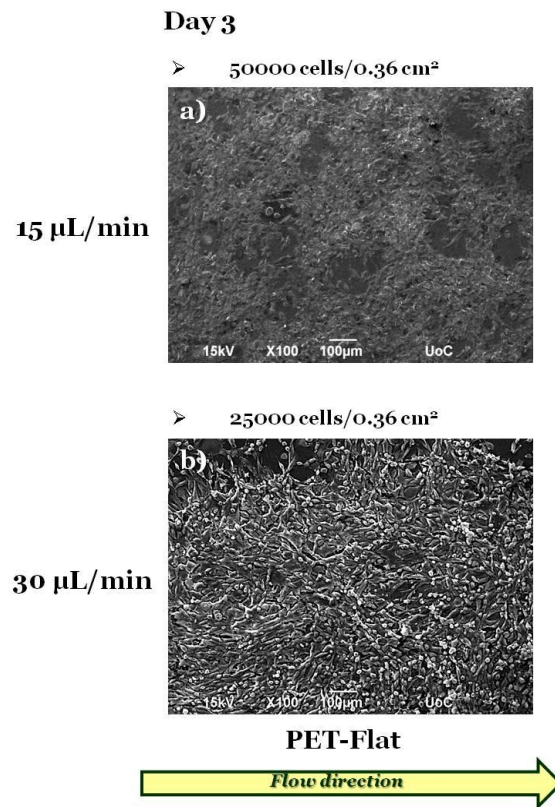
Flow direction

Figure 3.11: *SEM images of NIH 3T3 cells cultured on the PET-Flat substrates, under dynamic conditions, applying 15 (a) and 30 (b) μL/min on the third day of culture. The yellow arrow represents the direction of the flow.*

Day 3

  ➤   15000 cells/0.36 cm²

30 μL/min

120 μL/min

60 μL/min

PET-Flat
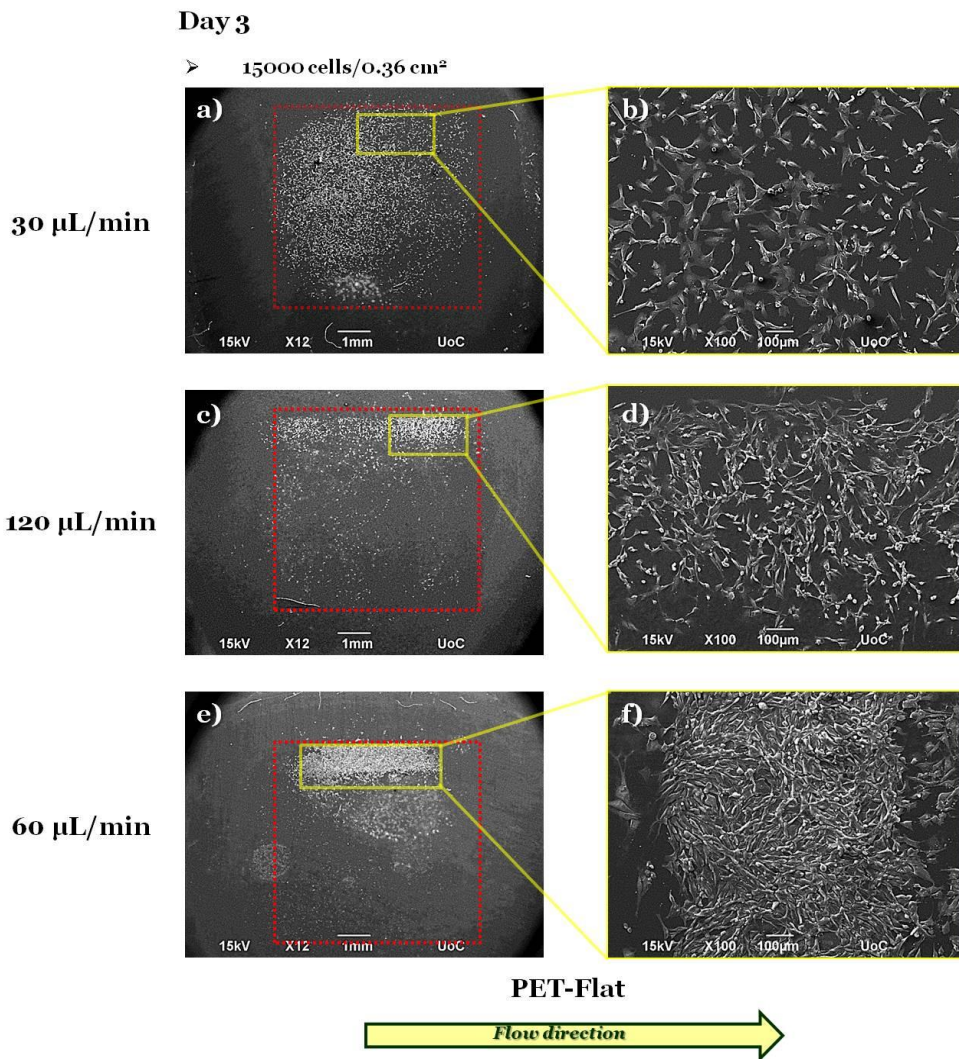
Flow direction

Figure 3.12: *SEM images of NIH 3T3 cells cultured on the PET-Flat substrates, under dynamic conditions, applying 30 (a, b), 120 (c, d), and 60 (e, f) μL/min on the third day of culture. The yellow arrow represents the direction of the flow. The cell culture chamber region is pointed out in the red dashed square areas. Images b, d, f are higher magnifications of the yellow parallelogram areas.*

3.5 *In vitro* experiments with SW10 cells

3.5.1 Growth of SW10 cells on the laser-microstructured substrates under static conditions

Figure 3.13 depicts the morphology of SW10 cells cultured on the PET-Flat (Figures 3.13a, b) or the laser-microstructured substrates [PET-MG (Figures 3.13c, d), PET-Chess (Figures 3.13e, f), PET-Net (Figures 3.13g, h)], under static conditions, on the fourth (Figures 3.13a, c, e, g), and sixth (Figures 3.13b, d, f, h) day of culture. In agreement with the previous study of NIH 3T3 cells (as previously described in section 3.4.2), SW10 cells appeared to be oriented parallel to the MG length for 4 and 6 days of culture while they showed an omnidirectional orientation on the other geometries (PET-Chess, PET-Net) and the PET-Flat. Thus, we decided to focus on the geometry of MG.
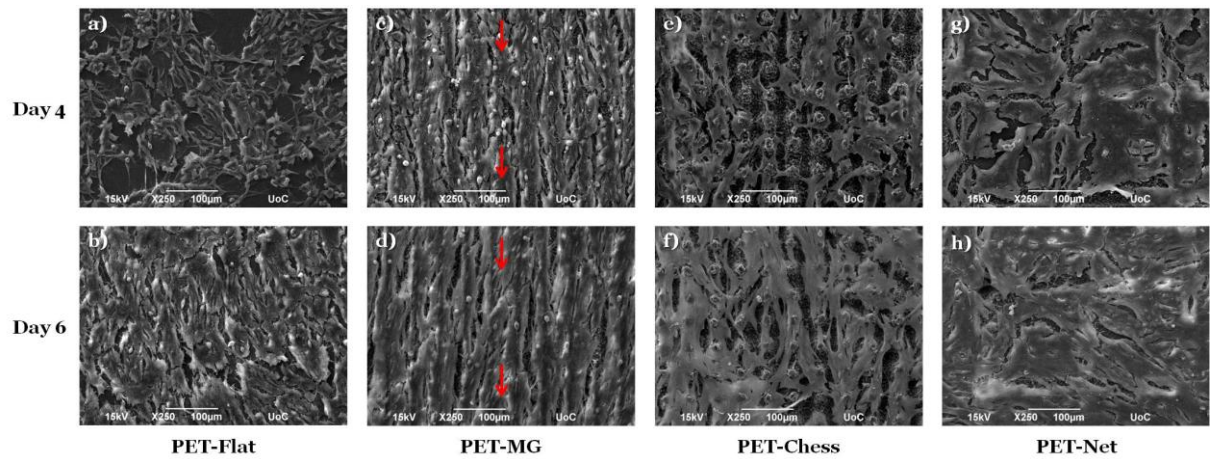
Figure 3.13: SEM images of SW10 cells cultured on the PET-Flat (a, b) or the laser-microstructured substrates [PET-MG (c, d), PET-Chess (e, f), PET-Net (g, h)], under static conditions, on the fourth (a, c, e, g), and sixth (b, d, f, h) day of culture. The red arrows represent the directionality of cells, which are oriented according to the direction of the microgrooves.

3.5.2 Orientation of SW10 cells on the laser-microstructured substrates (MG) under static conditions

To quantify the directional orientation of SW10 cells on the PET-MG substrates, under static conditions, on the fourth and sixth day of culture directionality histograms were performed (Figure 3.14). Indeed, the directionality histograms confirmed that the cells were oriented along the direction of the MG, showing that the

amount of cells (for both days) was higher in the domain parallel to the MG (±~90 degrees).
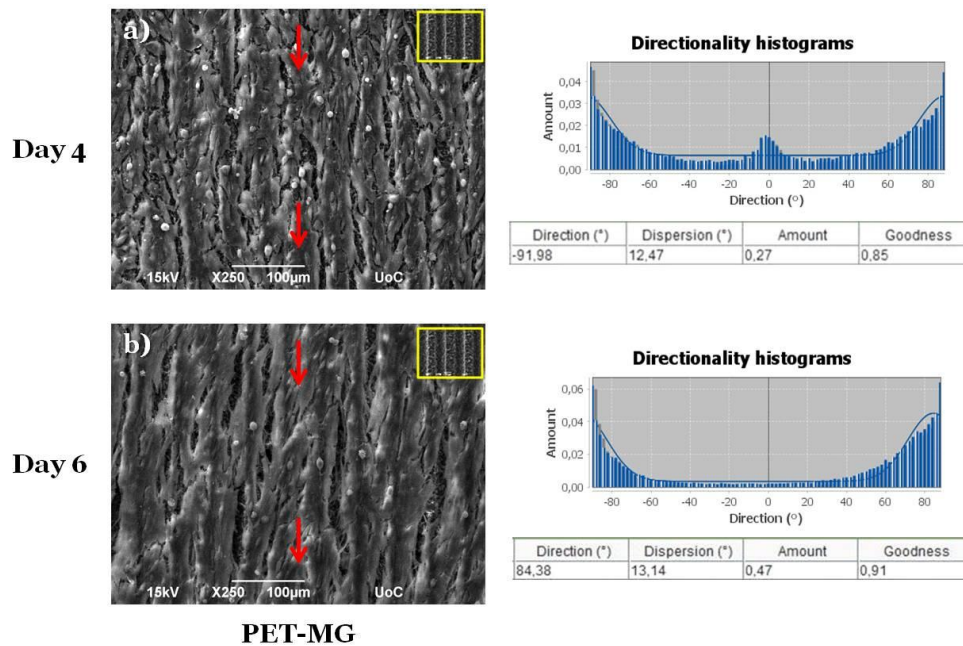
Figure 3.14: SEM images of SW10 cells cultured on the PET-MG substrates, under static conditions, on the fourth (a) and sixth (b) day of culture. The red arrows represent the directionality of cells, which are oriented according to the direction of the microgrooves. The inset SEM images, framed by a yellow box, depict the geometry of microgrooves. Next to the SEM images, directionality histograms and the tables with statistics are presented, which were generated using the Fiji ImageJ plug-in "Directionality" [183]. On top of the histogram, the plug-in generates statistics on the highest peak found, which is fitted by a Gaussian function considering the periodic nature of the histogram. In the tables, the "Direction (º)" column reports the center of the Gaussian; the "Dispersion (º)" column refers to the standard deviation of the Gaussian; the "Amount" column presents the sum of the histogram from center-std to center+std, divided by the total sum of the histogram; the "Goodness" column indicates the goodness of the fit, where 1 is good, 0 is bad.

3.5.3 Orientation of SW10 cells' cytoskeleton on the laser-microstructured substrates (MG) under static conditions

Figure 3.15 illustrates the fluorescent images of SW10 cells cultured on the PET-Flat or PET-MG substrates, under static conditions, on the fourth and sixth day of culture.

We observed that the cytoskeleton of SW10 cells was oriented parallel to the MG length direction, for 4 and 6 days, while it showed a random orientation on the flat PET, similarly to the previous study with NIH 3T3 cells (as previously described in section 3.4.3).
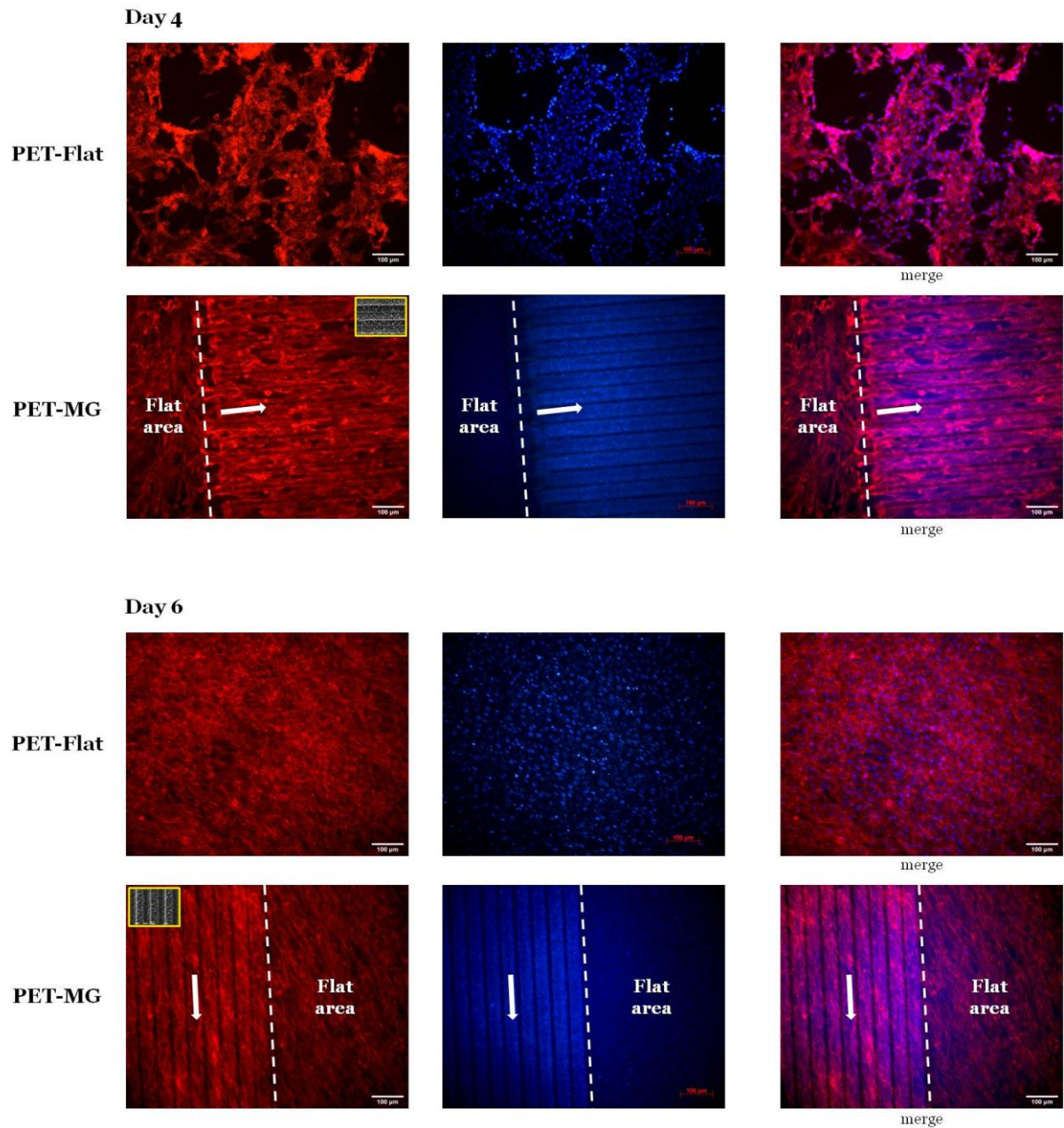
Figure 3.15: *Fluorescent images of SW10 cells cultured on the PET-Flat or PET-MG substrates, under static conditions, on the fourth and sixth day of culture. The cytoskeleton of the cells is visualized with red color (Alexa Fluor® 568 Phalloidin), while the nuclei with blue color (DAPI). The white arrows represent the directionality of cells, which are oriented*

according to the direction of the microgrooves. The inset SEM images, framed by a yellow box, depict the geometry of microgrooves.

3.5.4 Proliferation of SW10 cells on the laser-microstructured substrates (MG) under static conditions

The outgrowth of SW10 cells (number of cells/mm^2) on the PET-Flat and PET-MG substrates, under static conditions, was evaluated by counting cell nuclei stained with DAPI (Figure 3.15). Figure 3.16 depicts the mean cell number on the PET-Flat and PET-MG substrates for 4 and 6 days of culture. The cell outgrowth was increased on the MG compared to the PET-Flat, with a significant difference between 4 and 6 days at MG.
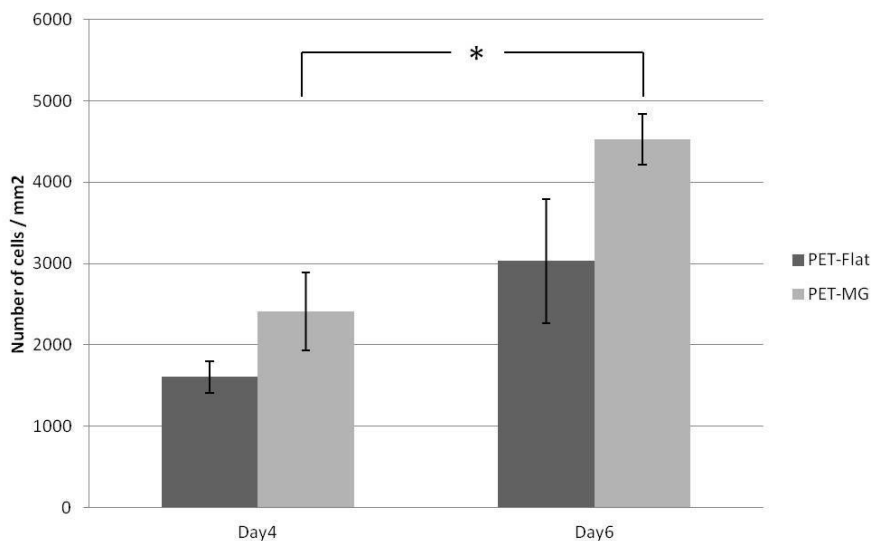
Figure 3.16: *Proliferation of SW10 cells (number of cells/mm^2) (via DAPI) on the PET-Flat and PET-MG substrates, under static conditions, on the fourth and sixth day of culture. Nuclei number was assessed with Fiji ImageJ using the "Cell Counter" plug-in. The statistical analysis of the data was performed using post hoc Tukey HSD test. A p-value < 0.05 was considered significant. A significant difference (* p<0.05) was observed between 4 days and 6 days for the PET-MG substrates.*

3.5.5 Growth of SW10 cells on the laser-microstructured substrates (MG) under static and dynamic conditions

After optimizing some basic parameters of the dynamic experiments using NIH 3T3 cells (as previously described in section 3.4.4), such as cell number (25000 cells/0.36 cm^2) and flow rate (starting point 30 μL/min) we performed the experiments using SW10 cells.

Specifically, Figure 3.17 presents the SW10 cells cultured on the PET-Flat (Figure 3.17a) or PET-MG (Figure 3.17b) substrates, under dynamic conditions, applying 30 μL/min on the third day of culture. By applying a flow rate of 30 μL/min, we noticed that the cells strongly adhered to the PET-Flat and PET-MG substrates and proliferated well. Furthermore, cells seemed to be oriented along the direction of the MG and parallel to flow while an omnidirectional orientation was observed on the flat PET. Consequently, we increased the flow rate to examine if the cells will be oriented on the PET-Flat.
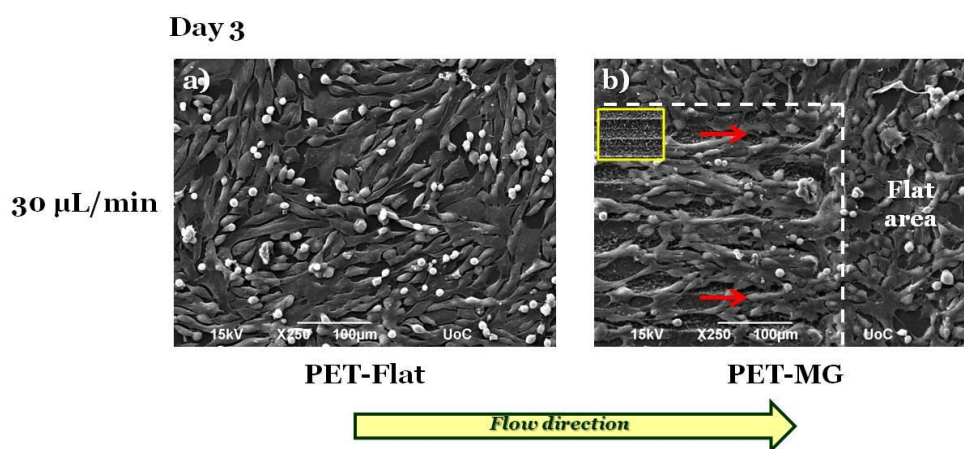
Figure 3.17: SEM images of SW10 cells cultured on the PET-Flat (a) or PET-MG (b) substrates, under dynamic conditions, applying 30 μL/min on the third day of culture. The red arrows represent the directionality of cells, which are oriented according to the direction of the microgrooves and parallel to flow. The inset SEM image, framed by a yellow box, depicts the geometry of microgrooves. The yellow arrow represents the direction of the flow.

Figures 3.18 and 3.19 illustrate the SW10 cells cultured on both types of substrates for static and dynamic culture conditions, under the flows of 50 and 200 μL/min, on

the third day of culture. We observed, in all cases, that the cells attached strongly and proliferated well on the substrates. Additionally, cells evenly adhered and proliferated both inside (Figure 3.18) as well as on top (Figure 3.19) of the MG of the PET-MG substrates.

In particular, Figures 3.18a-c depict the SW10 cells cultured on the PET-Flat substrates under static and dynamic conditions. Contrary to the case without flow, we observed a preferential orientation of the cytoskeleton parallel to the flow, which was more enhanced as the flow rate was increased.

Figures 3.18d-f and 3.19a-c show the SW10 cells cultured inside and on top of the MG of the PET-MG substrates, respectively, under static and dynamic conditions, where the flow was applied parallel to the MG length, at the rates of 50 and 200 μL/min. We noticed that in both static and dynamic culture conditions, the cytoskeleton was oriented parallel to the MG length direction.

Finally, by applying the same flow rates perpendicular to the MG length (Figures 3.18h, i and 3.19e, f), we observed that the SW10 cells' cytoskeleton orientation was practically unaffected and remained oriented along the MG.
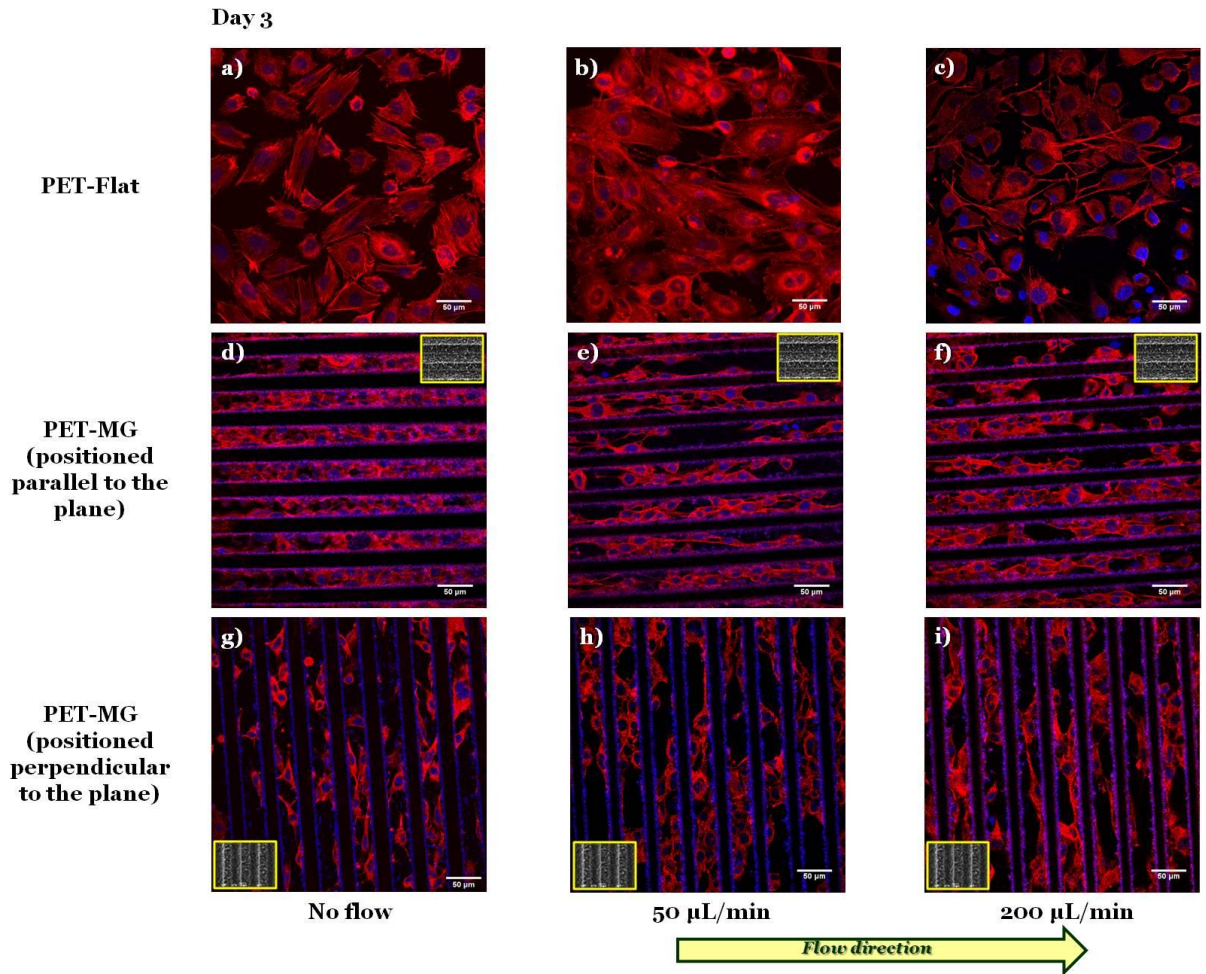
Figure 3.18: *Confocal images of SW10 cells cultured on the PET-Flat (a-c) or inside the MG of the PET-MG substrates (d-i), under static (a, d, g) or dynamic conditions, applying 50 (b, e, h) and 200 (c, f, i) μL/min, on the third day of culture. The cytoskeleton of the cells is visualized with red color (Alexa Fluor® 680 Phalloidin) while the nuclei with blue color (DAPI). The direction of the flow was parallel (e, f) or perpendicular (h, i) to the microgrooves. The inset SEM images, framed by a yellow box, depict the geometry of microgrooves. The yellow arrow represents the direction of the flow.*
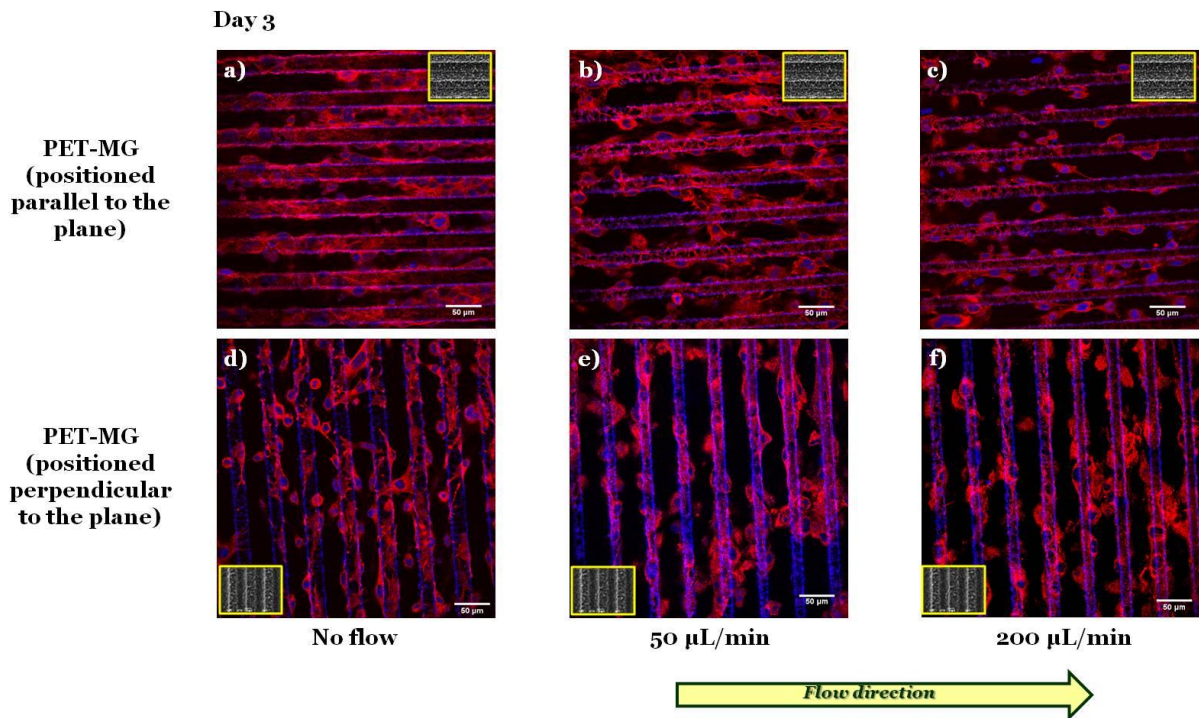
Figure 3.19: Confocal images of SW10 cells cultured on top of the MG of the PET-MG substrates under static (a, d) or dynamic conditions, applying 50 (b, e) and 200 (c, f) μL/min, on the third day of culture. The cytoskeleton of the cells is visualized with red color (Alexa Fluor® 680 Phalloidin) while the nuclei with blue color (DAPI). The direction of the flow was parallel (b, c) or perpendicular (e, f) to the microgrooves. The inset SEM images, framed by a yellow box, depict the geometry of microgrooves. The yellow arrow represents the direction of the flow.

3.5.6 Orientation of SW10 cells' cytoskeleton on the laser-microstructured substrates (MG) under static and dynamic conditions

The orientation of the SW10 cells' cytoskeleton on the PET-Flat or PET-MG substrates, under static and dynamic (50 and 200 μL/min) conditions, on the third day of culture has been extracted from the respective images (Figures 3.18 and 3.19) and plotted as polar plots depicted in Figures 3.20 and 3.21.

The directional polar plots of SW10 cells' cytoskeleton presented in Figure 3.20a confirmed the preferential orientation of cells' cytoskeleton parallel to flow, which was more enhanced from 50 to 200 μL/min, as well as, the random orientation in the

case without flow (Figures 3.18a-c). Specifically, the polar plot corresponding to the flow rate of 200 μL/min (Figure 3.20a, blue line), exhibited a much narrower distribution compared to 50 μL/min (Figure 3.20a, red line) at the direction of the flow, $\pm\sim15^{\circ}$. In contrast, under static culture conditions (Figure 3.20a, black line) the polar plot showed a broad distribution indicating an omnidirectional cell orientation.

In both static and dynamic culture conditions (flows of 50 and 200 μL/min parallel to the MG length), the cytoskeleton was oriented parallel to the MG length direction (Figure 3.18d-f and 3.19a-c). However, an enhanced cytoskeleton orientation was observed under dynamic culture conditions combined with the MG topography, as evidenced by the directional polar plots, illustrated in Figures 3.20b and 3.21a. Indeed, the normalized cell population under dynamic conditions, both inside (Figure 3.20b) and on top (Figure 3.21a) of the MG of the PET-MG substrates, exhibited a narrower distribution compared to the static cultures. This distribution did not seem to be affected by increasing the flow rate from 50 to 200 μL/min.

Finally, the directional polar plots, inside (Figure 3.20c) and on top (Figure 3.21b) of the MG of the PET-MG substrates, confirmed that by applying the same flow rates perpendicular to the MG length (Figures 3.18h, i and 3.19e, f), the cells' cytoskeleton orientation was practically unaffected and remained oriented along the MG.
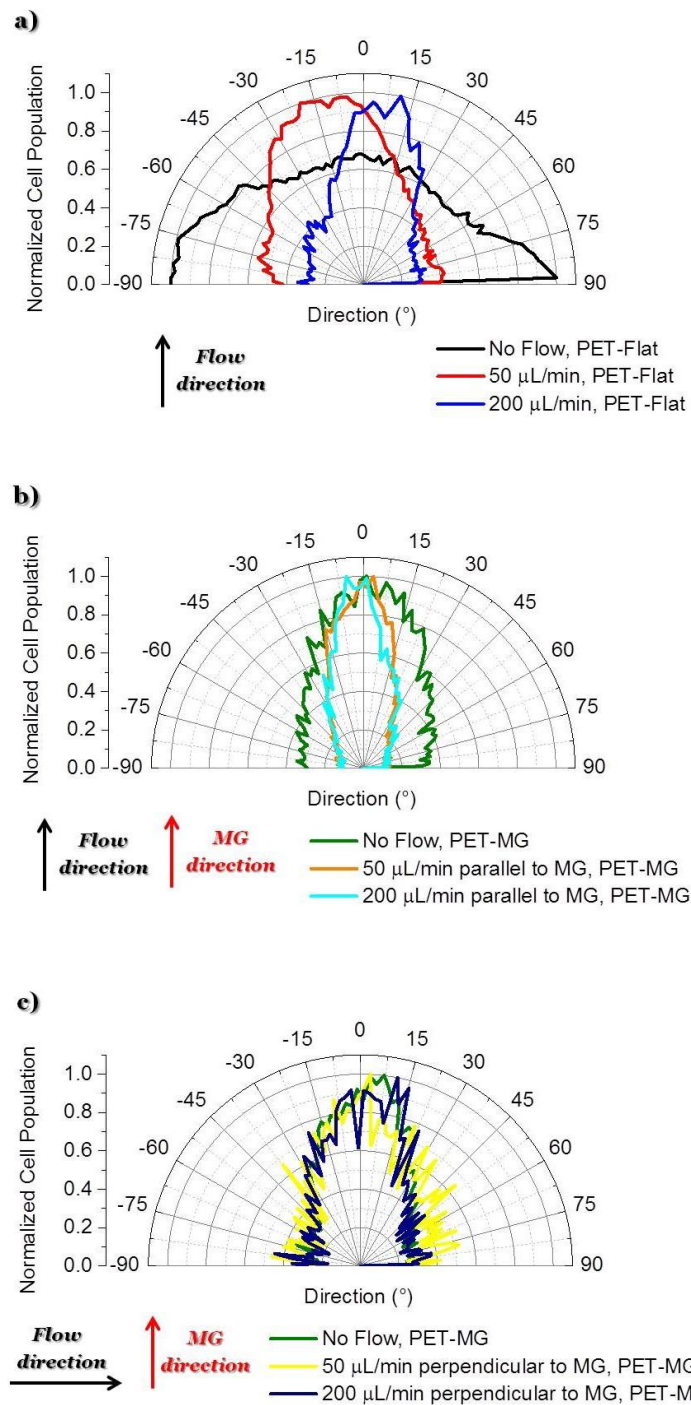
Figure 3.20: *Directional polar plots of cells' cytoskeleton on the PET-Flat or inside the MG of the PET-MG substrates. The directional polar plots were generated using the Fiji ImageJ plug-in "Directionality"* [183]. *In this way, the data of the amount of cells, presented in the input image, in each direction was extracted and plotted as a polar plot. To compare the different cases, the cell population per angle was normalized with the maximum value in each case and expressed as normalized cell population. Specifically: a) No flow, PET-Flat (black*

line) - 50 μL/min, PET-Flat (red line) - 200 μL/min, PET-Flat (blue line), b) No flow, PET-MG (green line) - 50 μL/min parallel to MG, PET-MG (orange line) - 200 μL/min parallel to MG, PET-MG (turquoise line), c) No flow, PET-MG (green line) - 50 μL/min perpendicular to MG, PET-MG (yellow line) - 200 μL/min perpendicular to MG, PET-MG (dark blue line). The black and red arrows represent the direction of the flow and the microgrooves, respectively. The statistical analysis of the data was performed using post hoc Tukey HSD test. A p-value < 0.05 was considered significant. In particular: a) No flow, PET-Flat is significantly different from 50 μL/min, PET-Flat and 200 μL/min, PET-Flat (** p<0.01). Moreover, 50 μL/min, PET-Flat is significantly different from 200 μL/min, PET-Flat (** p<0.01); b) No flow, PET-MG is significantly different from 50 μL/min parallel to MG, PET-MG and 200 μL/min parallel to MG, PET-MG (* p<0.05). No significant difference was observed between 50 μL/min parallel to MG, PET-MG and 200 μL/min parallel to MG, PET-MG; c) No significant difference was observed between No flow, PET-MG, 50 μL/min perpendicular to MG, PET-MG and 200 μL/min perpendicular to MG, PET-MG.
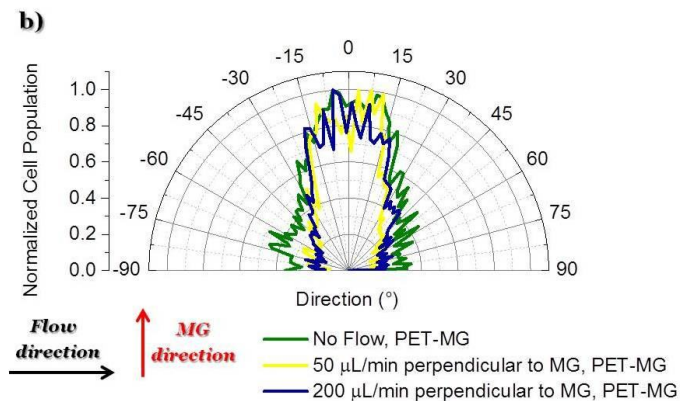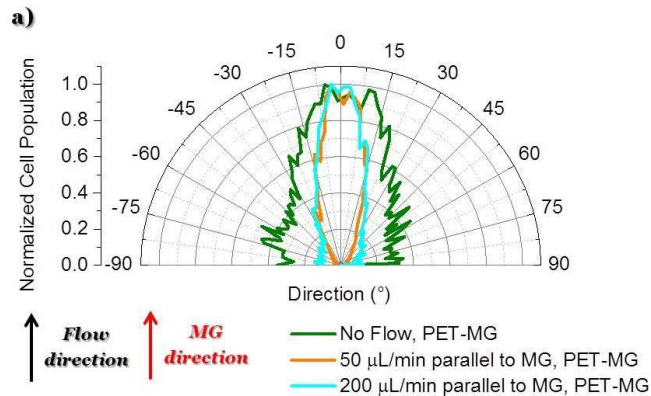
Figure 3.21: *Directional polar plots of cells' cytoskeleton on top of the MG of the PET-MG substrates. The directional polar plots were generated using the Fiji ImageJ plug-in "Directionality" [183]. In this way, the data of the amount of cells, presented in the input image, in each direction was extracted and plotted as a polar plot. To compare the different cases, the cell population per angle was normalized with the maximum value in each case and expressed as normalized cell population. Specifically: a) No flow, PET-MG (green line) - 50 μL/min parallel to MG, PET-MG (orange line) - 200 μL/min parallel to MG, PET-MG (turquoise line), b) No flow, PET-MG (green line) - 50 μL/min perpendicular to MG, PET-MG (yellow line) - 200 μL/min perpendicular to MG, PET-MG (dark blue line). The black and red arrows represent the direction of the flow and the microgrooves, respectively. The statistical analysis of the data was performed using post hoc Tukey HSD test. A p-value < 0.05 was considered significant. In particular: a) No flow, PET-MG is significantly different from 50 μL/min parallel to MG, PET-MG and 200 μL/min parallel to MG, PET-MG (* p<0.05). No significant difference was observed between 50 μL/min parallel to MG, PET-MG and 200 μL/min parallel to MG, PET-MG; b) No significant difference was observed between No flow, PET-MG, 50 μL/min perpendicular to MG, PET-MG and 200 μL/min perpendicular to MG, PET-MG.*

3.5.7 Elongation of SW10 cells on the laser-microstructured substrates (MG) under static and dynamic conditions

Figure 3.22 depicts the estimated length of SW10 cells on the PET-Flat and PET-MG substrates under static and dynamic culture conditions. We observed that the cell length, on the PET-Flat substrate, under the flow rate of 50 μL/min was significantly higher compared to the static cultures (Figure 3.22a). While a further elongation of the cytoskeleton was observed upon increasing the flow rate to 200 μL/min (Figure 3.22a). More importantly, the cell length was further enhanced upon dynamic culture conditions combined with the MG topography (Figure 3.22b). On the contrary, the cell length tended to decrease upon a flow perpendicular to the MG (Figure 3.22c).
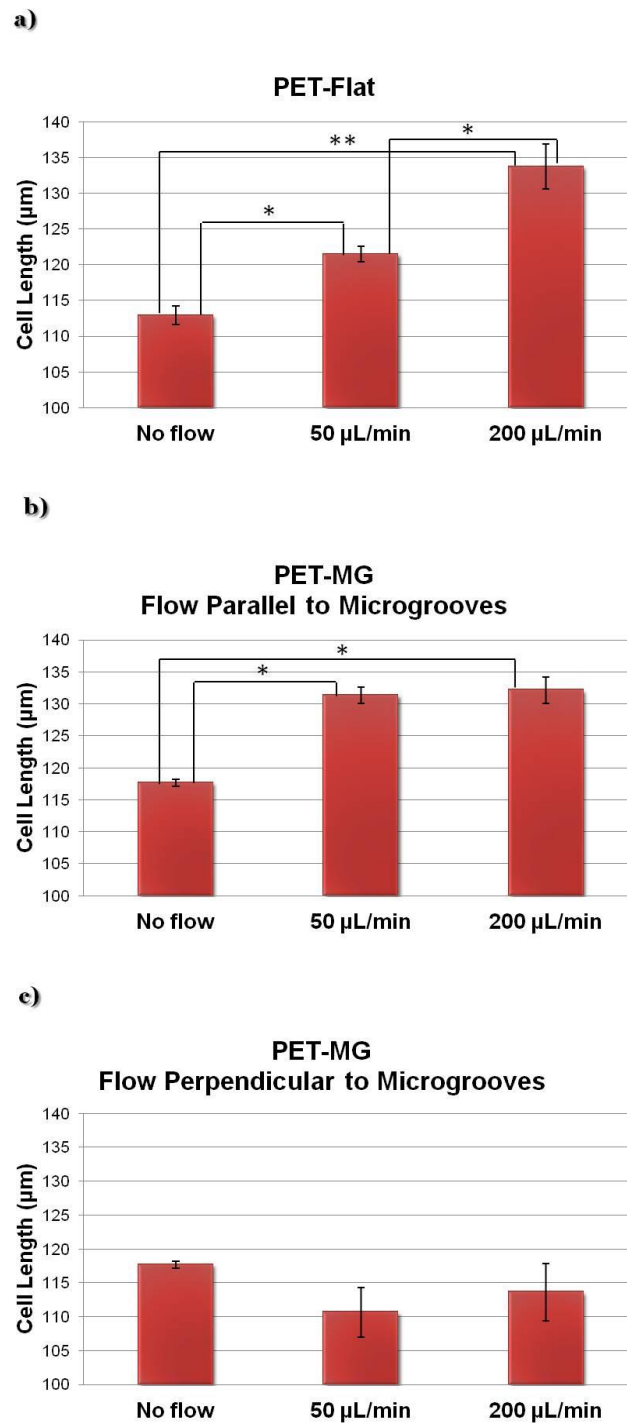
Figure 3.22: *Cell length of SW10 cells (via Fiji ImageJ and Operetta High-Content Imaging System) on the PET-Flat (a) and PET-MG (b, c) substrates under static and dynamic conditions, applying 50 and 200 µL/min, on the third day of culture. The flow was parallel (b) or perpendicular (c) to the microgrooves. The statistical analysis of the data was performed using post hoc Tukey HSD test. A p-value < 0.05 was considered significant.*

3.6 *In vitro* experiments with N2a cells

3.6.1 Growth and differentiation of N2a cells on the laser-microstructured substrates (MG) under static conditions

Figure 3.23 illustrates the morphology of N2a cells cultured on the PET-Flat (Figures 3.23a, c, e) or PET-MG substrates (Figures 3.23b, d, f), under static conditions, on the third day of culture. To perform the cell differentiation experiments (Figures 3.23a-d), the culture medium was replaced with either serum-free DMEM containing 1% antibiotic solution and 300 μM cAMP (Figures 3.23a, b) or serum-free DMEM containing 1% antibiotic solution (Figures 3.23c, d) after 24 hours of incubation.

We observed that N2a cells exhibited good attachment and outgrowth both on the PET-Flat and PET-MG substrates (Figures 3.23e, f). However, contradictory to SW10 cells, N2a cells appeared to be randomly oriented on the MG (Figures 3.23e, f). In the differentiation experiments, we noticed that N2a cells developed neurite-like extensions on the PET-Flat, both with serum deprivation and with/without the addition of cAMP (Figures 3.23a, c). However, N2a cells did not develop neurite-like extensions on the MG and appeared to have rounded cell morphology (Figures 3.23b, d).

Day 3

DMEM w/o FBS
+ 1% PS
+ 300 μM cAMP

DMEM w/o FBS
+ 1% PS

DMEM + 10% FBS
+ 1% PS
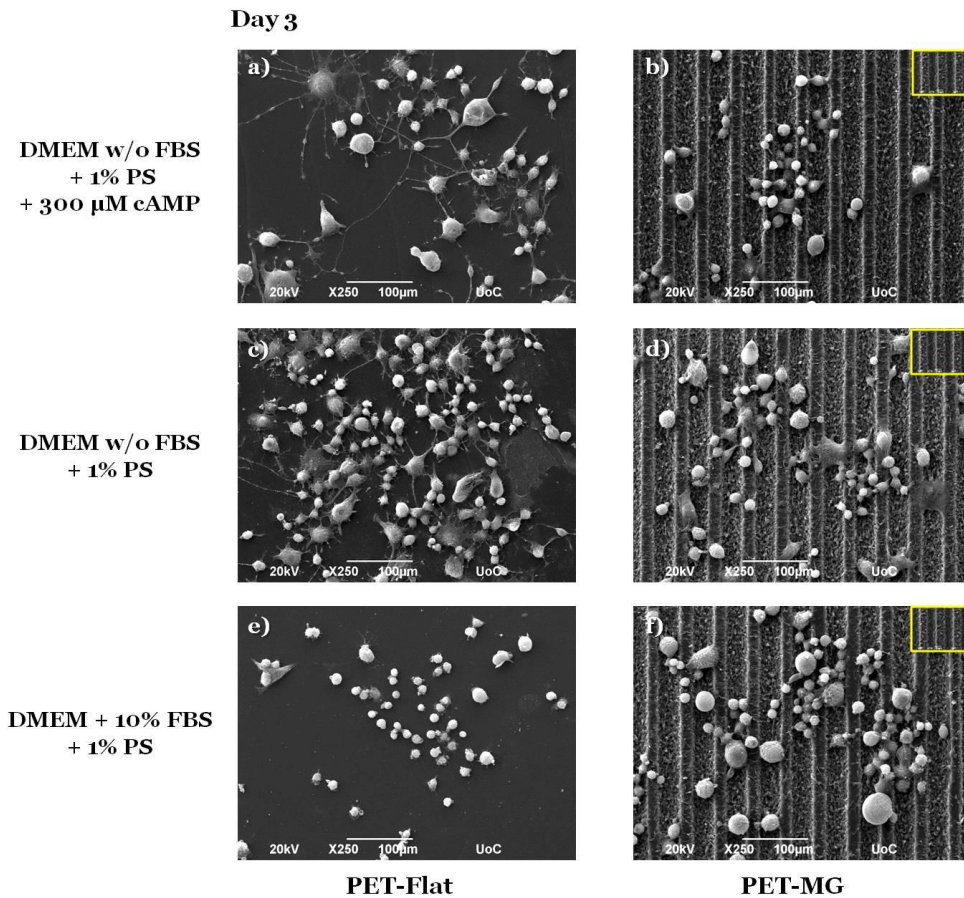
PET-Flat   **PET-MG**

Figure 3.23: *SEM images of N2a cells cultured on the PET-Flat (a, c, e) or PET-MG (b, d, f) substrates, under static conditions, on the third day of culture. For the cell differentiation experiments (a-d) the culture medium [DMEM + 10% FBS + 1% antibiotic solution Pen-Strep (PS)] was replaced with serum-free (w/o FBS) DMEM containing 1% PS + 300 μM cAMP (a, b) or serum-free (w/o FBS) DMEM containing 1% PS (c, d) after 24 hours of incubation. The inset SEM images, framed by a yellow box, depict the geometry of microgrooves.*

In agreement with the SEM images (Figure 3.23), the respective confocal images of N2a cells on the PET-Flat (Figures 3.24a, d, g) or PET-MG substrates [on top of MG (Figures 3.24b, e, h) or inside MG (Figures 3.24c, f, i)] showed that N2a cells extended neurites on the PET-Flat (Figures 3.24a, d), but they did not both on top (Figures 3.24b, e) and inside (Figures 3.24c, f) the MG of the PET-MG substrates.

77

Day 3

PET-Flat

PET-MG
(On top of MG)

PET-MG
(Inside MG)

DMEM w/o FBS
+ 1% PS
+ 300 µM cAMP

DMEM w/o FBS
+ 1% PS

DMEM + 10% FBS
+ 1% PS

Figure 3.24: Confocal images of N2a cells cultured on the PET-Flat (a, d, g) or PET-MG substrates [on top of MG (b, e, h) or inside MG (c, f, i)], under static conditions, on the third day of culture. The cytoskeleton of the cells is visualized with red color (Alexa Fluor® 680 Phalloidin) while the nuclei with blue color (DAPI). For the cell differentiation experiments (a-f) the culture medium [DMEM + 10% FBS + 1% antibiotic solution Pen-Strep (PS)] was replaced with serum-free (w/o FBS) DMEM containing 1% PS + 300 µM cAMP (a-c) or serum-free (w/o FBS) DMEM containing 1% PS (d-f) after 24 hours of incubation. The inset SEM images, framed by a yellow box, depict the geometry of microgrooves.

The extension of neurites revealed in Figures 3.23a, c and 3.24a, d, indicated the ability of N2a cells to be differentiated on the PET-Flat substrates. To verify the differentiation ability of N2a the detection of class III β-tubulin (specific neuronal marker) was studied. For the staining of this marker, the specific anti-class III β-tubulin monoclonal antibody (TUJ1) was used.

These studies (Figure 3.25) also confirmed that the PET-Flat allowed the differentiation of N2a cells to neurons promoting the neurite formation (Figures 3.25a, c), whereas the MG inhibited the differentiation of cells considering the rounded cell morphology (Figures 3.25b, d).
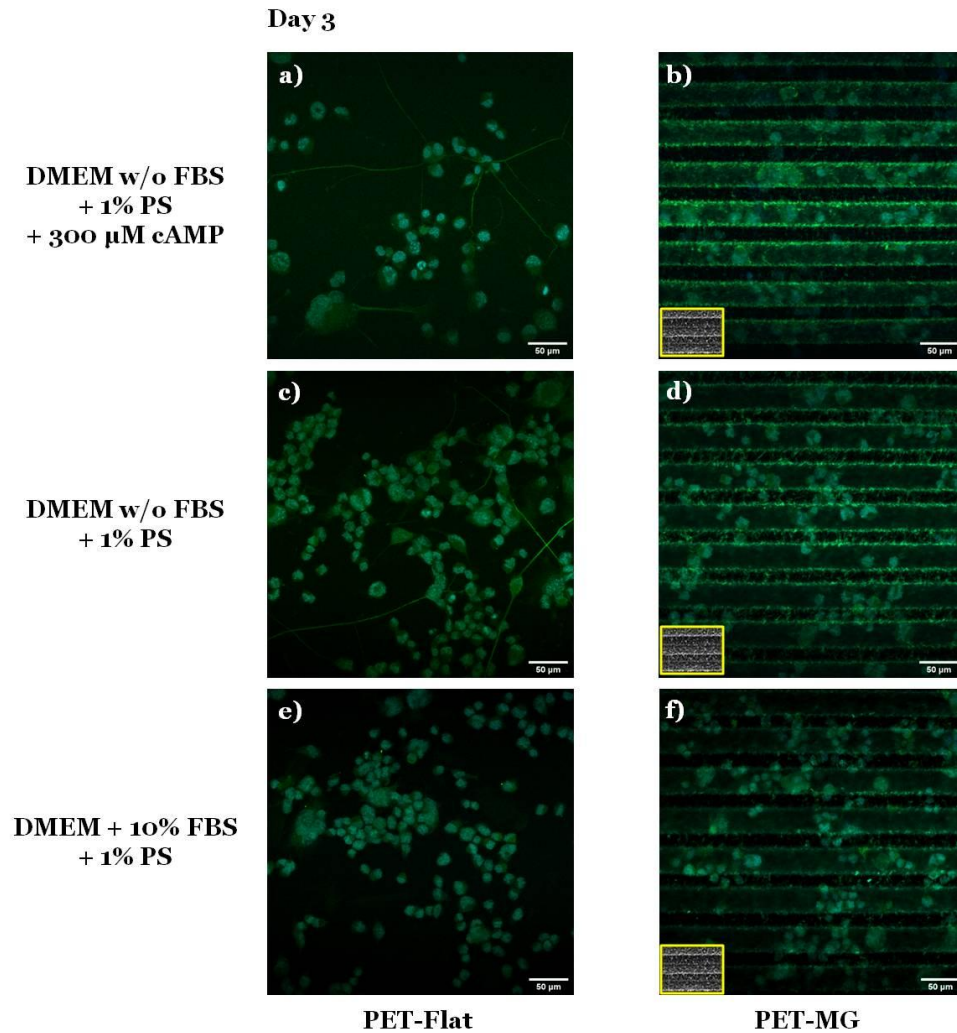
Figure 3.25: *Staining of neuron-specific class III β-tubulin in N2a cells. Confocal images of N2a cells cultured on the PET-Flat (a, c, e) or PET-MG (b, d, f) substrates, under static conditions, on the third day of culture. The cells were stained using the anti-mouse TUJ1 (green color) antibody. Nuclei were stained with DAPI (blue color). For the cell differentiation experiments (a-d) the culture medium [DMEM + 10% FBS + 1% antibiotic solution Pen-Strep (PS)] was replaced with serum-free (w/o FBS) DMEM containing 1% PS + 300 μM cAMP (a, b) or serum-free (w/o FBS) DMEM containing 1% PS (c, d) after 24 hours of incubation. The inset SEM images, framed by a yellow box, depict the geometry of microgrooves.*

3.6.2 Growth and differentiation of N2a cells on the laser-microstructured substrates (MG) under dynamic conditions

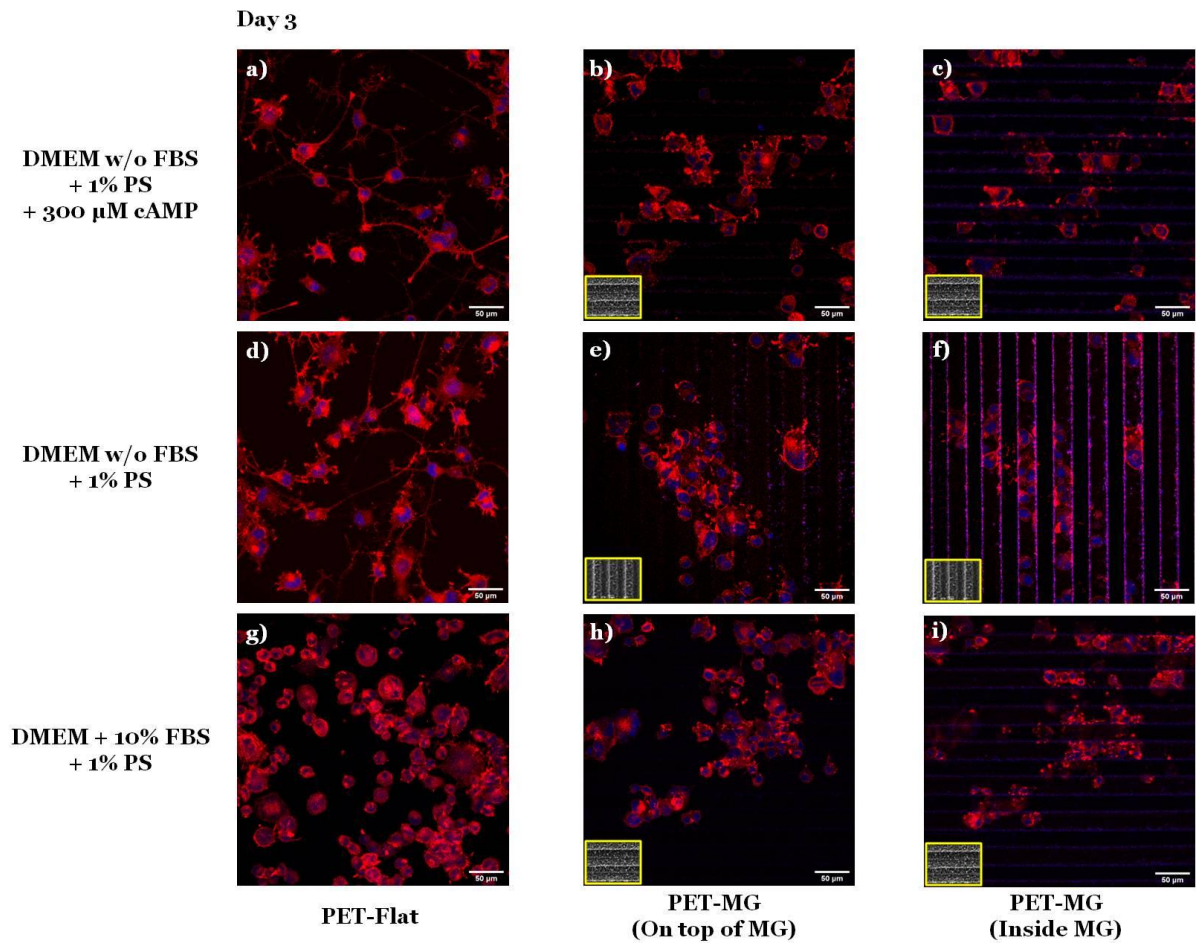Figure 3.26 presents the N2a cells cultured on the PET-Flat (Figures 3.26a, d) or PET-MG substrates [on top of MG (Figures 3.26b, e) or inside MG (Figures 3.26c, f)], under dynamic conditions, applying 15 (Figures 3.26a-c) and 30 (Figures 3.26d-f) μL/min on the third day of culture. The cell differentiation experiments were performed by replacing the culture medium with serum-free DMEM containing 1% antibiotic solution after 24 hours of incubation.

By applying both flow rates parallel to the MG length, we observed that N2a cells did not exhibit the phenotype of differentiated cells (neurite extensions) both on top (Figures 3.26b, e) and inside (Figures 3.26c, f) the MG of the PET-MG substrates, in agreement with the static cultures (Figures 3.23 and 3.24). Interestingly, under dynamic conditions, N2a cells did not appear such a phenotype either on the PET-Flat (Figures 3.26a, d), contradictory to the static cultures (Figures 3.23 and 3.24). Further investigation of the N2a differentiation process by immunofluorescence experiments using the TUJ1 antibody (Figure 3.27), revealed that flow-induced shear stress (Figures 3.27a, c) seemed to inhibit the differentiation of N2a cells to neurons.

Day 3

15 µL/min

30 µL/min

PET-Flat

PET-MG
(On top of MG)

PET-MG
(Inside MG)

Flow direction
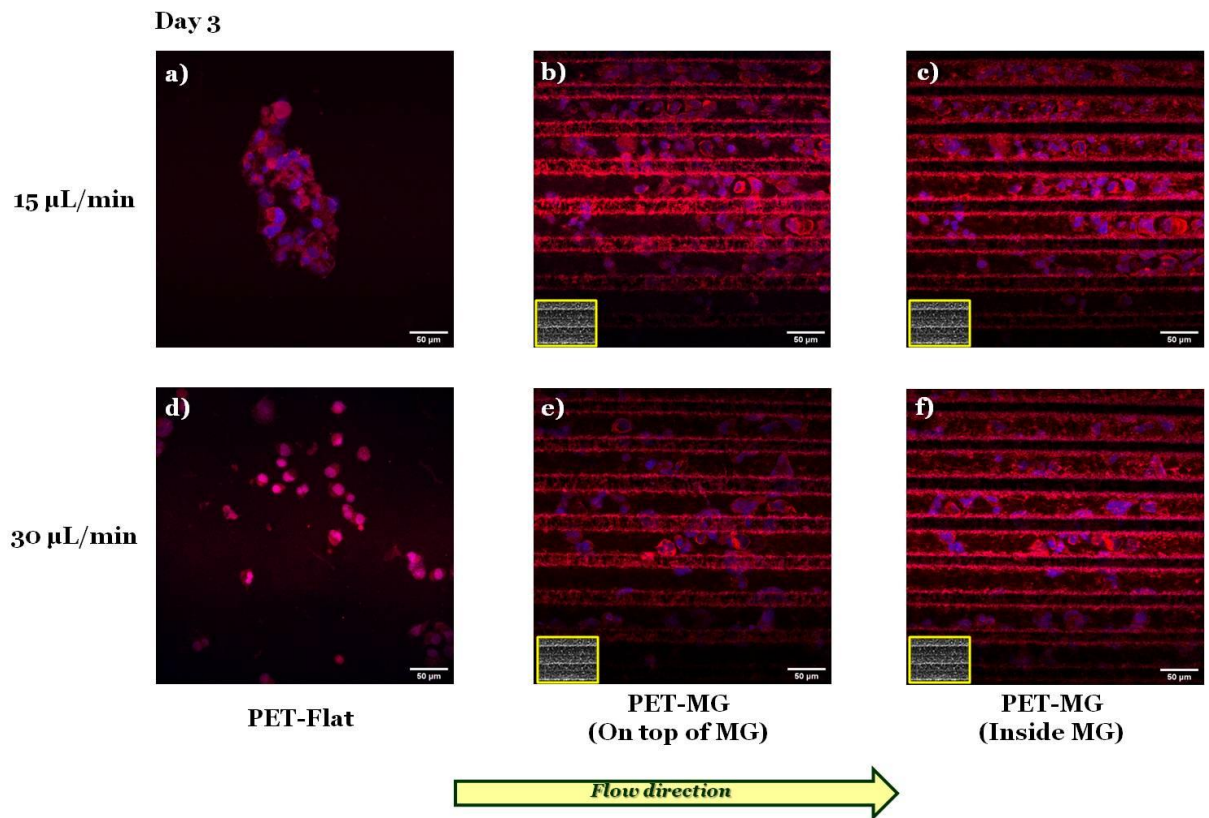
Figure 3.26: *Confocal images of N2a cells cultured on the PET-Flat (a, d) or PET-MG substrates [on top of MG (b, e) or inside MG (c, f)], under dynamic conditions, applying 15 (a-c) and 30 (d-f) µL/min, on the third day of culture. The cytoskeleton of the cells is visualized with red color (Alexa Fluor® 680 Phalloidin) while the nuclei with blue color (DAPI). The culture medium [DMEM + 10% FBS + 1% antibiotic solution Pen-Strep (PS)] was replaced with serum-free (w/o FBS) DMEM containing 1% PS, to perform the cell differentiation experiments, after 24 hours of incubation. The inset SEM images, framed by a yellow box, depict the geometry of microgrooves. The yellow arrow represents the direction of the flow.*
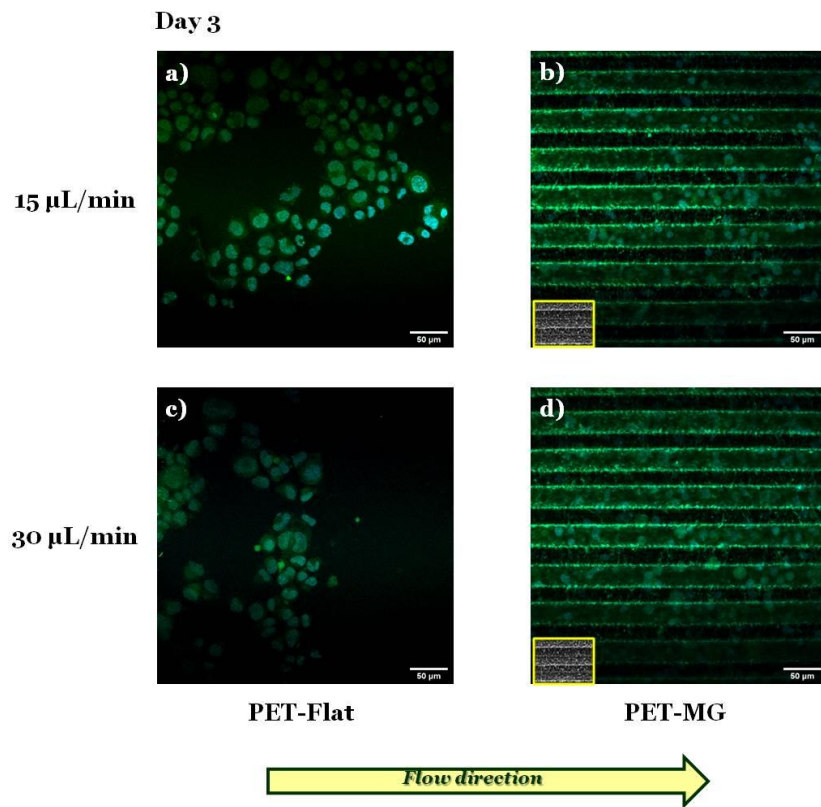
Figure 3.27: *Staining of neuron-specific class III β-tubulin in N2a cells. Confocal images of N2a cells cultured on the PET-Flat (a, c) or PET-MG (b, d) substrates, under dynamic conditions, applying 15 (a, b) and 30 (c, d) μL/min, on the third day of culture. The cells were stained using the anti-mouse TUJ1 (green color) antibody. Nuclei were stained with DAPI (blue color). The culture medium [DMEM + 10% FBS + 1% antibiotic solution Pen-Strep (PS)] was replaced with serum-free (w/o FBS) DMEM containing 1% PS, to perform the cell differentiation experiments, after 24 hours of incubation. The inset SEM images, framed by a yellow box, depict the geometry of microgrooves. The yellow arrow represents the direction of the flow.*

3.7 In vitro experiments with SW10 and N2a cells (co-culture)

3.7.1 Co-culture of SW10 and N2a cells on the laser-microstructured substrates (MG) under static conditions

Figure 3.28 depicts the co-culture of SW10 and N2a cells on the PET-Flat (Figures 3.28a, c, e) or PET-MG (Figures 3.28b, d, f) substrates, under static conditions, on the

third day of culture. For the cell differentiation experiments (Figures 3.28a-d), the culture medium was replaced with DMEM containing 0.5% FBS, 1% antibiotic solution, and 300 μM cAMP (Figures 3.28a, b) or DMEM containing 0.5% FBS and 1% antibiotic solution (Figures 3.28c, d) after 24 hours of incubation. Due to the fact that serum-free DMEM caused the death of SW10 cells, the DMEM supplemented with 0.5% FBS in the co-culture system.

The discrimination between SW10 and N2a cells was made based on their morphological characteristics. In particular, SW10 cells are flat and elongated while undifferentiated N2a cells have a more rounded shape while differentiated N2a cells develop neurite-like extensions. Additionally, the distinction between the two cell types was made through the specific TUJ1 marker applied in the co-culture system. Since N2a cells are TUJ1 positive cells, they were shown in green color in the confocal microscope (Figure 3.28).

We noticed that the SW10 cells in the co-culture system exhibited similar behavior compared to their mono-culture (as previously described in sections 3.5.1 - 3.5.3) i.e. preferential orientation along the direction of the MG and high randomness on the PET-Flat (Figure 3.28). The response of N2a cells in the co-culture system was also similar to that observed in their mono-culture (as previously described in section 3.6.1) i.e. good attachment, outgrowth, and no preferential orientation on the PET-Flat, as well as, on the MG (Figures 3.28e, f). However, we observed that when N2a cells were co-cultured with SW10 cells, on the PET-Flat, N2a cells preferred to grow on top of the SW10 cells (Figure 3.28e).

Regarding the differentiation experiments, we noticed that N2a cells, in the co-culture system, differentiated to neurons on the PET-Flat developing a neuronal network (Figures 3.28a, c), whereas they did not differentiate on the MG (Figures 3.28b, d). The results were in agreement with the respective mono-culture, as previously described in section 3.6.1. Interestingly, we observed that in the co-culture system on the PET-Flat, N2a cells tended to develop neurite extensions on top of the SW10 cells (Figures 3.28a, c).

Day 3
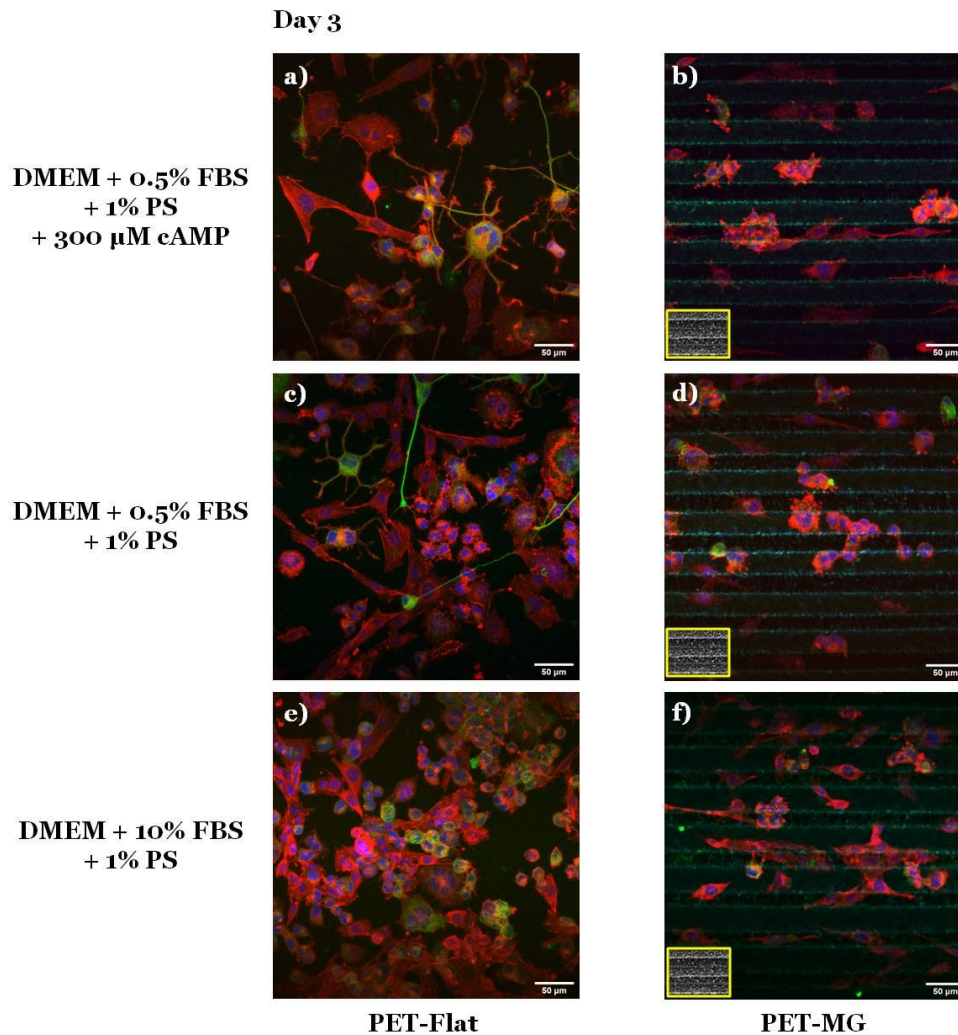
Figure 3.28: *Confocal images of the co-culture of SW10 and N2a cells on the PET-Flat (a, c, e) or PET-MG (b, d, f) substrates, under static conditions, on the third day of culture. For the staining of neuron-specific class III β-tubulin in N2a cells, cells were stained using anti-mouse TUJ1 (green color) antibody. The F-actin of cells' cytoskeleton was stained with Alexa Fluor® 568 Phalloidin (red color). Nuclei were stained with DAPI (blue color). For the cell differentiation experiments (a-d) the culture medium [DMEM + 10% FBS + 1% antibiotic solution Pen-Strep (PS)] was replaced with DMEM + 0.5% FBS + 1% PS + 300 μM cAMP (a, b) or DMEM + 0.5% FBS + 1% PS (c, d) after 24 hours of incubation. The inset SEM images, framed by a yellow box, depict the geometry of microgrooves.*

4. Discussion

Although the axons of the PNS spontaneously regenerate after injury, the regeneration that takes place is rarely functional because axons are usually directed in inappropriate targets [57,186,187]. Therefore, the discovery of successful methods to guide neurite outgrowth in a controllable manner, *in vitro*, is essential towards neurogenesis.

The survival and function of neurons strongly depend on the support of glial cells. Owing to their ability to release neurotrophic factors, express cell surface ligands, and synthesize ECM, as well as to their oriented shape and structural reorganization, glial cells provide molecular and topographical guidance stimuli for the development and outgrowth of neurons [69]. As a consequence, the evaluation of both glial cells' and neurons' responses on the culture substrate topography as well as on the surrounding mechano-environment is of significant value.

Previous studies have shown that the culture substrate topography, particularly in the form of continuous electrospun polymeric fibers and grooves, as well as discontinuous isotropic and anisotropic pillars/cones, influence neurite outgrowth, orientation, and differentiation [15,30,146–155,31,156–165,139,166,167,140–145].

Apart from topography, it has recently become increasingly evident that neurogenesis may be also driven by mechanical factors [188,189]. Indeed, it has been reported that shear stress is a significant component of the host environment of regenerating axons [69]. Consequently, fluid-induced shear stress may be also pivotal for guiding neurite outgrowth. Although Schwann cells are the main glial cells in the PNS, the effect of shear stress on this cell type has been rarely reported [69,75,76]. Specifically, Chafik et al. [69] showed that mechanical stimuli (1.33 Pa for 2 hours) enhanced the proliferation of Schwann cells and caused a slight movement from their original positions. Furthermore, Gupta et al. [75,76] reported that shear stress (3.1 Pa for 2 hours) increased the proliferation of primary Schwann cells and down-regulated myelin protein gene expression. However, the main limitation in these studies was that the flow was not continuous, as it is *in vivo*, but applied for only a few hours per day. In addition to this, the effect of shear stress on the alignment of Schwann (SW10)

cells, as well as, the cell length has not been addressed. More importantly, to the best of our knowledge, the combined effect of shear stress and topography on SW10 cells' behavior has not been reported yet. Moreover, there is currently no study in the literature focusing on the effect of shear stress combined with or without topography on neuronal (N2a) cells, although N2a cells are extensively used as a model system to study neurite outgrowth [126–132].

The present study aims to present for the first time the combined effect of shear stress and topography on the growth, orientation, and elongation of SW10 cells, as well as, on the growth and differentiation of N2a cells, under dynamic culture conditions attained via continuous microfluidic flow used to produce the applied shear stress. For this purpose, a precise flow controlled microfluidic system with custom-made chambers incorporating the laser-microstructured substrates was developed to investigate the synergistic or antagonistic effect of shear stress and topography on neural cell outgrowth, orientation, elongation, and differentiation under continuous flow conditions (Figure 2.2). The cell culture results were combined with computational flow simulation studies employed to calculate accurately the shear stress values. Finally, the effect of topography on the co-culture of SW10 and N2a cells was studied to better simulate the PNS via the involvement of both glial and neuronal cells.

It is worth mentioning that prior to the use of SW10 cells and N2a cells in static and dynamic cell cultures, NIH 3T3 cells were used as a well-characterized experimental model for studying cellular functions (adhesion, proliferation, orientation) in order to optimize basic parameters of the experiment (e.g. cell densities, days of culture, flow rates).

In this work, polymeric (PET) anisotropic continuous MG (PET-MG substrates), isotropic discontinuous chess (PET-Chess substrates), and isotropic continuous net (PET-Net substrates) have been fabricated via ultrafast laser structuring (Figure 3.1), which is a simple and effective method to fabricate micro- and nano-structures with controlled geometry and pattern regularity [42,43]. It is known that the groove width, in continuous grooved substrates, plays a critical role in the neuronal outgrowth [149,150,159–161,151–158]. Considering that patterns exhibiting widths or spacings

in the range from 2 to 30 μm are optimal for the Schwann cells' alignment [24], the width/spacing of the anisotropic continuous MG was chosen to be within this range, i.e. ~29 μm. A similar spacing, ~25 μm, was used in the isotropic discontinuous chess, while a larger spacing, ~168 μm, in the isotropic continuous net.

The aforementioned patterns were employed to imitate native nerve regeneration support structures, particularly imitating the guidance/alignment and growth of Schwann cells. It is known that primary Schwann cells transiently proliferate and form longitudinal bands of Büngner (boB) [190]. Aligned Schwann cells and their extracellular matrix are indispensable pathways for oriented axonal regrowth. From a molecular point of view, the boB formation is unknown. A possible mechanism may be the polarized expression of adhesion proteins along the proximal-distal cell axis [190]. It has been reported that placement of dissimilar adhesion characteristics in separate Schwann cell surface domains could aid longitudinal cell alignment. From a physical point of view, the basal lamina tube (enwrapping Schwann cells and myelinated axons) is the guiding cue for axonal regrowth [190].

The laser-microstructured substrates (PET-MG, PET-Chess, PET-Net) have been characterized as to wetting properties (contact angle measurements), and surface chemistry (UV-Vis, LIF, Raman measurements). Specifically, a decrease in the hydrophilicity was observed on the PET-MG, PET-Chess, and PET-Net compared to the PET-Flat, which is associated with the increased roughness of the surfaces after irradiation with the femtosecond laser [191] (Figure 3.3). UV-Vis spectra revealed an increase of the absorption in the laser-microstructured substrates due to the structuring process (Figure 3.4) Additionally, the spectra showed the development of an absorption band in the region of 300 - 500 nm in the PET-MG and PET-Chess, except PET-Net probably due to the large net's spacing, which is attributed to the presence of aromatic hydroxylated species produced during the photooxidation of PET (Figure 3.4). This finding was in agreement with previous studies, demonstrating the development of an absorption band at around 340 nm in the UV range [192–194]. The data obtained by the fluorescence spectroscopy are related to the production of fluorescent species generating from reactions dependent on the UV irradiation and oxygen [193]. In particular, excitation at 248 nm on the PET-Flat revealed a peak

centered at ~460 nm, which is associated with the fluorescence of mono-hydroxylated species which are known to be generated during the photodegradative process of PET [193] (Figure 3.5). The blue shift and the fluorescent increase of the PET-MG, PET-Chess, and PET-Net compared to the PET-Flat may be ascribed to additional modifications to the surface chemistry of the irradiated samples (e.g. the formation of additional fluorescent species) due to the structuring process (Figure 3.5). Finally, Raman spectra displayed an increase of the fluorescence background in the PET-MG, PET-Chess, and PET-Net compared to the PET-Flat, indicating that additional modifications are induced on the irradiated sample surface, besides the topological one [185] (Figure 3.6).

Considering the high viability of NIH 3T3 cells on the PET-Flat and the laser-microstructured substrates (PET-MG, PET-Chess, PET-Net) (Figure 3.8), as well as, the good attachment and outgrowth of NIH 3T3 cells (Figure 3.9), SW10 cells (Figures 3.13 and 3.16), and N2a cells (Figure 3.23) on the substrates, we can conclude that the observed surface roughness and photooxidation on the irradiated samples surfaces seem to have a minor effect on cells' response.

Among the different geometries, we observed that NIH 3T3 cells were oriented along the direction of the MG, while they showed an omnidirectional orientation on the PET-Chess, and PET-Net, as well as, on the flat PET (Figures 3.9 and 3.10). In agreement with NIH 3T3 cells, SW10 cells exhibited similar behavior i.e. preferential orientation along the MG length and high randomness on the other geometries and the flat PET (Figures 3.13 and 3.15). This was also demonstrated by the directionality histograms presented in Figure 3.14.

The preferential alignment of cells along the anisotropic continuous MG may be attributed to the effect of anisotropy, providing cues along a single axis, and to the optimal width/spacing of the MG (in our case ~29 μm). Considering the similar size (chess pieces' diameter ~ 22 μm) and spacing (~25 μm) of the chess with that of MG, the random orientation of cells, on the isotropic discontinuous chess, could be ascribed to the isotropic surface providing cues along multiple axes. The effect of isotropic discontinuous geometries on the alignment of glial cells has not been reported. Studies have been performed on nerve cells showing that the features'

diameter and spacing are critical parameters for oriented neurite outgrowth [195–197]. In particular, it has been reported that as the feature diameter and spacing increased, above ~10 μm, a transition from a preferential to a random orientation occurred on the isotropic discontinuous geometries [195–197]. Finally, the high randomness of cells on the isotropic continuous net could be attributed to the large net's spacing, ~168 μm, resulting in similar cell behavior to that found on a flat substrate.

Based on these results, the MG provided a favorable environment for the alignment of SW10 cells, which is crucial for axonal regeneration by providing physical guidance as well as neurotrophic and neurotropic support for axonal regrowth [69]. Thus, the geometry of MG was selected to be the most appropriate for investigating the combined effect of shear stress and topography on neuronal response.

Since the forces of values applied during nerve regeneration *in vivo* have not been described, prior to using SW10 cells and N2a cells, parametric studies were performed with NIH 3T3 cells (Figures 3.11 and 3.12) to conclude to the flow rates used in this study (Tables 2.2 and 2.3).

By applying a flow rate of 30 μL/min, we noticed that SW10 cells oriented parallel to the MG length and the flow, while high randomness was observed on the flat PET substrates (Figure 3.17). Therefore, the flow rate was increased (50 and 200 μL/min) to examine whether the cells would be oriented on the flat PET. Interestingly, under both flow rates of 50 and 200 μL/min, we noticed that the SW10 cells' cytoskeleton oriented parallel to flow, whereas it showed a random orientation under static conditions on the PET-Flat substrates (Figures 3.18a-c and 3.20a). Moreover, the length of SW10 cells under the flow rates of 50 and 200 μL/min on the PET-Flat significantly increased by 7.6% and 18.5%, respectively, compared to the static culture conditions (Figure 3.22a). To date, the values of shear stress reported to be stimulatory for Schwann cells for short periods are higher than 1 Pa [69,75,76]. In this study, although the values of shear stress exerted to the cells were lower, 0.04 and 0.15 Pa, it is found that they were adequate to promote the cells' alignment and elongation. Both phenomena could be attributed to the continuous fluid-induced shear

stress experienced by the cells, which induces mechanical stimulation resulting in the reorganization of the cytoskeleton [57,69,70].

In a novel approach, the combined effect of shear stress and topography on SW10 cells' behavior has been studied. Our results presented in Figures 3.18d-f, 3.19a-c, 3.20b, 3.21a, and 3.22b clearly show that this effect is synergetic when the flow direction is parallel to the MG length and gives rise to further enhancement of cells' orientation and elongation. Indeed, a significantly increased cell length by 11.7% and 12.3% was observed upon applying the flow parallel to the MG length, compared to the static culture conditions on the PET-MG substrates. However, the shear stress cannot provide further significant enhancement of SW10 cells' length and orientation above 50 μL/min on the MG. This indicates that small values of flow rate are sufficient to attain the maximum cell response.

When the flow was perpendicular to the MG length direction, we noticed that SW10 cells retained their orientation along the direction of the MG, despite the presence of shear stress in the perpendicular direction (Figures 3.18h-i, 3.19e-f, 3.20c, 3.21b). Furthermore, the cell length, in that case, was lower compared to the static cultures on the same substrates (Figure 3.22c). Both results imply that an antagonistic effect between the shear stress and topography takes place in this case and the topography effect on cell response is more pronounced.

Despite the different shear stress values inside and on top of the MG of the PET-MG substrates, obtained from numerical simulations, similar results on the SW10 cells' cytoskeleton orientation were observed both inside and on top of the MG of the PET-MG substrates (Figures 3.20b, c and 3.21 respectively). This indicates that the topography is the dominant factor that drives the cell orientation, compared to the shear stress (at least within the range of shear stress values used in this study).

Results obtained from numerical simulations of the flow in the cell culture chamber for the PET-Flat and PET-MG substrates (Figure 3.7) indicated that on the PET-Flat shear forces are non-uniformly distributed with stronger spatial gradients located near the boundaries of the flow domain. When the substrate topography is altered by placing MG, in either parallel or perpendicular to the mean flow direction, wall shear

stress distribution patterns are strongly affected with marked spatial gradients appearing at the edges of the MG profile. As the cell size is of the scale of the MG pattern it is expected that cells lying to the top of the MG will be exposed to both a high axial shear and a strong axial shear gradient in a direction perpendicular to the flow. Therefore the response of these cells regarding cytoskeleton length and orientation will be the result of a triplet of factors, i.e. a) substrate topography, b) shear stress and c) spatial gradient of shear stress. These factors appear to act in a synergistic way when MG are parallel to the mean flow direction, while the topography seems to be superior in the case where MG are placed perpendicular to the mean flow. The presence of spatial gradients of wall shear stress in the microfluidic system chamber and the effects of these gradients on cell response is of interest.

Experimental observations in cultured endothelial cells have indicated that cell morphology and phenotype response are sensitive to spatial gradients of wall shear stress [198,199]. Endothelial cells tend to align with the flow under uniform wall shear stress but appear more randomly oriented when exposed to shear stress gradients. Based on these observations it could be ascertained that shear gradients would be expected to act in a way to reduce the heights of bars in Figures 3.22b, c. However, as cell response shown in Figure 3.22 accounts for topography, magnitude, and gradients of wall shear stress, it is not possible to separate the effect of gradients. It should also be noted that as gradients of shear increase with flow rate their relative effect will be more pronounced in the 200 µL/min case. This may explain why cell length appears similar for 50 and 200 µL/min in the microstructured substrate case presented in Figure 3.22b in contrast to the marked length difference observed in the flat substrate case presented in Figure 3.22a.

It should be noted that the computational geometry of the PET-MG substrate is an idealized version of the real microstructured groove geometry depicted in Figures 3.1a and 3.2. Therefore although the pattern in the wall shear stress gradients will be similar minor quantitative differences in the experimental conditions are expected. This, however, is not expected to alter our main findings.

Although the effect of anisotropic continuous topographies on Schwann cells has been studied, there are limited studies on N2a cells [133,137,158,200]. Specifically, Mitra et. al. [137] reported that N2a cells oriented on and along with the carbon micro-track length for micro-track width and inter-track distances of 15 - 30 μm, which was comparable to the cell dimension (~15 μm). Additionally, differentiated N2a cells extended neurites aligned along the micro-track axis when the track width was 15 μm. Similarly, Beduer et. al. [158] showed that PDMS grooves of 20 μm width promoted the differentiation rate of N2a cells and the neurite alignment along the groove axis. On the contrary, Zhu et. al. [133] demonstrated that the neurites of differentiated N2a cells guided by Si, polyamide (PI), and transparency grooves of 300 - 400 nm width, 400 - 700 nm depth, and 1 - 1.2 μm period. Finally, Lee et. al. [200] reported that N2a cells on silicon dioxide (SiO_2) linear ridges with 4 μm height, extended neurites following the linear microtrack. Consequently, a wide range of dimensions affecting neurite outgrowth has been proposed in the literature.

Generally, it has been shown that, on the microscale (a scale similar to that of axons), the effect of distance between topographical features on the neurons' alignment increases as the width of the space between the cues decreases [201]. On the nanoscale, the sensitivity of neurons in the nanometer-sized topographical cues is strongly evident [201]. Since the cell adhesion sites, i.e. focal adhesions, are in the range of 5 - 200 nm [202], it was proposed that the cell-substrate interactions are governed by intricate mechanisms operating at the nanoscale. In particular, it was suggested that the cell-substrate interactions are strongly influenced by nanoscale rather than microscale features [203,204]. On the nanoscale, there is also sensitivity producing different effects on cell differentiation [201]. Indeed, previous studies demonstrated that several neuronal markers [e.g. microtubule-associated protein 2 (MAP2), TUJ1] were significantly upregulated on nano-grating substrates compared to unpatterned and micro-grating substrates [205,206]. The aforementioned observations, regarding the importance of size scale, may explain in our study the omnidirectional orientation of N2a cells on the MG, as well as, the inhibition of cell differentiation on them (width/spacing of MG ~ 29 μm) (Figures 3.23, 3.24, 3.25).

In accordance with the static cultures, by applying the flow rates of 15 and 30 μL/min parallel to the MG length, we observed that N2a cells remained undifferentiated on the MG (Figures 3.26 and 3.27). Interestingly, under dynamic culture conditions (both flow rates of 15 and 30 μL/min), N2a cells did not differentiate on the PET-Flat (Figures 3.26 and 3.27) in contrast to the static cultures (Figures 3.23, 3.24, 3.25). This implies that shear stress may inhibit the differentiation of N2a cells (at least within the range of values used in this study). However, further investigation is needed to identify the exact mechanisms resulting in the inhibition of cell differentiation due to shear stress.

Finally, the co-culture of SW10 and N2a cells was investigated on the PET-Flat and PET-MG substrates, inspired by the indirect alignment of neuronal cells by targeting the influence of the patterned topography towards glial cells [4]. Although topographical cues are used to directly influence the neuronal outgrowth, an alternative strategy is to use a patterned topography to align glial cells. Glial cells, in turn, can support and stimulate the directed axonal growth not only through physical guidance cues but also through aligned pathways of biochemical guidance cues, like secreted ECM molecules [207]. Schwann cells aligned on patterned substrates have been shown to promote neuronal outgrowth and direct axonal growth [156,167,208].

Specifically, studies of Schwann cells co-cultured with dorsal root ganglion (DRG) neurons have been reported [156,208]. Miller et. al. [156] co-cultured Schwann cells with DRG on poly(D,L-lactic acid) (PDLA) microgrooves and found that the presence of Schwann cells in the grooves promoted the neurite alignment and outgrowth. Additionally, Schwann cells helped the neurites to orient on shallower grooves and exhibit continued alignment even as the grooves degraded. Pawelec et. al. [208] showed that the co-culture of Schwann cells with DRG neurons on porous PCL increased the neurite outgrowth and led to a higher percentage of cells with neurites in comparison to DRG neurons mono-culture. As far as we are concerned, there is only one study of the co-culture of Schwann cells with N2a cells [167]. Angelaki et. al. [167] demonstrated that the presence of Schwann cells altered the adhesion behavior of N2a cells in their co-culture. In particular, N2a cells followed

the adhesion of the oriented Schwann cells and adhered only to the sites where the Schwann cells were located i.e. microcones.

However, in our study, when SW10 cells were co-cultured with N2a cells on the MG a similar behavior was observed compared to their mono-cultures i.e. preferential orientation of SW10 cells along the direction of the MG, as well as, random orientation of N2a cells on the MG and inhibition of differentiation on them (Figures 3.28b, d, f).

Interestingly, on the PET-Flat, in the co-culture system, N2a cells preferred to grow on top of the SW10 cells (Figure 3.28e), while differentiated N2a cells developed neurite extensions on top of the SW10 cells (Figures 3.28a, c). Based on these observations, it can be assumed that SW10 cells formed a "glial carpet", on the PET-Flat, and N2a cells preferentially grew on top of it, in agreement with [167]. This may be explained by the well-known fact that glial cells provide trophic support to the neurons [209], and as a consequence, the neuronal-like cells prefer to adhere and differentiate in the same areas with the glial cells [167,210].

Considering these promising results on the PET-Flat, we assume that with further optimization of the parameters of this preliminary experiment (e.g. cell densities, days of culture) an aligned "glial carpet" will be formed on the MG, which would serve as a substrate for directed axonal growth.

Such a co-culture patterned system is of great interest, as a) it simulates more realistically the actual structure of the PNS, including both the glial and the neuronal-like cells, b) it could be used for the assessment in dynamic microenvironments that provide a more *in vivo*-like environment.

5. Conclusions

In the present thesis, an interdisciplinary approach was realized, where laser engineering, dynamic cell culture under flow, and computational flow simulations were employed to evaluate the synergistic or antagonistic effect of shear stress and topography on neuronal response.

Ultrafast laser structuring has been employed for the fabrication of different types of polymeric (PET) microstructured substrates (MG, chess, net), characterized as to surface morphology, wetting properties, and surface chemistry. Subsequently, the NIH 3T3 cells and SW10 cells' response cultured on such substrates was evaluated to select the geometry of MG as the most appropriate topography for investigating the effect of flow-induced shear stress.

The combined effect of shear stress and MG topography on SW10 cells' growth, orientation, and elongation has been investigated under both static and dynamic culture conditions. The experimental findings were analyzed together with numerical simulations of the distribution of flow-induced wall shear stress, which was strongly affected by the substrate topography. It was revealed that, depending on the relation of the direction of flow with respect to the topographical features, wall shear stress gradients were acting in a synergistic or antagonistic manner to topography in promoting cell elongation and affecting cell response. Our results demonstrate the ability to guide the outgrowth of Schwann cells *in vitro* that could be potentially useful in the fields of neural tissue engineering with the ultimate goal of the creation of autologous graft substitutes for nerve tissue regeneration.

The combined effect of shear stress and topography on N2a cells' growth and differentiation was also evaluated. In agreement with the static cultures, it was found that, under dynamic culture conditions, N2a cells did not differentiate on the MG. However and most important, N2a cells remained undifferentiated on the flat PET substrates under dynamic culture conditions, contrary to the static cultures, indicating that shear stress may inhibit the differentiation of N2a cells. The dynamic microenvironment system presented here could also potentially be used as a new model system to explore the role of shear stress on cell differentiation.

Finally, the effect of topography on the co-culture of SW10 and N2a cells was evaluated in an attempt to differentiate and indirectly align the N2a cells through the alignment of SW10 cells on the MG. The main finding of this preliminary study was that N2a cells preferred to adhere and differentiate on top of the SW10 cells on the flat PET substrates. Taking into consideration this result, we assume that with further optimization of the parameters of the co-culture patterned system an aligned "glial carpet" will be formed on the MG which would serve as a substrate for directed axonal growth. Such a co-culture patterned system could be potentially useful in the fields of neural tissue engineering and for dynamic microenvironment systems reflecting more closely the *in vivo* conditions.

In overall, in this thesis, we studied the combined effect of stress and topography on neural cells. We demonstrated that shear stress can act synergistically or antagonistically with topographical cues in specific cell responses such as orientation and elongation.

6. Publications

- E. Babaliari, P. Kavatzikidou, D. Angelaki, L. Chaniotaki, A. Manousaki, A. Siakouli-Galanopoulou, A. Ranella, E. Stratakis, Engineering Cell Adhesion and Orientation via Ultrafast Laser Fabricated Microstructured Substrates, Int. J. Mol. Sci. 19 (2018) 2053. doi:10.3390/ijms19072053

- E. Babaliari, P. Kavatzikidou, A. Mitraki, Y. Papaharilaou, A. Ranella, E. Stratakis, Combined Effect of Shear Stress and Laser-Patterned Topography on Schwann cell Outgrowth: Synergistic or Antagonistic?, *submitted*

7. References

[1]   S.S. Pedrosa, A.R. Caseiro, J.D. Santos, A.C. Maurício, Scaffolds for Peripheral Nerve
        Regeneration, the Importance of In Vitro and In Vivo Studies for the Development of Cell-
        Based Therapies and Biomaterials: State of the Art, in: Scaffolds Tissue Eng. - Mater. Technol.
        Clin. Appl., 2017. doi:10.5772/intechopen.69540.

[2]   L. Papadimitriou, P. Manganas, A. Ranella, E. Stratakis, Biofabrication for neural tissue
        engineering applications, Mater. Today Bio. 6 (2020) 100043.
        doi:10.1016/j.mtbio.2020.100043.

[3]   J. FitzGerald, J. Fawcett, Repair in the central nervous system, J. Bone Jt. Surg. - Ser. B. 89
        (2007) 1413–1420. doi:10.1302/0301-620X.89B11.19651.

[4]   B.D. Ratner, A.S. Hoffman, F.J. Schoen, J.E. Lemons, Biomaterials science: an introduction to
        materials in medicine, 2004. https://books.google.gr/books?id=8hBq-
        dLLaxwC&pg=PA1291&lpg=PA1291&dq=CHAPTER+II.6.14+NEURONAL+TISSUE+EN
        GINEERING&source=bl&ots=Yi8s797CCk&sig=ACfU3U3cZfXzSHcvq4yJhMyTjBkDbfh1
        OQ&hl=el&sa=X&ved=2ahUKEwj_8P-
        Wp_foAhVNCewKHRO9C2MQ6AEwAXoECAsQAQ#v=onepage&q=CH (accessed April
        20, 2020).

[5]   E. GUTMANN, L. GUTTMANN, P.B. MEDAWAR, J.Z. YOUNG, The Rate of Regeneration
        of Nerve, J. Exp. Biol. 19 (1942).

[6]   Principles of Tissue Engineering, Elsevier, 2014. doi:10.1016/C2011-0-07193-4.

[7]   S.K. Seidlits, J.Y. Lee, C.E. Schmidt, Nanostructured scaffolds for neural applications,
        Nanomedicine. 3 (2008) 183–199. doi:10.2217/17435889.3.2.183.

[8]   M.J. Dalby, N. Gadegaard, M.O. Riehle, C.D.W. Wilkinson, A.S.G. Curtis, Investigating
        filopodia sensing using arrays of defined nano-pits down to 35 nm diameter in size, Int. J.
        Biochem. Cell Biol. 36 (2004) 2005–2015. doi:10.1016/j.biocel.2004.03.001.

[9]   R.G. Flemming, C.J. Murphy, G.A. Abrams, S.L. Goodman, P.F. Nealey, Effects of synthetic
        micro- and nano-structured surfaces on cell behavior, Biomaterials. 20 (1999) 573–588.
        doi:10.1016/S0142-9612(98)00209-9.

[10]   G.A. Abrams, S.L. Goodman, P.F. Nealey, M. Franco, C.J. Murphy, Nanoscale topography of
        the basement membrane underlying the corneal epithelium of the rhesus macaque, Cell Tissue
        Res. 299 (2000) 39–46. doi:10.1007/s004419900074.

[11]   A.M. Pasapera, I.C. Schneider, E. Rericha, D.D. Schlaepfer, C.M. Waterman, Myosin II activity regulates vinculin recruitment to focal adhesions through FAK-mediated paxillin phosphorylation., J. Cell Biol. 188 (2010) 877–90. doi:10.1083/jcb.200906012.

[12]   S.W. Crowder, V. Leonardo, T. Whittaker, P. Papathanasiou, M.M. Stevens, Material Cues as Potent Regulators of Epigenetics and Stem Cell Function, Cell Stem Cell. 18 (2016) 39–52. doi:10.1016/J.STEM.2015.12.012.

[13]   M.J. Dalby, N. Gadegaard, R.O.C. Oreffo, Harnessing nanotopography and integrin–matrix interactions to influence stem cell fate, Nat. Mater. 13 (2014) 558–569. doi:10.1038/nmat3980.

[14]   J.M. Stukel, R.K. Willits, Mechanotransduction of Neural Cells Through Cell–Substrate Interactions, Tissue Eng. Part B Rev. 22 (2016) 173–182. doi:10.1089/ten.teb.2015.0380.

[15]   C. Yiannakou, C. Simitzi, A. Manousaki, C. Fotakis, A. Ranella, E. Stratakis, Cell patterning via laser micro/nano structured silicon surfaces, Biofabrication. 9 (2017) 025024. doi:10.1088/1758-5090/aa71c6.

[16]   X. Wang, C.A. Ohlin, Q. Lu, J. Hu, Cell directional migration and oriented division on three-dimensional laser-induced periodic surface structures on polystyrene, Biomaterials. 29 (2008) 2049–2059. doi:10.1016/j.biomaterials.2007.12.047.

[17]   E. Rebollar, I. Frischauf, M. Olbrich, T. Peterbauer, S. Hering, J. Preiner, P. Hinterdorfer, C. Romanin, J. Heitz, Proliferation of aligned mammalian cells on laser-nanostructured polystyrene, Biomaterials. 29 (2008) 1796–1806. doi:10.1016/J.BIOMATERIALS.2007.12.039.

[18]   A. Ranella, M. Barberoglou, S. Bakogianni, C. Fotakis, E. Stratakis, Tuning cell adhesion by controlling the roughness and wettability of 3D micro/nano silicon structures, Acta Biomater. 6 (2010) 2711–2720. doi:10.1016/J.ACTBIO.2010.01.016.

[19]   N. Orgovan, B. Peter, S. Bősze, J.J. Ramsden, B. Szabó, R. Horvath, Dependence of cancer cell adhesion kinetics on integrin ligand surface density measured by a high-throughput label-free resonant waveguide grating biosensor, Sci. Rep. 4 (2015) 4034. doi:10.1038/srep04034.

[20]   E. Makarona, B. Peter, I. Szekacs, C. Tsamis, R. Horvath, ZnO Nanostructure Templates as a Cost-Efficient Mass-Producible Route for the Development of Cellular Networks, Materials (Basel). 9 (2016) 256. doi:10.3390/ma9040256.

[21]   P. Rakic, Neuron-glia relationship during granule cell migration in developing cerebellar cortex. A Golgi and electonmicroscopic study in Macacus rhesus, J. Comp. Neurol. 141 (1971) 283–312. doi:10.1002/cne.901410303.

[22]   C.D.W. Wilkinson, M. Riehle, M. Wood, J. Gallagher, A.S.G. Curtis, The use of materials patterned on a nano- and micro-metric scale in cellular engineering, Mater. Sci. Eng. C. 19 (2002) 263–269. doi:10.1016/S0928-4931(01)00396-4.

[23]   C. Simitzi, K. Karali, A. Ranella, E. Stratakis, Controlling the Outgrowth and Functions of Neural Stem Cells: The Effect of Surface Topography, ChemPhysChem. (2018). doi:10.1002/cphc.201701175.

[24]   C. Simitzi, A. Ranella, E. Stratakis, Controlling the morphology and outgrowth of nerve and neuroglial cells: The effect of surface topography, Acta Biomater. 51 (2017) 21–52. doi:10.1016/J.ACTBIO.2017.01.023.

[25]   A.A. Abdeen, J. Lee, K.A. Kilian, Capturing extracellular matrix properties in vitro: Microengineering materials to decipher cell and tissue level processes, Exp. Biol. Med. 241 (2016) 930–938. doi:10.1177/1535370216644532.

[26]   W. Chen, Y. Shao, X. Li, G. Zhao, J. Fu, Nanotopographical surfaces for stem cell fate control: Engineering mechanobiology from the bottom, Nano Today. 9 (2014) 759–784. doi:10.1016/J.NANTOD.2014.12.002.

[27]   L.G. Griffith, M.A. Swartz, Capturing complex 3D tissue physiology in vitro, Nat. Rev. Mol. Cell Biol. 7 (2006) 211–224. doi:10.1038/nrm1858.

[28]   H. Mirzadeh, M. Dadsetan, Influence of laser surface modifying of polyethylene terephthalate on fibroblast cell adhesion, Radiat. Phys. Chem. 67 (2003) 381–385. doi:10.1016/S0969-806X(03)00071-9.

[29]   M. Dadsetan, H. Mirzadeh, N. Sharifi-Sanjani, P. Salehian, IR LASER SURFACE MODIFICATION OF POLYETHYLENE TEREPHTHALATE AS BIOMATERIAL, in: Process. Fabr. Adv. Mater. VIII, WORLD SCIENTIFIC, 2001: pp. 221–229. doi:10.1142/9789812811431_0026.

[30]   C. Simitzi, P. Efstathopoulos, A. Kourgiantaki, A. Ranella, I. Charalampopoulos, C. Fotakis, I. Athanassakis, E. Stratakis, A. Gravanis, Laser fabricated discontinuous anisotropic microconical substrates as a new model scaffold to control the directionality of neuronal network outgrowth, Biomaterials. 67 (2015) 115–128. doi:10.1016/j.biomaterials.2015.07.008.

[31]   C. Simitzi, E. Stratakis, C. Fotakis, I. Athanassakis, A. Ranella, Microconical silicon structures influence NGF-induced PC12 cell morphology, J. Tissue Eng. Regen. Med. 9 (2015) 424–434. doi:10.1002/term.1853.

[32]   A.S. Alnaser, S.A. Khan, R.A. Ganeev, E. Stratakis, Recent Advances in Femtosecond Laser-

Induced Surface Structuring for Oil–Water Separation, Appl. Sci. 9 (2019) 1554. doi:10.3390/app9081554.

[33]   B.C. Stuart, M.D. Feit, A.M. Rubenchik, B.W. Shore, M.D. Perry, Laser-induced damage in dielectrics with nanosecond to subpicosecond pulses, Phys. Rev. Lett. 74 (1995) 2248–2251. doi:10.1103/PhysRevLett.74.2248.

[34]   S. Nolte, C. Momma, H. Jacobs, A. Tünnermann, B.N. Chichkov, B. Wellegehausen, H. Welling, Ablation of metals by ultrashort laser pulses, J. Opt. Soc. Am. B. 14 (1997) 2716. doi:10.1364/josab.14.002716.

[35]   T. Lippert, Interaction of Photons with Polymers: From Surface Modification to Ablation, Plasma Process. Polym. 2 (2005) 525–546. doi:10.1002/ppap.200500036.

[36]   J. Krüger, W. Kautek, Ultrashort pulse laser interaction with dielectrics and polymers, Adv. Polym. Sci. 168 (2004) 247–289. doi:10.1007/b12683.

[37]   H. woon Choi, J.K. Johnson, J. Nam, D.F. Farson, J. Lannutti, Structuring electrospun polycaprolactone nanofiber tissue scaffolds by femtosecond laser ablation, J. Laser Appl. 19 (2007) 225–231. doi:10.2351/1.2795749.

[38]   S. Küper, M. Stuke, Femtosecond uv excimer laser ablation, Appl. Phys. B Photophysics Laser Chem. 44 (1987) 199–204. doi:10.1007/BF00692122.

[39]   S. Küper, M. Stuke, Ablation of polytetrafluoroethylene (Teflon) with femtosecond UV excimer laser pulses, Appl. Phys. Lett. 54 (1989) 4–6. doi:10.1063/1.100831.

[40]   M. Womack, M. Vendan, P. Molian, Femtosecond pulsed laser ablation and deposition of thin films of polytetrafluoroethylene, Appl. Surf. Sci. 221 (2004) 99–109. doi:10.1016/S0169-4332(03)00835-3.

[41]   S. Baudach, J. Bonse, J. Krüger, W. Kautek, Ultrashort pulse laser ablation of polycarbonate and polymethylmethacrylate, Appl. Surf. Sci. 154 (2000) 555–560. doi:10.1016/S0169-4332(99)00474-2.

[42]   E. Stratakis, A. Ranella, C. Fotakis, Biomimetic micro/nanostructured functional surfaces for microfluidic and tissue engineering applications, Biomicrofluidics. 5 (2011) 013411. doi:10.1063/1.3553235.

[43]   E. Stratakis, A. Ranella, M. Farsari, C. Fotakis, Laser-based micro/nanoengineering for biological applications, Prog. Quantum Electron. 33 (2009) 127–163. doi:10.1016/j.pquantelec.2009.06.001.

[44]   E.L. Papadopoulou, A. Samara, M. Barberoglou, A. Manousaki, S.N. Pagakis, E. Anastasiadou, C. Fotakis, E. Stratakis, Silicon Scaffolds Promoting Three-Dimensional Neuronal Web of Cytoplasmic Processes, Tissue Eng. Part C Methods. 16 (2010) 497–502. doi:10.1089/ten.tec.2009.0216.

[45]   H. Webb, J. Arnott, R. Crawford, E. Ivanova, Plastic Degradation and Its Environmental Implications with Special Reference to Poly(ethylene terephthalate), Polymers (Basel). 5 (2012) 1–18. doi:10.3390/polym5010001.

[46]   F. Awaja, D. Pavel, Recycling of PET, Eur. Polym. J. 41 (2005) 1453–1477. doi:10.1016/j.eurpolymj.2005.02.005.

[47]   D. Kint, S. Muñoz- Guerra, A review on the potential biodegradability of poly(ethylene terephthalate), Polym. Int. 48 (1999) 346–352. doi:10.1002/(SICI)1097-0126(199905)48:5<346::AID-PI156>3.0.CO;2-N.

[48]   T. Amari, Y. Ozaki, Real-time monitoring of the initial oligomerization of bis(hydroxyethyl terephthalate) by attenuated total reflection/infrared spectroscopy and chemometrics, Macromolecules. 34 (2001) 7459–7462. doi:10.1021/ma002102f.

[49]   V. Sinha, M.R. Patel, J. V. Patel, Pet waste management by chemical recycling: A review, J. Polym. Environ. 18 (2010) 8–25. doi:10.1007/s10924-008-0106-7.

[50]   H. Nakajima, P. Dijkstra, K. Loos, The Recent Developments in Biobased Polymers toward General and Engineering Applications: Polymers that are Upgraded from Biodegradable Polymers, Analogous to Petroleum-Derived Polymers, and Newly Developed, Polymers (Basel). 9 (2017) 523. doi:10.3390/polym9100523.

[51]   C. Chollet, C. Chanseau, M. Remy, A. Guignandon, R. Bareille, C. Labrugère, L. Bordenave, M.-C. Durrieu, The effect of RGD density on osteoblast and endothelial cell behavior on RGD-grafted polyethylene terephthalate surfaces, Biomaterials. 30 (2009) 711–720. doi:10.1016/j.biomaterials.2008.10.033.

[52]   Y. Li, T. Ma, S.-T. Yang, D.A. Kniss, Thermal compression and characterization of three-dimensional nonwoven PET matrices as tissue engineering scaffolds, Biomaterials. 22 (2001) 609–618. doi:10.1016/S0142-9612(00)00224-6.

[53]   S. Swar, V. Zajícová, M. Rysová, I. Lovětinská-Šlamborová, L. Voleský, I. Stibor, Biocompatible surface modification of poly(ethylene terephthalate) focused on pathogenic bacteria: Promising prospects in biomedical applications, J. Appl. Polym. Sci. 134 (2017). doi:10.1002/app.44990.

[54]   Flow in Tubes | Boundless Physics, (n.d.). https://courses.lumenlearning.com/boundless-physics/chapter/flow-in-tubes/ (accessed April 13, 2020).

[55]   M.M. Janaszak, R.P. Wolfe, T. Ahsan, Biomechanics in Stem Cell Manufacturing, in: Stem Cell Manuf., Elsevier Inc., 2016: pp. 27–42. doi:10.1016/B978-0-444-63265-4.00002-9.

[56]   T.D. Brown, Techniques for mechanical stimulation of cells in vitro: a review, J. Biomech. 33 (2000) 3–14. doi:10.1016/S0021-9290(99)00177-3.

[57]   I.A. Kim, S.A. Park, Y.J. Kim, S.-H. Kim, H.J. Shin, Y.J. Lee, S.G. Kang, J.-W. Shin, Effects of mechanical stimuli and microfiber-based substrate on neurite outgrowth and guidance, J. Biosci. Bioeng. 101 (2006) 120–126. doi:10.1263/JBB.101.120.

[58]   J. Shemesh, I. Jalilian, A. Shi, G. Heng Yeoh, M.L. Knothe Tate, M. Ebrahimi Warkiani, Flow-induced stress on adherent cells in microfluidic devices, Lab Chip. 15 (2015) 4114–4127. doi:10.1039/C5LC00633C.

[59]   J.A. Frangos, L. V. McIntire, S.G. Eskin, Shear stress induced stimulation of mammalian cell metabolism, Biotechnol. Bioeng. 32 (1988) 1053–1060. doi:10.1002/bit.260320812.

[60]   A.M. Sorkin, K.C. Dee, M.L. Knothe Tate, "Culture shock" from the bone cell's perspective: emulating physiological conditions for mechanobiological investigations, Am. J. Physiol. Physiol. 287 (2004) C1527–C1536. doi:10.1152/ajpcell.00059.2004.

[61]   E. Babaliari, G. Petekidis, M. Chatzinikolaidou, A Precisely Flow-Controlled Microfluidic System for Enhanced Pre-Osteoblastic Cell Response for Bone Tissue Engineering, Bioeng. 2018, Vol. 5, Page 66. 5 (2018) 66. doi:10.3390/BIOENGINEERING5030066.

[62]   M. Sato, K. Nagayama, N. Kataoka, M. Sasaki, K. Hane, Local mechanical properties measured by atomic force microscopy for cultured bovine endothelial cells exposed to shear stress, J. Biomech. 33 (2000) 127–135. doi:10.1016/S0021-9290(99)00178-5.

[63]   A.A. Lee, D.A. Graham, S. Dela Cruz, A. Ratcliffe, W.J. Karlon, Fluid Shear Stress-Induced Alignment of Cultured Vascular Smooth Muscle Cells, J. Biomech. Eng. 124 (2002) 37. doi:10.1115/1.1427697.

[64]   K. Hattori, Y. Munehira, H. Kobayashi, T. Satoh, S. Sugiura, T. Kanamori, Microfluidic perfusion culture chip providing different strengths of shear stress for analysis of vascular endothelial function, J. Biosci. Bioeng. 118 (2014) 327–332. doi:10.1016/J.JBIOSC.2014.02.006.

[65]   A. Manbachi, S. Shrivastava, M. Cioffi, B.G. Chung, M. Moretti, U. Demirci, M. Yliperttula,

A. Khademhosseini, Microcirculation within grooved substrates regulates cell positioning and cell docking inside microfluidic channels, Lab Chip. 8 (2008) 747–754. doi:10.1039/b718212k.

[66]   P. Uttayarat, M. Chen, M. Li, F.D. Allen, R.J. Composto, P.I. Lelkes, Microtopography and flow modulate the direction of endothelial cell migration, Am. J. Physiol. - Hear. Circ. Physiol. 294 (2008) H1027–H1035. doi:10.1152/ajpheart.00816.2007.

[67]   M. Khabiry, B.G. Chung, M.J. Hancock, H.C. Soundararajan, Y. Du, D. Cropek, W.G. Lee, A.U. Khademhosseini, Cell docking in double grooves in a microfluidic channel, Small. 5 (2009) 1186–1194. doi:10.1002/smll.200801644.

[68]   J.A. Pedersen, S. Lichter, M.A. Swartz, Cells in 3D matrices under interstitial flow: Effects of extracellular matrix alignment on cell shear stress and drag forces, J. Biomech. 43 (2010) 900–905. doi:10.1016/j.jbiomech.2009.11.007.

[69]   D. Chafik, D. Bear, P. Bui, A. Patel, N.F. Jones, B.T. Kim, C.T. Hung, R. Gupta, Optimization of Schwann Cell Adhesion in Response to Shear Stress in an *in Vitro* Model for Peripheral Nerve Tissue Engineering, Tissue Eng. 9 (2003) 233–241. doi:10.1089/107632703764664701.

[70]   D. Choquet, D.P. Felsenfeld, M.P. Sheetz, Extracellular Matrix Rigidity Causes Strengthening of Integrin–Cytoskeleton Linkages, Cell. 88 (1997) 39–48. doi:10.1016/S0092-8674(00)81856-5.

[71]   C.H. Lee, H.J. Shin, I.H. Cho, Y.M. Kang, I.A. Kim, K.D. Park, J.W. Shin, Nanofiber alignment and direction of mechanical strain affect the ECM production of human ACL fibroblast, Biomaterials. 26 (2005) 1261–1270. doi:10.1016/j.biomaterials.2004.04.037.

[72]   M.G. Park, H. Jang, S.H. Lee, C. Justin Lee, Flow shear stress enhances the proliferative potential of cultured radial glial cells possibly via an activation of mechanosensitive calcium channel, Exp. Neurobiol. 26 (2017) 71–81. doi:10.5607/en.2017.26.2.71.

[73]   B.G. Chung, L.A. Flanagan, S.W. Rhee, P.H. Schwartz, A.P. Lee, E.S. Monuki, N.L. Jeon, Human neural stem cell growth and differentiation in a gradient-generating microfluidic device, Lab Chip. 5 (2005) 401. doi:10.1039/b417651k.

[74]   Y.C. Cheng, C.W. Tsao, M.Z. Chiang, C.A. Chung, C.C. Chien, W.W. Hu, R.C. Ruaan, C. Li, Microfluidic platform for human placenta-derived multipotent stem cells culture and applied for enhanced neuronal differentiation, Microfluid. Nanofluidics. 18 (2015) 587–598. doi:10.1007/s10404-014-1455-2.

[75]   R. Gupta, O. Steward, Chronic nerve compression induces concurrent apoptosis and proliferation of Schwann cells, J. Comp. Neurol. 461 (2003) 174–186. doi:10.1002/cne.10692.

[76]   R. Gupta, L. Truong, D. Bear, D. Chafik, E. Modafferi, C.T. Hung, Shear stress alters the expression of myelin-associated glycoprotein (MAG) and myelin basic protein (MBP) in Schwann cells, J. Orthop. Res. 23 (2005) 1232–1239. doi:10.1016/j.orthres.2004.12.010.

[77]   M.L. Coluccio, G. Perozziello, N. Malara, E. Parrotta, P. Zhang, F. Gentile, T. Limongi, P.M. Raj, G. Cuda, P. Candeloro, E. Di Fabrizio, Microfluidic platforms for cell cultures and investigations, Microelectron. Eng. 208 (2019) 14–28. doi:10.1016/j.mee.2019.01.004.

[78]   C. Zhang, D. Van Noort, Cells in microfluidics, Top. Curr. Chem. 304 (2011) 295–321. doi:10.1007/128_2011_147.

[79]   E.E. Hui, S.N. Bhatia, Micromechanical control of cell-cell interactions, Proc. Natl. Acad. Sci. U. S. A. 104 (2007) 5722–5726. doi:10.1073/pnas.0608660104.

[80]   M. Karimi, S. Bahrami, H. Mirshekari, S.M.M. Basri, A.B. Nik, A.R. Aref, M. Akbari, M.R. Hamblin, Microfluidic systems for stem cell-based neural tissue engineering, Lab Chip. 16 (2016) 2551–2571. doi:10.1039/C6LC00489J.

[81]   M. Mehling, Microfluidic cell culture, Curr. Opin. Biotechnol. 25 (2014) 95–102. doi:10.1016/J.COPBIO.2013.10.005.

[82]   B. Harink, S. Le Gac, R. Truckenmüller, C. Van Blitterswijk, P. Habibovic, Regeneration-on-a-chip? the perspectives on use of microfluidics in regenerative medicine, Lab Chip. 13 (2013) 3512–3528. doi:10.1039/c3lc50293g.

[83]   A.D. Van Der Meer, V. V. Orlova, P. Ten Dijke, A. Van Den Berg, C.L. Mummery, Three-dimensional co-cultures of human endothelial cells and embryonic stem cell-derived pericytes inside a microfluidic device, Lab Chip. 13 (2013) 3562–3568. doi:10.1039/c3lc50435b.

[84]   E. Cimetta, D. Sirabella, K. Yeager, K. Davidson, J. Simon, R.T. Moon, G. Vunjak-Novakovic, Microfluidic bioreactor for dynamic regulation of early mesodermal commitment in human pluripotent stem cells, Lab Chip. 13 (2013) 355–364. doi:10.1039/c2lc40836h.

[85]   R.J. Macown, F.S. Veraitch, N. Szita, Robust, microfabricated culture devices with improved control over the soluble microenvironment for the culture of embryonic stem cells, Biotechnol. J. 9 (2014) 805–813. doi:10.1002/biot.201300245.

[86]   P. Occhetta, M. Centola, B. Tonnarelli, A. Redaelli, I. Martin, M. Rasponi, High-throughput microfluidic platform for 3D cultures of mesenchymal stem cells, towards engineering developmental processes, Sci. Rep. 5 (2015) 1–12. doi:10.1038/srep10288.

[87]   K. Yang, S. Han, Y. Shin, E. Ko, J. Kim, K.I. Park, S. Chung, S.W. Cho, A microfluidic array

for quantitative analysis of human neural stem cell self-renewal and differentiation in three-dimensional hypoxic microenvironment, Biomaterials. 34 (2013) 6607–6614. doi:10.1016/j.biomaterials.2013.05.067.

[88] E. Krausz, R. de Hoogt, E. Gustin, F. Cornelissen, T. Grand-Perret, L. Janssen, N. Vloemans, D. Wuyts, S. Frans, A. Axel, P.J. Peeters, B. Hall, M. Cik, Translation of a Tumor Microenvironment Mimicking 3D Tumor Growth Co-culture Assay Platform to High-Content Screening, J. Biomol. Screen. 18 (2013) 54–66. doi:10.1177/1087057112456874.

[89] C. Lovitt, T. Shelper, V. Avery, Advanced Cell Culture Techniques for Cancer Drug Discovery, Biology (Basel). 3 (2014) 345–367. doi:10.3390/biology3020345.

[90] C.G. Hubert, M. Rivera, L.C. Spangler, Q. Wu, S.C. Mack, B.C. Prager, M. Couce, R.E. McLendon, A.E. Sloan, J.N. Rich, A three-dimensional organoid culture system derived from human glioblastomas recapitulates the hypoxic gradients and cancer stem cell heterogeneity of tumors found in vivo, Cancer Res. 76 (2016) 2465–2477. doi:10.1158/0008-5472.CAN-15-2402.

[91] E. Leclerc, B. David, L. Griscom, B. Lepioufle, T. Fujii, P. Layrolle, C. Legallaisa, Study of osteoblastic cells in a microfluidic environment, Biomaterials. 27 (2006) 586–595. doi:10.1016/J.BIOMATERIALS.2005.06.002.

[92] M.E. Gomes, V.I. Sikavitsas, E. Behravesh, R.L. Reis, A.G. Mikos, Effect of flow perfusion on the osteogenic differentiation of bone marrow stromal cells cultured on starch-based three-dimensional scaffolds, J Biomed Mater Res. 67 (2003) 87–95. https://repositorium.sdum.uminho.pt/bitstream/1822/3864/1/0063.pdf (accessed May 17, 2018).

[93] T. Ono, Y. Suzuki, Y. Kato, R. Fujita, T. Araki, T. Yamashita, H. Kato, R. Torii, N. Sato, A single-cell and feeder-free culture system for monkey embryonic stem cells, PLoS One. 9 (2014). doi:10.1371/journal.pone.0088346.

[94] S.-J. Lo, D.-J. Yao, Get to Understand More from Single-Cells: Current Studies of Microfluidic-Based Techniques for Single-Cell Analysis, Int. J. Mol. Sci. 16 (2015) 16763–16777. doi:10.3390/ijms160816763.

[95] B.L. Wang, A. Ghaderi, H. Zhou, J. Agresti, D.A. Weitz, G.R. Fink, G. Stephanopoulos, Microfluidic high-throughput culturing of single cells for selection based on extracellular metabolite production or consumption, Nat. Biotechnol. 32 (2014) 473–478. doi:10.1038/nbt.2857.

[96] G. Perozziello, P. Candeloro, F. Gentile, A. Nicastri, A. Perri, M.L. Coluccio, A. Adamo, F.

Pardeo, R. Catalano, E. Parrotta, H.D. Espinosa, G. Cuda, E. Di Fabrizio, Microfluidics & nanotechnology: Towards fully integrated analytical devices for the detection of cancer biomarkers, RSC Adv. 4 (2014) 55590–55598. doi:10.1039/c4ra10486b.

[97]   G. Simone, N. Malara, V. Trunzo, M. Renne, G. Perozziello, E. Di Fabrizio, A. Manz, Galectin-3 coats the membrane of breast cells and makes a signature of tumours, Mol. Biosyst. 10 (2014) 258–265. doi:10.1039/c3mb70359b.

[98]   G. Simone, N. Malara, V. Trunzo, G. Perozziello, P. Neuzil, M. Francardi, L. Roveda, M. Renne, U. Prati, V. Mollace, A. Manz, E. Di Fabrizio, Protein-Carbohydrate Complex Reveals Circulating Metastatic Cells in a Microfluidic Assay, Small. 9 (2013) 2152–2161. doi:10.1002/smll.201202867.

[99]   A. Weltin, K. Slotwinski, J. Kieninger, I. Moser, G. Jobst, M. Wego, R. Ehret, G.A. Urban, Cell culture monitoring for drug screening and cancer research: A transparent, microfluidic, multi-sensor microsystem, Lab Chip. 14 (2014) 138–146. doi:10.1039/c3lc50759a.

[100]   S. Breslin, L. O'Driscoll, Three-dimensional cell culture: The missing link in drug discovery, Drug Discov. Today. 18 (2013) 240–249. doi:10.1016/j.drudis.2012.10.003.

[101]   C.R. Thoma, M. Zimmermann, I. Agarkova, J.M. Kelm, W. Krek, 3D cell culture systems modeling tumor growth determinants in cancer target discovery, Adv. Drug Deliv. Rev. 69–70 (2014) 29–41. doi:10.1016/j.addr.2014.03.001.

[102]   A. Marsano, C. Conficconi, M. Lemme, P. Occhetta, E. Gaudiello, E. Votta, G. Cerino, A. Redaelli, M. Rasponi, Beating heart on a chip: A novel microfluidic platform to generate functional 3D cardiac microtissues, Lab Chip. 16 (2016) 599–610. doi:10.1039/c5lc01356a.

[103]   M.D. Nguyen, J.P. Tinney, F. Yuan, T.J. Roussel, A. El-Baz, G. Giridharan, B.B. Keller, P. Sethu, Cardiac cell culture model as a left ventricle mimic for cardiac tissue generation, Anal. Chem. 85 (2013) 8773–8779. doi:10.1021/ac401910d.

[104]   K. Rennert, S. Steinborn, M. Gröger, B. Ungerböck, A.M. Jank, J. Ehgartner, S. Nietzsche, J. Dinger, M. Kiehntopf, H. Funke, F.T. Peters, A. Lupp, C. Gärtner, T. Mayr, M. Bauer, O. Huber, A.S. Mosig, A microfluidically perfused three dimensional human liver model, Biomaterials. 71 (2015) 119–131. doi:10.1016/j.biomaterials.2015.08.043.

[105]   C. Gärtner, B. Ungerböck, I. Schulz, T. Jahn, A. Mosig, T. Mayr, H. Becker, Sensor enhanced microfluidic devices for cell based assays and organs on chip, in: B.M. Cullum, E.S. McLamore (Eds.), Smart Biomed. Physiol. Sens. Technol. XII, SPIE, 2015: p. 948704. doi:10.1117/12.2178690.

[106] A. Blin, A. Le Goff, A. Magniez, S. Poirault-Chassac, B. Teste, G. Sicot, K.A. Nguyen, F.S. Hamdi, M. Reyssat, D. Baruch, Microfluidic model of the platelet-generating organ: Beyond bone marrow biomimetics, Sci. Rep. 6 (2016) 1–12. doi:10.1038/srep21700.

[107] M.J. Wilmer, C.P. Ng, H.L. Lanz, P. Vulto, L. Suter-Dick, R. Masereeuw, Kidney-on-a-Chip Technology for Drug-Induced Nephrotoxicity Screening, Trends Biotechnol. 34 (2016) 156–170. doi:10.1016/j.tibtech.2015.11.001.

[108] H.E. Abaci, K. Gledhill, Z. Guo, A.M. Christiano, M.L. Shuler, Pumpless microfluidic platform for drug testing on human skin equivalents, Lab Chip. 15 (2015) 882–888. doi:10.1039/c4lc00999a.

[109] I. Maschmeyer, A.K. Lorenz, K. Schimek, T. Hasenberg, A.P. Ramme, J. Hübner, M. Lindner, C. Drewell, S. Bauer, A. Thomas, N.S. Sambo, F. Sonntag, R. Lauster, U. Marx, A four-organ-chip for interconnected long-term co-culture of human intestine, liver, skin and kidney equivalents, Lab Chip. 15 (2015) 2688–2699. doi:10.1039/c5lc00392j.

[110] A. Perestrelo, A. Águas, A. Rainer, G. Forte, Microfluidic Organ/Body-on-a-Chip Devices at the Convergence of Biology and Microengineering, Sensors. 15 (2015) 31142–31170. doi:10.3390/s151229848.

[111] K. Schimek, A. Markhoff, F. Sonntag, M. Blechert, R. Lauster, U. Marx, G. Lindner, Integrating skin and vasculature in a Multi-Organ-Chip Platform, BMC Proc. 9 (2015) 1–2. doi:10.1186/1753-6561-9-s9-p20.

[112] A. Panoskaltsis-Mortari, Bioreactor Development for Lung Tissue Engineering, Curr. Transplant. Reports. 2 (2015) 90–97. doi:10.1007/s40472-014-0048-z.

[113] M. Radisic, M. Euloth, L. Yang, R. Langer, L.E. Freed, G. Vunjak-Novakovic, High-density seeding of myocyte cells for cardiac tissue engineering, Biotechnol. Bioeng. 82 (2003) 403–414. doi:10.1002/bit.10594.

[114] X. Li, A. V. Valadez, P. Zuo, Z. Nie, Microfluidic 3D cell culture: Potential application for tissue-based bioassays, Bioanalysis. 4 (2012) 1509–1525. doi:10.4155/bio.12.133.

[115] U. Meyer, T. Meyer, J. Handschel, H.P. Wiesmann, Fundamentals of tissue engineering and regenerative medicine, Springer Berlin Heidelberg, 2009. doi:10.1007/978-3-540-77755-7.

[116] C.E. Schmidt, J.B. Leach, Neural Tissue Engineering: Strategies for Repair and Regeneration, Annu. Rev. Biomed. Eng. 5 (2003) 293–347. doi:10.1146/annurev.bioeng.5.011303.120731.

[117] J.M. Frade, M.C. Ovejero-Benito, Neuronal cell cycle: The neuron itself and its circumstances,

Cell Cycle. 14 (2015) 712–720. doi:10.1080/15384101.2015.1004937.

[118] B.M. Ilfeld, J. Preciado, A.M. Trescot, Novel cryoneurolysis device for the treatment of sensory and motor peripheral nerves, Expert Rev. Med. Devices. 13 (2016) 713–725. doi:10.1080/17434440.2016.1204229.

[119] G.J. TODARO, H. GREEN, Quantitative studies of the growth of mouse embryo cells in culture and their development into established lines., J. Cell Biol. 17 (1963) 299–313. doi:10.1083/jcb.17.2.299.

[120] C. Leibiger, N. Kosyakova, H. Mkrtchyan, M. Glei, V. Trifonov, T. Liehr, First Molecular Cytogenetic High Resolution Characterization of the NIH 3T3 Cell Line by Murine Multicolor Banding, J. Histochem. Cytochem. 61 (2013) 306–312. doi:10.1369/0022155413476868.

[121] K. Bhatheja, J. Field, Schwann cells: Origins and role in axonal maintenance and regeneration, Int. J. Biochem. Cell Biol. 38 (2006) 1995–1999. doi:10.1016/j.biocel.2006.05.007.

[122] J.T. Voyvodic, Target size regulates calibre and myelination of sympathetic axons, Nature. 342 (1989) 430–433. doi:10.1038/342430a0.

[123] C. Taveggia, G. Zanazzi, A. Petrylak, H. Yano, J. Rosenbluth, S. Einheber, X. Xu, R.M. Esper, J.A. Loeb, P. Shrager, M. V. Chao, D.L. Falls, L. Role, J.L. Salzer, Neuregulin-1 type III determines the ensheathment fate of axons, Neuron. 47 (2005) 681–694. doi:10.1016/j.neuron.2005.08.017.

[124] D. Riethmacher, E. Sonnenberg-Riethmacher, V. Brinkmann, T. Yamaai, G.R. Lewin, C. Birchmeier, Severe neuropathies in mice with targeted mutations in the ErbB3 receptor, Nature. 389 (1997) 725–730. doi:10.1038/39593.

[125] K.R. Jessen, R. Mirsky, The origin and development of glial cells in peripheral nerves, Nat. Rev. Neurosci. 6 (2005) 671–682. doi:10.1038/nrn1746.

[126] R. Salto, J.D. Vílchez, M.D. Girón, E. Cabrera, N. Campos, M. Manzano, R. Rueda, J.M. López-Pedrosa, β-Hydroxy-β-methylbutyrate (HMB) promotes neurite outgrowth in Neuro2a cells, PLoS One. 10 (2015). doi:10.1371/journal.pone.0135614.

[127] S.J. Park, M.L. Jin, H.K. An, K.S. Kim, M.J. Ko, C.M. Kim, Y.W. Choi, Y.C. Lee, Emodin induces neurite outgrowth through PI3K/Akt/GSK-3β-mediated signaling pathways in Neuro2a cells, Neurosci. Lett. 588 (2015) 101–107. doi:10.1016/j.neulet.2015.01.001.

[128] P.Y. Wu, Y.C. Lin, C.L. Chang, H.T. Lu, C.H. Chin, T.T. Hsu, D. Chu, S.H. Sun, Functional decreases in P2X7 receptors are associated with retinoic acid-induced neuronal differentiation

of Neuro-2a neuroblastoma cells, Cell. Signal. 21 (2009) 881–891. doi:10.1016/j.cellsig.2009.01.036.

[129]   N. Yanaka, Y. Nogusa, Y. Fujioka, Y. Yamashita, N. Kato, Involvement of membrane protein GDE2 in retinoic acid-induced neurite formation in Neuro2A cells, FEBS Lett. 581 (2007) 712–718. doi:10.1016/j.febslet.2007.01.035.

[130]   A. Ma'ayan, S.L. Jenkins, A. Barash, R. Iyengar, Neuro2A differentiation by Gαi/o pathway, Sci. Signal. 2 (2009) cm1–cm1. doi:10.1126/scisignal.254cm1.

[131]   J. Arsenault, S.A.G. Cuijpers, E. Ferrari, D. Niranjan, A. Rust, C. Leese, J.A. O'Brien, T. Binz, B. Davletov, Botulinum protease-cleaved SNARE fragments induce cytotoxicity in neuroblastoma cells, J. Neurochem. 129 (2014) 781–791. doi:10.1111/jnc.12645.

[132]   R.G. Tremblay, M. Sikorska, J.K. Sandhu, P. Lanthier, M. Ribecco-Lutkiewicz, M. Bani-Yaghoub, Differentiation of mouse Neuro 2A cells into dopamine neurons, J. Neurosci. Methods. 186 (2010) 60–67. doi:10.1016/j.jneumeth.2009.11.004.

[133]   M. Zhu, L. Zhou, B. Li, M.K. Dawood, G. Wan, C.Q. Lai, H. Cheng, K.C. Leong, R. Rajagopalan, H.P. Too, W.K. Choi, Creation of nanostructures by interference lithography for modulation of cell behavior, Nanoscale. 3 (2011) 2723–2729. doi:10.1039/c1nr00015b.

[134]   C.H. Lin, M. Hsieh, S.S. Fan, The promotion of neurite formation in Neuro2A cells by mouse Mob2 protein, FEBS Lett. 585 (2011) 523–530. doi:10.1016/j.febslet.2011.01.003.

[135]   D. Hoffman-Kim, J.A. Mitchel, R. V Bellamkonda, Topography, cell response, and nerve regeneration., Annu. Rev. Biomed. Eng. 12 (2010) 203–31. doi:10.1146/annurev-bioeng-070909-105351.

[136]   M.M. Stevens, J.H. George, Exploring and Engineering the Cell Surface Interface, Science (80-.). 310 (2005) 1135–1138. doi:10.1126/science.1106587.

[137]   J. Mitra, S. Jain, A. Sharma, B. Basu, Patterned growth and differentiation of neural cells on polymer derived carbon substrates with micro/nano structures in vitro, Carbon N. Y. 65 (2013) 140–155. doi:10.1016/j.carbon.2013.08.008.

[138]   D.H. Kim, P.P. Provenzano, C.L. Smith, A. Levchenko, Matrix nanotopography as a regulator of cell function, J. Cell Biol. 197 (2012) 351–360. doi:10.1083/jcb.201108062.

[139]   W.N. Chow, D.G. Simpson, J.W. Bigbee, R.J. Colello, Evaluating neuronal and glial growth on electrospun polarized matrices: bridging the gap in percussive spinal cord injuries., Neuron Glia Biol. 3 (2007) 119–26. doi:10.1017/S1740925X07000580.

[140] E. Schnell, K. Klinkhammer, S. Balzer, G. Brook, D. Klee, P. Dalton, J. Mey, Guidance of glial cell migration and axonal growth on electrospun nanofibers of poly-ε-caprolactone and a collagen/poly-ε-caprolactone blend, Biomaterials. 28 (2007) 3012–3025. doi:10.1016/J.BIOMATERIALS.2007.03.009.

[141] S. Gnavi, B. Fornasari, C. Tonda-Turo, R. Laurano, M. Zanetti, G. Ciardelli, S. Geuna, The Effect of Electrospun Gelatin Fibers Alignment on Schwann Cell and Axon Behavior and Organization in the Perspective of Artificial Nerve Design, Int. J. Mol. Sci. 16 (2015) 12925–12942. doi:10.3390/ijms160612925.

[142] J. Radhakrishnan, A.A. Kuppuswamy, S. Sethuraman, A. Subramanian, Topographic cue from electrospun scaffolds regulate myelin-related gene expressions in schwann cells, J. Biomed. Nanotechnol. 11 (2015) 512–521. doi:10.1166/jbn.2015.1921.

[143] Y. tae Kim, V.K. Haftel, S. Kumar, R. V. Bellamkonda, The role of aligned polymer fiber-based constructs in the bridging of long peripheral nerve gaps, Biomaterials. 29 (2008) 3117–3127. doi:10.1016/j.biomaterials.2008.03.042.

[144] J.M. Corey, D.Y. Lin, K.B. Mycek, Q. Chen, S. Samuel, E.L. Feldman, D.C. Martin, Aligned electrospun nanofibers specify the direction of dorsal root ganglia neurite growth, J. Biomed. Mater. Res. Part A. 83A (2007) 636–645. doi:10.1002/jbm.a.31285.

[145] H. Cao, G. Marcy, E.L.K. Goh, F. Wang, J. Wang, S.Y. Chew, The Effects of Nanofiber Topography on Astrocyte Behavior and Gene Silencing Efficiency, Macromol. Biosci. 12 (2012) 666–674. doi:10.1002/mabi.201100436.

[146] V.J. Mukhatyar, M. Salmerón-Sánchez, S. Rudra, S. Mukhopadaya, T.H. Barker, A.J. García, R. V. Bellamkonda, Role of fibronectin in topographical guidance of neurite extension on electrospun fibers, Biomaterials. 32 (2011) 3958–3968. doi:10.1016/j.biomaterials.2011.02.015.

[147] S.Y. Chew, R. Mi, A. Hoke, K.W. Leong, The effect of the alignment of electrospun fibrous scaffolds on Schwann cell maturation, Biomaterials. 29 (2008) 653–661. doi:10.1016/j.biomaterials.2007.10.025.

[148] H. Xia, X. Sun, D. Liu, Y. Zhou, D. Zhong, Oriented growth of rat Schwann cells on aligned electrospun poly(methyl methacrylate) nanofibers, J. Neurol. Sci. 369 (2016) 88–95. doi:10.1016/j.jns.2016.07.061.

[149] F. Johansson, P. Carlberg, N. Danielsen, L. Montelius, M. Kanje, Axonal outgrowth on nano-imprinted patterns, Biomaterials. 27 (2006) 1251–1258. doi:10.1016/J.BIOMATERIALS.2005.07.047.

[150] L. Yao, S. Wang, W. Cui, R. Sherlock, C. O 'connell, G. Damodaran, A. Gorman, A. Windebank, A. Pandit, Effect of functionalized micropatterned PLGA on guided neurite growth, (2008). doi:10.1016/j.actbio.2008.09.002.

[151] M. Cecchini, G. Bumma, M. Serresi, F. Beltram, PC12 differentiation on biopolymer nanostructures, Nanotechnology. 18 (2007). doi:10.1088/0957-4484/18/50/505103.

[152] A. Ferrari, M. Cecchini, A. Dhawan, S. Micera, I. Tonazzini, R. Stabile, D. Pisignano, F. Beltram, Nanotopographic Control of Neuronal Polarity, Nano Lett. 11 (2011) 505–511. doi:10.1021/nl103349s.

[153] N. Gomez, Y. Lu, S. Chen, C.E. Schmidt, Immobilized nerve growth factor and microtopography have distinct effects on polarization versus axon elongation in hippocampal cells in culture, Biomaterials. 28 (2007) 271–284. doi:10.1016/j.biomaterials.2006.07.043.

[154] J.S. Goldner, J.M. Bruder, G. Li, D. Gazzola, D. Hoffman-Kim, Neurite bridging across micropatterned grooves, Biomaterials. 27 (2006) 460–472. doi:10.1016/j.biomaterials.2005.06.035.

[155] S. Hsu, C.-Y. Chen, P.S. Lu, C.-S. Lai, C.-J. Chen, Oriented Schwann cell growth on microgrooved surfaces, Biotechnol. Bioeng. 92 (2005) 579–588. doi:10.1002/bit.20634.

[156] C. Miller, S. Jeftinija, S. Mallapragada, Micropatterned Schwann cell-seeded biodegradable polymer substrates significantly enhance neurite alignment and outgrowth, Tissue Eng. 7 (2001) 705–715. doi:10.1089/107632701753337663.

[157] J.A. Mitchel, D. Hoffman-Kim, Cellular scale anisotropic topography guides Schwann cell motility, PLoS One. 6 (2011). doi:10.1371/journal.pone.0024316.

[158] A. Béduer, L. Vaysse, E. Flahaut, F. Seichepine, I. Loubinoux, C. Vieu, Multi-scale engineering for neuronal cell growth and differentiation, in: Microelectron. Eng., Elsevier, 2011: pp. 1668–1671. doi:10.1016/j.mee.2010.12.049.

[159] G. Li, X. Zhao, L. Zhang, J. Yang, W. Cui, Y. Yang, H. Zhang, Anisotropic ridge/groove microstructure for regulating morphology and biological function of Schwann cells, Appl. Mater. Today. 18 (2020) 100468. doi:10.1016/j.apmt.2019.100468.

[160] D. Zhang, S. Wu, J. Feng, Y. Duan, D. Xing, C. Gao, Micropatterned biodegradable polyesters clicked with CQAASIKVAV promote cell alignment, directional migration, and neurite outgrowth, Acta Biomater. 74 (2018) 143–155. doi:10.1016/j.actbio.2018.05.018.

[161] G. Li, X. Zhao, W. Zhao, L. Zhang, C. Wang, M. Jiang, X. Gu, Y. Yang, Porous chitosan

scaffolds with surface micropatterning and inner porosity and their effects on Schwann cells, Biomaterials. 35 (2014) 8503–8513. doi:10.1016/j.biomaterials.2014.05.093.

[162]   C. Schulte, S. Rodighiero, M.A. Cappelluti, L. Puricelli, E. Maffioli, F. Borghi, A. Negri, E. Sogne, M. Galluzzi, C. Piazzoni, M. Tamplenizza, A. Podestà, G. Tedeschi, C. Lenardi, P. Milani, Conversion of nanoscale topographical information of cluster-assembled zirconia surfaces into mechanotransductive events promotes neuronal differentiation, J. Nanobiotechnology. 14 (2016) 18. doi:10.1186/s12951-016-0171-3.

[163]   E. Maffioli, C. Schulte, S. Nonnis, F. Grassi Scalvini, C. Piazzoni, C. Lenardi, A. Negri, P. Milani, G. Tedeschi, Proteomic Dissection of Nanotopography-Sensitive Mechanotransductive Signaling Hubs that Foster Neuronal Differentiation in PC12 Cells, Front. Cell. Neurosci. 11 (2018) 417. doi:10.3389/fncel.2017.00417.

[164]   C. Schulte, M. Ripamonti, E. Maffioli, M.A. Cappelluti, S. Nonnis, L. Puricelli, J. Lamanna, C. Piazzoni, A. Podestà, C. Lenardi, G. Tedeschi, A. Malgaroli, P. Milani, Scale Invariant Disordered Nanotopography Promotes Hippocampal Neuron Development and Maturation with Involvement of Mechanotransductive Pathways, Front. Cell. Neurosci. 10 (2016) 267. doi:10.3389/fncel.2016.00267.

[165]   M. Terakawa, Terakawa, Mitsuhiro, Femtosecond Laser Processing of Biodegradable Polymers, Appl. Sci. 8 (2018) 1123. doi:10.3390/app8071123.

[166]   E. Fadeeva, A. Deiwick, B. Chichkov, S. Schlie-Wolter, Impact of laser-structured biomaterial interfaces on guided cell responses., Interface Focus. 4 (2014) 20130048. doi:10.1098/rsfs.2013.0048.

[167]   D. Angelaki, P. Kavatzikidou, C. Fotakis, E. Stratakis, A. Ranella, Laser-induced topographies enable the spatial patterning of co-cultured peripheral nervous system cells, Mater. Sci. Eng. C. 115 (2020) 111144. doi:10.1016/j.msec.2020.111144.

[168]   L.J. Millet, M.E. Stewart, J. V. Sweedler, R.G. Nuzzo, M.U. Gillette, Microfluidic devices for culturing primary mammalian neurons at low densities, Lab Chip. 7 (2007) 987. doi:10.1039/b705266a.

[169]   Y. Nakashima, T. Yasuda, Cell differentiation guidance using chemical stimulation controlled by a microfluidic device, Sensors Actuators, A Phys. 139 (2007) 252–258. doi:10.1016/j.sna.2007.05.035.

[170]   J.H. Kim, J. Sim, H.J. Kim, Neural stem cell differentiation using microfluidic device-generated growth factor gradient, Biomol. Ther. 26 (2018) 380–388. doi:10.4062/biomolther.2018.001.

[171]   J.Y. Park, S.-K. Kim, D.-H. Woo, E.-J. Lee, J.-H. Kim, S.-H. Lee, Differentiation of Neural Progenitor Cells in a Microfluidic Chip-Generated Cytokine Gradient, Stem Cells. 27 (2009) 2646–2654. doi:10.1002/stem.202.

[172]   D. Majumdar, Y. Gao, D. Li, D.J. Webb, Co-culture of neurons and glia in a novel microfluidic platform., J. Neurosci. Methods. 196 (2011) 38–44. doi:10.1016/j.jneumeth.2010.12.024.

[173]   M. Shi, D. Majumdar, Y. Gao, B.M. Brewer, C.R. Goodwin, J.A. McLean, D. Li, D.J. Webb, Glia co-culture with neurons in microfluidic platforms promotes the formation and stabilization of synaptic contacts, Lab Chip. 13 (2013) 3008. doi:10.1039/c3lc50249j.

[174]   Z. Hesari, M. Soleimani, F. Atyabi, M. Sharifdini, S. Nadri, M.E. Warkiani, M. Zare, R. Dinarvand, A hybrid microfluidic system for regulation of neural differentiation in induced pluripotent stem cells, J. Biomed. Mater. Res. Part A. 104 (2016) 1534–1543. doi:10.1002/jbm.a.35689.

[175]   K.J. Jeon, S.H. Park, J.W. Shin, Y.G. Kang, J.-S. Hyun, M.J. Oh, S.Y. Kim, J.-W. Shin, Combined effects of flow-induced shear stress and micropatterned surface morphology on neuronal differentiation of human mesenchymal stem cells, J. Biosci. Bioeng. 117 (2014) 242–247. doi:10.1016/J.JBIOSC.2013.08.002.

[176]   E. Skoulas, A. Manousaki, C. Fotakis, E. Stratakis, Biomimetic surface structuring using cylindrical vector femtosecond laser beams, Sci. Rep. 7 (2017) 45114. doi:10.1038/srep45114.

[177]   M. Lotfi, M. Nejib, M. Naceur, Cell Adhesion to Biomaterials: Concept of Biocompatibility, in: Adv. Biomater. Sci. Biomed. Appl., InTech, 2013. doi:10.5772/53542.

[178]   M. Baker, H. Wayland, On-line volume flow rate and velocity profile measurement for blood in microvessels, Microvasc. Res. 7 (1974) 131–143. doi:10.1016/0026-2862(74)90043-0.

[179]   E. Fröhlich, G. Bonstingl, A. Höfler, C. Meindl, G. Leitinger, T.R. Pieber, E. Roblegg, Comparison of two in vitro systems to assess cellular effects of nanoparticles-containing aerosols, Toxicol. Vitr. 27 (2013) 409–417. doi:10.1016/J.TIV.2012.08.008.

[180]   M. Boissaud-Cooke, T.E. Pidgeon, R. Tunstall, The Microcirculation of Peripheral Nerves: The Vasa Nervorum, Nerves Nerve Inj. (2015) 507–523. doi:10.1016/B978-0-12-410390-0.00039-1.

[181]   M. von Köckritz-Blickwede, O. Chow, M. Ghochani, V. Nizet, Visualization and functional evaluation of phagocyte extracellular traps, Academic Press, 2010. doi:10.1016/S0580-9517(10)37007-3.

[182] K. Ladt, A. Ganguly, S. Roy, Axonal actin in action: Imaging actin dynamics in neurons, Methods Cell Biol. 131 (2016) 91–106. doi:10.1016/BS.MCB.2015.07.003.

[183] J. Schindelin, I. Arganda-Carreras, E. Frise, V. Kaynig, M. Longair, T. Pietzsch, S. Preibisch, C. Rueden, S. Saalfeld, B. Schmid, J.-Y. Tinevez, D.J. White, V. Hartenstein, K. Eliceiri, P. Tomancak, A. Cardona, Fiji: an open-source platform for biological-image analysis., Nat. Methods. 9 (2012) 676–82. doi:10.1038/nmeth.2019.

[184] I. Donelli, P. Taddei, P.F. Smet, D. Poelman, V.A. Nierstrasz, G. Freddi, Enzymatic surface modification and functionalization of PET: A water contact angle, FTIR, and fluorescence spectroscopy study, Biotechnol. Bioeng. 103 (2009) 845–856. doi:10.1002/bit.22316.

[185] E. Rebollar, J.R. Vázquez De Aldana, I. Martín-Fabiani, M. Hernández, D.R. Rueda, T.A. Ezquerra, C. Domingo, P. Moreno, M. Castillejo, Assessment of femtosecond laser induced periodic surface structures on polymer films, Phys. Chem. Chem. Phys. 15 (2013) 11287–11298. doi:10.1039/c3cp51523k.

[186] Z.-L. Chen, W.-M. Yu, S. Strickland, Peripheral Regeneration, Annu. Rev. Neurosci. 30 (2007) 209–233. doi:10.1146/annurev.neuro.30.051606.094337.

[187] E.A. Huebner, S.M. Strittmatter, Axon regeneration in the peripheral and central nervous systems., Results Probl. Cell Differ. 48 (2009) 339–51. doi:10.1007/400_2009_19.

[188] H. Stoll, I.K. Kwon, J.Y. Lim, Material and mechanical factors: New strategy in cellular neurogenesis, Neural Regen. Res. 9 (2014) 1810–1813. doi:10.4103/1673-5374.143426.

[189] K. Franze, The mechanical control of nervous system development, Dev. 140 (2013) 3069–3077. doi:10.1242/dev.079145.

[190] M. Lietz, L. Dreesmann, M. Hoss, S. Oberhoffner, B. Schlosshauer, Neuro tissue engineering of glial nerve guides and the impact of different cell types, Biomaterials. 27 (2006) 1425–1436. doi:10.1016/J.BIOMATERIALS.2005.08.007.

[191] V. Zorba, E. Stratakis, M. Barberoglou, E. Spanakis, P. Tzanetakis, S.H. Anastasiadis, C. Fotakis, Biomimetic Artificial Surfaces Quantitatively Reproduce the Water Repellency of a Lotus Leaf, Adv. Mater. 20 (2008) 4049–4054. doi:10.1002/adma.200800651.

[192] T. Grossetête, A. Rivaton, J.L. Gardette, C.E. Hoyle, M. Ziemer, D.R. Fagerburg, H. Clauberg, Photochemical degradation of poly(ethylene terephthalate)-modified copolymer, Polymer (Guildf). 41 (2000) 3541–3554. doi:10.1016/S0032-3861(99)00580-7.

[193] G.J.M. Fechine, M.S. Rabello, R.M. Souto Maior, L.H. Catalani, Surface characterization of

photodegraded poly(ethylene terephthalate). The effect of ultraviolet absorbers, Polymer (Guildf). 45 (2004) 2303–2308. doi:10.1016/j.polymer.2004.02.003.

[194]   S.G. Prasad, A. De, U. De, Structural and Optical Investigations of Radiation Damage in Transparent PET Polymer Films, Int. J. Spectrosc. 2011 (2011) 1–7. doi:10.1155/2011/810936.

[195]   N.M. Dowell-Mesfin, M.A. Abdul-Karim, A.M.P. Turner, S. Schanz, H.G. Craighead, B. Roysam, J.N. Turner, W. Shain, Topographically modified surfaces affect orientation and growth of hippocampal neurons, J. Neural Eng. 1 (2004) 78–90. doi:10.1088/1741-2560/1/2/003.

[196]   M.A. Bucaro, Y. Vasquez, B.D. Hatton, J. Aizenberg, Fine-tuning the degree of stem cell polarization and alignment on ordered arrays of high-aspect-ratio nanopillars, ACS Nano. 6 (2012) 6222–6230. doi:10.1021/nn301654e.

[197]   J.N. Hanson, M.J. Motala, M.L. Heien, M. Gillette, J. Sweedler, R.G. Nuzzo, Textural guidance cues for controlling process outgrowth of mammalian neurons, Lab Chip. 9 (2009) 122–131. doi:10.1039/b803595d.

[198]   R.L. Leask, L. Rouleau, M. Farcas, J.-C. Tardif, Endothelial Cell Morphologic Response to Asymmetric Stenosis Hemodynamics: Effects of Spatial Wall Shear Stress Gradients, Artic. J. Biomech. Eng. (2010). doi:10.1115/1.4001891.

[199]   A. Brown, G. Burke, B.J. Meenan, Modeling of shear stress experienced by endothelial cells cultured on microstructured polymer substrates in a parallel plate flow chamber, Biotechnol. Bioeng. 108 (2011) 1148–1158. doi:10.1002/bit.23022.

[200]   J.W. Lee, K.S. Lee, N. Cho, B.K. Ju, K.B. Lee, S.H. Lee, Topographical guidance of mouse neuronal cell on SiO2 microtracks, Sensors Actuators, B Chem. 128 (2007) 252–257. doi:10.1016/j.snb.2007.06.017.

[201]   M. Marcus, K. Baranes, M. Park, I.S. Choi, K. Kang, O. Shefi, Interactions of Neurons with Physical Environments, Adv. Healthc. Mater. 6 (2017) 1700267. doi:10.1002/adhm.201700267.

[202]   M. Arnold, E.A. Cavalcanti-Adam, R. Glass, J. Blümmel, W. Eck, M. Kantlehner, H. Kessler, J.P. Spatz, Activation of integrin function by nanopatterned adhesive interfaces, ChemPhysChem. 5 (2004) 383–388. doi:10.1002/cphc.200301014.

[203]   V. Brunetti, G. Maiorano, L. Rizzello, B. Sorce, S. Sabella, R. Cingolani, P.P. Pompa, Neurons sense nanoscale roughness with nanometer sensitivity, Proc. Natl. Acad. Sci. U. S. A. 107 (2010) 6264–6269. doi:10.1073/pnas.0914456107.

[204] A.S.G. Curtis, M. Dolby, N. Gadegaand, Cell signaling arising from nanotopography: Implications for nanomedical devices, Nanomedicine. 1 (2006) 67–72. doi:10.2217/17435889.1.1.67.

[205] E.K.F. Yim, S.W. Pang, K.W. Leong, Synthetic nanostructures inducing differentiation of human mesenchymal stem cells into neuronal lineage, Exp. Cell Res. 313 (2007) 1820–1829. doi:10.1016/j.yexcr.2007.02.031.

[206] F. Pan, M. Zhang, G. Wu, Y. Lai, B. Greber, H.R. Schöler, L. Chi, Topographic effect on human induced pluripotent stem cells differentiation towards neuronal lineage, Biomaterials. 34 (2013) 8131–8139. doi:10.1016/j.biomaterials.2013.07.025.

[207] D.M. Thompson, H.M. Buettner, Oriented Schwann cell monolayers for directed neurite outgrowth, Ann. Biomed. Eng. 32 (2004) 1120–1130. doi:10.1114/b:abme.0000036648.68804.e7.

[208] K.M. Pawelec, C. Yoon, R.J. Giger, J. Sakamoto, Engineering a platform for nerve regeneration with direct application to nerve repair technology, Biomaterials. 216 (2019) 119263. doi:10.1016/j.biomaterials.2019.119263.

[209] U.A. Aregueta-Robles, P.J. Martens, L.A. Poole-Warren, R.A. Green, Tissue engineered hydrogels supporting 3D neural networks, Acta Biomater. 95 (2019) 269–284. doi:10.1016/j.actbio.2018.11.044.

[210] C. Simitzi, Material processing via ultra-short pulsed laser: study of the outgrowth and interfacing of neural networks in 3D Si scaffolds, University of Crete, 2014. https://www.didaktorika.gr/eadd/bitstream/10442/34746/1/34746.pdf (accessed September 1, 2020).